8-6-2020 10:30 AM

Impact Melt-Bearing Deposits Around Martian Craters

William A. Yingling, *The University of Western Ontario*

Supervisor: Neish, Catherine N., *The University of Western Ontario*
Co-Supervisor: Tornabene, Livio L., *The University of Western Ontario*
A thesis submitted in partial fulfillment of the requirements for the Master of Science degree in Geology

Recommended Citation

Yingling, William A., "Impact Melt-Bearing Deposits Around Martian Craters" (2020). *Electronic Thesis and Dissertation Repository*. 7305.
https://ir.lib.uwo.ca/etd/7305

Abstract

In this work, we investigate impact melt emplacement around Martian craters. We compare our results to melt emplacement processes found on Venus, the Moon, and Mercury. We tentatively find Martian melt emplacement more closely resembles Venusian emplacement, rather than lunar emplacement. This suggests Martian melt emplacement likely takes place during the excavation stage where impactor momentum is imparted to the melt. Mercury and Mars have amongst the highest and lowest average impact velocities, respectively, of terrestrial bodies in the Solar System, but a significant difference in emplacement is not observed. This suggests impact velocity may not have as large an influence on melt emplacement as previously thought. It appears lunar melt emplacement is distinct amongst the rocky bodies, where melt is mobilized beyond the crater rim when given additional momentum from central uplift during the modification stage of crater formation.

Keywords

Mars, impact cratering, pitted materials, melt, craters, ejecta, Solar System, melt emplacement, The Moon, Venus, Mercury, HiRISE, CTX, MOLA

Summary for Lay Audience

Impact cratering is a geologic process that continually shapes planetary surfaces. Given the high temperatures and pressures experienced during the impact process, some of the planet's rock will be heated and melted. For this body of work, we investigate how impact melt rock can escape beyond crater rims on Mars. We compare our results to previous results for Venus, the Moon, and Mercury. We investigate how melt is transported and distributed exterior to the interior cavity of the crater. We collect and map high resolution images of the Martian surface in order to determine the distribution of the melt rock. We focus on larger-sized craters, termed "complex craters", so that we may be consistent with previous studies. Venus and the Moon represent two ends of a spectrum for rocky worlds; Venus is a large world with high gravity, while the Moon is a relatively small world with low gravity. In comparison, both Mars and Mercury have an intermediate gravity. We currently see two distinct trends for how melt rock escapes crater rims; on Venus (and to an extent Mercury), the melt rock seems to escape the crater rim in the middle of the cratering process, while on the Moon, melt rock flows over the crater rim later. We seek to determine at what stage of the cratering process melt rock escapes the crater rim during impact events on Mars. We tentatively find that the Martian processes resemble Venusian processes (and also Mercurian processes to an extent). This suggests three new ideas: 1) Martian melt rock escapes the crater rim in the middle of the cratering process, 2) surface gravity plays the most important role in how melt rock escapes the crater rim, and 3) Venus, Mercury and now Mars have similar melt emplacement processes, while the Moon may represent an unusual case for how melt rock is emplaced beyond the crater rim.

Acknowledgments

In this section I would like to acknowledge those who helped make this thesis possible. I would like to acknowledge and thank Dr. Catherine Neish and Dr. Livio Tornabene for being advisors on this thesis. Their continued support, advice, and guidance has been key in making this thesis possible. I am grateful to have been a part of the Western Space program.

Also, I would like to thank my family, particularly my mother and father, for their years of love, inspiration, and encouragement to help put me through school, all the way through this Master's thesis. This would not have been possible without them.

Thank you to Shannon Hibbard, Leah Sacks, and Jahnavi Shah for their years of friendship and collaboration. Without them, my experience at Western would not have been what it was. Whether it was taking on an unexpected roommate or having socially distant picnics, they have been a support system that I cannot thank them enough for.

I would also like to thank the HiRISE Science and Operation team for their contributions. A number of HiRISE images were acquired for this thesis with their assistance, thank you to the CIPPs and HiTS who I worked with and who worked behind the scenes to obtain these images.

Table of Contents

List of Tables

List of Figures

Chapter 1

1 Introduction

Impact cratering is a geologic process that continually shapes planetary surfaces. Distinct associated features of impact cratering include depressions where impactors hit, ejected material, and impact-generated melt rock. The frequency, density, and preservation state of craters can give insight into the geologic history of the surface and near subsurface of a planetary body (Melosh, 1989).

One of these associated features, melt deposits, are emplaced during the cratering process. They are often found on crater floors but can be found exterior to the crater as well. The amount of melt generated during an impact event is dependent on a variety of factors, in particular surface gravity and impactor velocity (Hawke & Head, 1977). Melt generation is a product of an impact event and can be heated to extremely high temperatures. At these high temperatures, melt is capable of mobilizing.

There are a few ways melt can be transported: 1) through ground-hugging flows, 2) by being ejected above the surface, or 3) a combination of both. Ground-hugging melt flows are mobilized under gravity, where the melt transports from a higher potential energy surface to a lower potential energy surface while remaining bound to the surface. Melt and other particles can be lofted above the surface and eventually brought back down by the planetary body’s gravity. If the melt lands on a sloped surface and/or it retains momentum from being lofted, it may then mobilize as a ground-hugging flow, if it does not quench before then. This combination of effects may result in melt that has the appearance of a regular ground hugging flow, but there will be a discontinuity, or lack, of melt between where the melt begins and the crater wall.

In this work, melt that collects exterior to the crater or on terraces at local topographic lows is referred to as a “melt pond”. Other forms of melt include veneers and flows. Veneers are thin coatings of melt and are often remnants of where melt has passed over the surface. A flow is usually a large amount melt that has remained coherent and can be described as lobate.

In this work, we focus on exterior melt ponds about Martian craters. We seek to determine the dominant emplacement mechanism for Martian melt deposits. The distribution of external melt ponds will be evaluated using a statistical analysis to determine if there is a correlation with the rim crest low of the crater. This emplacement mechanism will then be compared to emplacement mechanisms for other previously studied terrestrial bodies, such as the Moon, Venus and Mercury, to gain a broader understanding of melt emplacement around terrestrial planets in general. Mars, shown in Figure 1, is an ideal candidate for study for a number of reasons, specifically: 1) Mars has a modest surface gravity similar to Mercury, but higher than the Moon and less than Venus, and 2) Mars has lower impact velocities than Mercury. Thus, studying melt emplacement mechanisms on Mars will help differentiate the relative influence of surface gravity and impactor velocity in the generation and emplacement of melt.

With its modest surface gravity and low impactor velocities, Mars may resemble lunar, rather than Venusian, emplacement. By studying such constraints for Mars, we will be able to understand the impact cratering process in more detail. This will help to inform models of how impact melt may mobilize on other planetary bodies, including the Earth, Ceres, or even Titan.

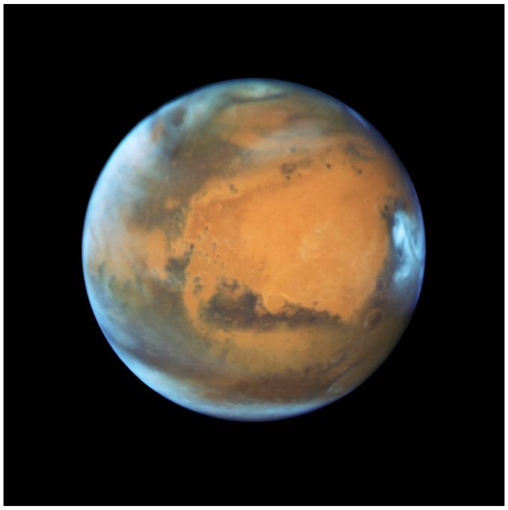

Figure 1. Hubble Space Telescope image of Mars, acquired on May 12, 2016. Credit: NASA, ESA, the Hubble Heritage Team (STScI/AURA), J. Bell (ASU), and M. Wolff (Space Science Institute).

1.1 The Impact Cratering Process

Impacts are features seen all throughout the Solar System. When hypervelocity impact events occur on solid planetary bodies an impact crater is formed. These craters can provide information about the composition and structure of the underlying rock, in such forms as a central uplift and ejecta deposits (Osinski & Pierazzo, 2013).

For bodies with an atmosphere, however, the cratering history can be obscured through erosion and degradation. Therefore, it is important to take this into account when assessing the geologic history of a planet. On the other hand, planetary bodies without a heavily cratered surface can also give insight into its recent geologic history. For example, Pluto’s Sputnik Planitia has a distinct lack of craters larger than 2 km, suggesting that the region has undergone recent resurfacing, which is estimated to be less than 10 million years old (Trilling, 2016).

Both target and impactor properties play important roles when it comes to impact cratering. The material composition of the target, target surface gravity, presence of an atmosphere, impactor speed and size, and angle of entry can all influence the morphology of the resulting crater (Melosh, 1989). Osinski & Pierazzo (2013) emphasize that different planetary environmental conditions, such as surface gravity, can also lead to differences in the cratering process. For example, effects of other environmental conditions, such as strength, structure, and composition of the country rock, can be seen in the variation of diameters for transitional craters on different planetary bodies, and even within the same planetary body (Boyce et al., 2006; Melosh, 1989; Pike, 1977b, 1977a, 1980; Silber et al., 2017).

One of the variables that can be constrained for Mars is the impactor type. Ivanov et al. (1999) suggest that the size frequency distribution of lunar craters show asteroids from the main belt are the main source of impactors for terrestrial planets. In other words, the population of terrestrial-body impactors is predominantly made up of main-belt asteroids, with an insignificant number of impactors coming from comets or Kuiper-belt objects. Therefore, we can generally assume that impactors that strike the surface of Mars resemble the composition of the main asteroid belt (Neukum, Ivanov, & Hartmann, 2001; Ivanov, 2001). The complete composition of the asteroid belt can subdivided into many different spectral classes, but the classes which make up the most mass are C-, B-, P-, V-, and S-type asteroids (DeMeo and Carry, 2013). In particular, the C- and P-type asteroids make up more than half the mass of the asteroid belt, when large asteroid bodies including Ceres, Pallas, Vesta, and Hygiea are excluded from the mass calculation (DeMeo and Carry, 2013). C-type asteroids are the most common type of asteroid and resemble carbonaceous chondrites.

Other variables, like surface gravity and impactor velocity, can also be constrained, making comparisons between terrestrial bodies possible. Stöffler et al. (2006) describe the Moon as an end member among the Solar System’s terrestrial bodies. It has low surface gravity, a distinct lack of an atmosphere, moderate impact velocities, and a lack of aeolian/aqueous resurfacing processes. In this regard, Mercury can be similarly grouped with the Moon, albeit with higher impact velocities and surface gravity (Schultz, 1988; Strom et al., 2011). The other end of the terrestrial body spectrum can be represented by Venus. Venus has a hot, thick atmosphere, a comparatively high surface gravity, moderately high impact velocities, and a low cratering efficiency (Schultz, 1993). Therefore, Mars, with its tenuous atmosphere, dynamic geological processes, surface gravity comparable to Mercury and low impactor velocities, is an ideal case study. It represents a terrestrial planet in between the two end members of the Moon and Venus (Carr, 2006). It therefore gives us insight into the physics involved in the impact cratering process.

There are four stages, shown in Figure 2, in the impact cratering process: 1) contact and compression, 2) excavation, 3) modification, and 4) hydrothermal/chemical alteration (Gault et al., 1968; Kieffer and Simonds, 1980). The fourth stage, hydrothermal/chemical alteration, is not often emphasized due to the required presence of volatiles.

1.1.1 Contact and Compression

The first stage, contact and compression, is the shortest of the three main stages. It begins with the contact of a hypervelocity impactor striking the surface of a target body. Consequently, energy is imparted from the impactor to the target and vice versa in the form of momentum, heat, and shock waves (Ahrens & O'Keefe, 1972; Melosh, 1989). The shock waves imparted into the impactor cause it to melt and often vaporize (Gault et al., 1968; Melosh, 1989). When the shock wave reaches the top of the impactor/surface, a rarefaction wave begins propagating outward, releasing the stress imposed by the initial shock wave. This is considered the conclusion of the contact and compression stage (Melosh, 1989).

1.1.2 Excavation

The second stage, excavation, is affected by a number of variables including surface gravity, target material properties, and the expanding shock wave (Melosh, 1989). The shock wave expands roughly spherically, attenuating the further away it gets, until it eventually turns into a lower-energy elastic wave which no longer shocks the target rock (Melosh, 1989). While the shock wave propagates radially outward faster than the speed of sound, crater excavation will take place at a much slower rate, where the excavation time is most dependent on the body's surface gravity (Melosh, 1989). The shock wave can shock, heat, and mobilize the target rock (Melosh, 1989). Crater excavation takes place through the combination of the shock wave and a closely followed rarefaction wave. An excavation flow field begins to form, creating what is called a “transient cavity” (Dence, 1968; Grieve and Cintala, 1981; Osinski and Pierazzo, 2012). Two zones are generally formed in the transient cavity: an upper excavated zone and a lower displaced zone. The target rock in the upper excavation zone is transported outside of the transient cavity rim, forming the ejecta blanket (Oberbeck, 1975). The lower displacement zone represents rock that either stays within the crater or melt-rich rock that has been mobilized out of the transient cavity via ejection or surface flow (Osinski et al., 2011; Osinski and Pierazzo, 2012). During the excavation stage, vapor plumes may be generated, and material can even be ejected at velocities greater than the planetary body’s escape velocity.

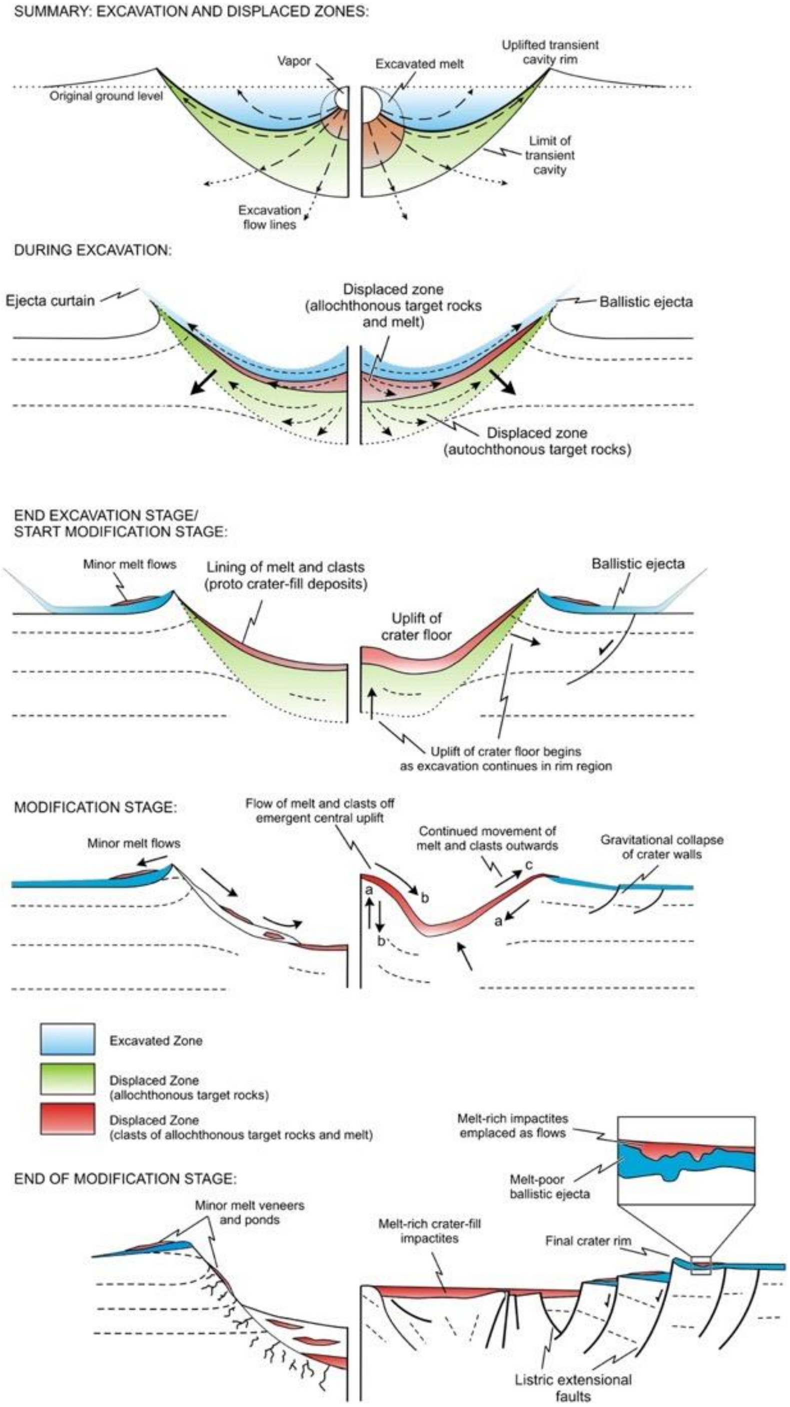

Figure 2. Diagram of the impact cratering process for simple (left) and complex (right) craters. Top diagram shows the end of the contact and compression stage. Middle two diagrams show the excavation stage. Second from the bottom diagram shows the modification stage. Bottom diagram shows the end of the modification stage. From Osinski et al., 2011.

1.1.3 Modification

Although there is overlap between when the excavation stage ends and when the modification stage begins, the modification stage generally begins when the transient cavity starts collapsing. The size of the crater and local surface gravity will control the degree of collapse (Melosh & Ivanov, 1999). If the transient cavity has minimal collapse, the remaining bowl-shaped depression is often referred to as a simple crater. If a sufficiently large transient cavity undergoes extensive modification, producing terracing, wall slumping, and stratigraphic uplift, then it is referred to as a complex crater (Dence, 1965; Melosh, 1989). Gravitational forces dominate the modification of larger craters, while the strength of the target material influences the morphology of smaller craters. A secondary ejecta emplacement process takes place during this stage, too, where melted rock may mobilize and flow along the ground. The melt generally will pond at topographic lows, including on the crater floor and within the ejecta blanket. There is no definite end to the modification stage (French, 1998).

1.1.4 Hydrothermal/Chemical Alteration

The post-impact hydrothermal alteration stage is often not emphasized because it requires the existence of volatiles, and, while common on Earth, they are not found everywhere in the Solar System. Subsurface volatiles, however, are present on Mars and their effects are seen in the form of pitted materials. The effects of volatile interaction with the impact cratering process is not entirely understood at present and remain open for discussion (Boyce et al., 2012; Denevi et al., 2012; Osinski et al., 2011; Tornabene et al., 2012). However, the formation of pitted materials on Mars likely happens during the alteration stage. Fractures known to have been formed during the modification stage can crosscut the pits within the pitted material, therefore suggesting that the fractures and the pits form at generally the same time.

1.1.5 Crater Morphologies

As mentioned above, impact craters can generally be subdivided into two groups: simple and complex. Simple craters are bowl-shaped depressions with raised rims. Inside the simple crater may also be an allochthonous breccia lens which contains shocked and unshocked target material (Shoemaker, 1960). They are represented by a depth-to-diameter ratio of 1:5 to 1:7 (Melosh, 1989). (Note: the most well-preserved craters will have deeper depths than less-preserved craters due to the nature of crater infilling and degradation over time.) In terms of depth-to-diameter ratios, the deepest craters will have ratios approaching 1:5 (Pike, 1977b), while the shallowest craters will tend towards 1:∞ (for extremely eroded craters; see Neish et al., 2016.). In contrast, complex craters, which are shown for different worlds in Figure 3, are characterized by their terraced walls, a generally flat crater floor, stratigraphic uplift often in the form of a central peak, scalloped rims, and depth-to-diameter ratios of 1:10 to 1:20 (Melosh, 1989; Osinski & Pierazzo, 2013; Pike, 1980). In addition to these two main types, there are also other types such as transitional craters and peak-ring basins. Transitional craters have diameters between simple and complex craters and have some characteristics of complex craters but not all (e.g., flat floors but no central uplift) (Robbins and Hynek, 2012). Peak-ring basin craters are even larger forms of complex craters, with characteristic features such as concentric circular scarps and ejecta blankets (Melosh, 1989). Multi-ring basin craters have not been considered for this study because of their ill-defined rims and ejecta blankets.

1.2 Mars

Mars is a fascinatingly complex world; craters, immense mountains, deep canyons, extensive flood plains, basaltic lava flows, and polar ice caps are just a few examples of its geologic diversity. It has captivated, inspired, and enthused many to explore planetary science and continues to do so to this day. The similarity of Mars to Earth has further piqued our collective interest and we send mission after mission to explore this unique world to compare it to our own. The differences between these two worlds further inspires curiosity and prompts multitudes of questions.

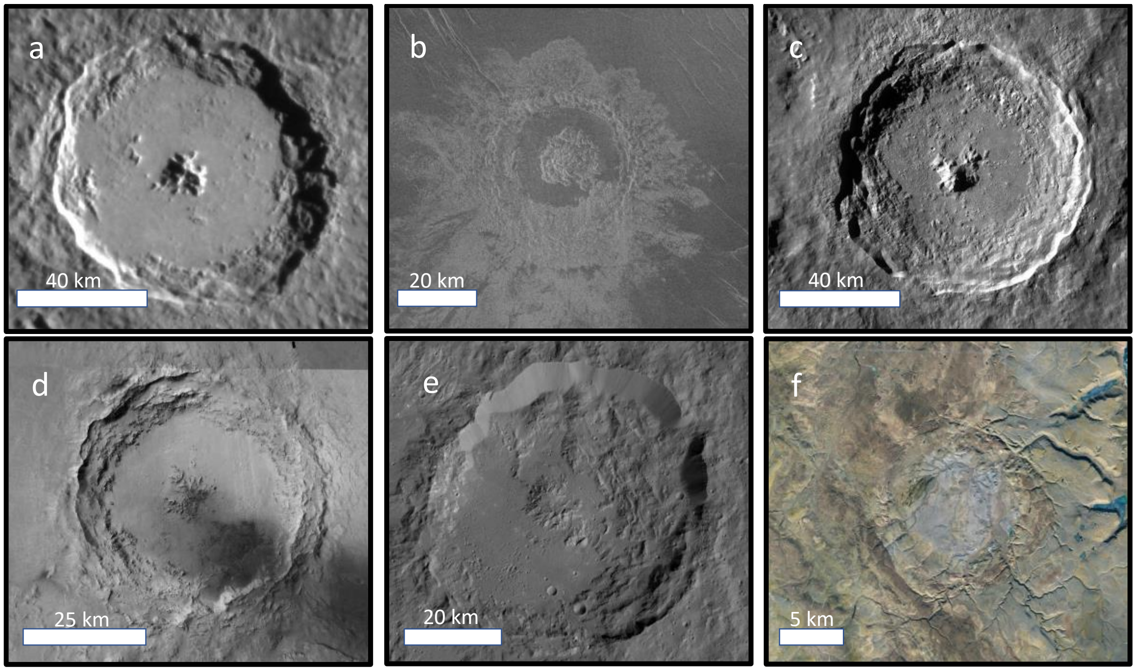

Figure 3. Complex craters on different rocky bodies in the Solar System. Notable morphologic features of complex craters include a central peak, terraced walls, and a flat crater floor. North is up. a) Debussy crater on Mercury, b) Xantippe crater on Venus, c) Tycho crater on the Moon, d) Mojave crater on Mars, e) Ikapati crater on Ceres, f) Haughton crater on Earth. Images were collected using JMARS and Google Earth.

Mars has an atmosphere though it is only a fraction of that compared to Earth's (approximately 700 Pa for Mars, compared to 101,325 Pa for Earth), which is dominated by carbon dioxide (~95%) (Barlow, 2008). Orbital magnetic field measurements show it once harbored a magnetic field, but it is not currently present (Acuña et al., 1999; Lillis et al., 2013).

1.2.1 Orbital Properties

Mars lies about 1.5 AU away from the Sun. A year on Mars takes approximately 688 Earth-days to complete a single orbit. The inclination of the orbit is approximately 1.85° from the plane of the Solar System. However, the orbit of Mars is not completely circular, it has an eccentricity of about 0.093. The eccentricity of Mars is relatively high amongst the planets in the Solar System, second only to Mercury. This means that Mars will be closer to Sun during perihelion and further away from the Sun at aphelion. Solar longitude – the time of year – on Mars is represented by L_S, in units of degrees, where the Martian year begins with $L_S=0^o$ at the vernal equinox and ends the year at $L_S=360^o$. Because of the eccentricity of the Martian orbit, the seasons are different lengths. To illustrate, Barlow (2008) details that northern spring (southern autumn) lasts for about 200 Earth-days while northern autumn (southern spring) lasts for about 146 Earth-days.

The axial tilt of Mars, or obliquity, is approximately 25^o. For comparison, the tilt of Earth is roughly 24^o. This means that Mars experiences similar seasons to Earth, with a spring, summer, autumn and winter. The sidereal rotation period, how long it takes for the Sun to reach to same position in the sky each day, for Mars is $24^h\ 37^m\ 22.65^s$ (Barlow, 2008), somewhat longer than a standard day on Earth.

1.2.2 Geology

1.2.2.1 Dichotomy

Mars has been observed to be dynamic and varied in its geologic processes. The Martian crust can be separated into two morphologically/topographically distinctive halves, also known as the Martian dichotomy: the smoother northern lowland plains and the heavily-cratered southern highlands. The crust is of variable thickness: thicker in the southern hemisphere than in the northern hemisphere (Neumann et al., 2004; Sohl and Spohn, 1997; Zuber, 2000). The crater size frequency distributions are distinct for the young northern plains and the old southern highlands, indicating that the northern plains have likely been resurfaced by volcanic, fluvial, and/or periglacial processes, although when and how resurfacing took place is open for debate (Barlow, 1988; Carr and Head, 2010; Hartmann et al., 2001; Strom et al., 1992).

1.2.2.2 Interior

An accepted model representing the core of Mars remains somewhat elusive; Smith et al., (2001) propose a solid core theory, while Yoder et al. (2003) propose a largely molten iron core with either little or no solids. Mars currently lacks a magnetic field, but it has been shown that it used to have a magnetic dynamo (Acuña et al., 2001, 1999). Lack of a current magnetic dynamo implies there is either not enough convection in the core or there is not sufficient solidification in the core to produce a magnetic field (Schubert et al., 2000; Stevenson, 2001). Recent surface measurements by InSight (Interior Exploration using Seismic Investigations, Geodesy and Heat Transport) have suggested that the Martian dynamo could have potentially lasted 200 My longer than previously thought, shutting off around 3.9 Gy ago, instead of 4.1 Gy ago (Johnson et al., 2020).

1.2.2.3 Geologic Processes

There are many interesting geologic processes that can be studied on Mars. These processes include past fluvial activity, volcanism, glacial and periglacial processes, and aeolian transport. Notable observations include: 1) layered ejecta on Mars (Barlow et al., 2000), suggesting the presence and interaction of subsurface volatiles (Carr et al., 1977; Stevenson, 2001), and/or ejecta blanket interaction with the Martian atmosphere (Barnouin-Jha et al., 1999a, 1999b; Schultz, 1992). 2) Mars is home to the largest shield volcano in the Solar System with a volume of about 3×10^6 km^3 (Smith et al., 2001). 3) Aeolian processes continue to shape the surface of Mars, first noted by McCauley (1973) and Ward (1979). Edgett & Malin (2000) were among the first to observe actively moving dunes on Mars, with the use of MGS. Later studies with HiRISE and CTX data have provided much finer detail, showing the movement of sand ripples, which further confirms that aeolian processes are contemporary and continue to sculpt the surface of Mars (e.g. Bridges et al., 2007; Chojnacki, Burr, Moersch, & Michaels, 2011).

Mars also provides a window into the impact cratering process due to its unique geology and environmental conditions, including having an atmosphere. As discussed above, craters on Mars can be simple, transitional, or complex. The defining characteristics of each classification, however, can vary for each planetary body, depending on the gravity regime and strength of the host material (Boyce and Garbeil, 2007; Pike, 1980). For Mars, simple craters tend to form at <6 km, transitional craters form at 6-9 km and complex craters tend to form at >9 km. Depth to diameter ratios of some of the best-preserved craters on Mars can be found within Tornabene et al. (2018).

1.2.2.4 Geologic Time

Similar to Earth, we divide up geologic periods on Mars. Broadly, from oldest to youngest, these three periods are called: Noachian, Hesperian, and Amazonian. The Noachian period begins before 3.95 Gy ago and extends until about 3.7 Gy ago. Noachian terrain is categorized generally as having the most heavily cratered surfaces, having formed during the Late Heavy Bombardment (Hartmann et al., 2001). The Noachian period is subdivided into late, middle, and early defined by their relative crater densities found by Hartmann et al. (2001). The Hesperian period follows the Noachian, extending from 3.7 Gy ago to about 3.0 Gy ago. It is characterized by heightened volcanic activity and declining impact rates from the Late Heavy Bombardment (Barlow, 2008). The Hesperian period is subdivided into two periods: late and early. The most recent period is the Amazonian. It begins about 3.0 Gy ago and extends to present day. It is characterized by low impact cratering rates, low erosion rates, and localized volcanic activity (Barlow, 2008).

1.2.2.5 Surface Composition

The surface of Mars is largely composed of varying forms of basalt. Utilizing the Thermal Emission Spectrometer aboard the Mars Global Surveyor, Bandfield et al., (2000) identified two distinct low-albedo regions on the Martian surface; the boundary between the two regions lies roughly along the dichotomy. The composition of the older unit in the southern hemisphere is of a basaltic composition dominated by plagioclase feldspar and clinopyroxene, whereas the younger northern plains have an andesitic composition dominated by plagioclase and volcanic glass (Bandfield et al., 2000). In follow up work, Bandfield, (2002) details that bright regions on Mars are often dust-covered, which covers up the underlying bedrock.

1.2.2.6 Volatiles

One aspect that makes Mars unique is the presence of volatiles on the surface. Volatiles, as their name suggests, are compounds that may readily change state, such as from a solid to gaseous form, and so can be fleeting. This includes such molecules as CO_2 and water-ice. Proposed by Leighton & Murray (1966), the polar caps show a dynamic cycle of sublimation and accumulation of volatiles, namely CO_2. Furthermore, volatiles and the atmosphere have been theorized to play a role in ejecta morphology for Mars (Barlow, 2005; Barnouin-Jha et al., 1999b, 1999a; Carr et al., 1977; Schultz, 1992; Stewart et al., 2001), contributing to the layered ejecta that has been observed. During a cratering event, it is more likely that subsurface volatiles are the dominant contributor to the formation and morphology of the final ejecta blanket (Barlow, 2005).

Barlow & Bradley, (1990) showed that subsurface volatiles on Mars play a distinct role in the ejecta morphology of craters, citing that larger craters – craters which excavate through the icy upper layer down to the volatile-poor layer – display distinctly different ejecta morphologies (e.g. smaller multiple-lobe ejecta morphology craters likely excavate only the top icy layer and potentially brines beneath the surface, whereas larger radial ejecta morphology craters excavate material down to the volatile-poor layer).

The utilization of gamma ray spectroscopy has allowed for mapping of the Martian surface and immediate subsurface (~1 m) of water-equivalent hydrogen. Feldman et al., (2004) found large fractions (20-100%) of water equivalent hydrogen lie within the subsurface for regions poleward of ~±50º. They also found that for the more equatorial regions of Mars, a nonnegligible fraction (2-10%) of water equivalent hydrogen exists within the subsurface. Feldman et al., (2004) further explain that reservoirs at high latitudes likely contain high concentrations of water-ice and that for the more equatorial regions with high water equivalent hydrogen signatures likely relate to water-ice or hydrated minerals.

1.2.3 Instrumentation

In this study, data from three orbital instruments have been utilized: The High Resolution Imaging Science Experiment (HiRISE), the Context Camera (CTX), and the Mars Orbiter Laser Altimeter (MOLA). HiRISE and CTX are both aboard the Mars Reconnaissance Orbiter (MRO), which launched in August 2005 and entered Mars orbit in March 2006. MOLA flew aboard the Mars Global Surveyor (MGS) from 1996 to 2007 (Albee et al., 1998). In November 2006, MRO began its primary science phase. Part of MRO's science objective was to map the surface of Mars in high-resolution, utilizing HiRISE and CTX data in order to assess the viability of past, present, and future landing sites (Malin et al., 2007; McEwen et al., 2007). The primary science phase of MRO lasted two years from 2006 to 2008. At the time of writing, MRO continues to collect valuable data with respect to the Martian atmosphere, weather, geology, polar caps, and in the search for potential liquid water.

1.2.3.1 HiRISE

HiRISE, shown in a clean room in Figure 4, is a 0.5 m orbital telescope observing the surface of Mars. This pushbroom-style imaging system takes images at resolutions of 0.25 to 0.5 m/pixel (McEwen et al., 2007). There are fourteen Charged Couple Devices, or CCDs, aboard HiRISE. Two CCDs record near infrared wavelengths, two record blue-green wavelengths, and ten CCDs record red wavelengths. The two infrared and two blue-green CCDs are both aligned to the middle of the ten-long red CCD array. Each CCD produces a strip of the image, which then have to be stitched together to form the full image. For this study, we have utilized the red CCDs in order to obtain the most amount of coverage. HiRISE images are approximately 6 km wide, with variable lengths.

Figure 4. The HiRISE camera being worked on in a clean room. Taken from https://mars.nasa.gov/mro/mission/instruments/hirise/

1.2.3.2 CTX

CTX is also a pushbroom-style camera that takes images in the mostly visible wavelength range (500-800 nm) over a much larger footprint with resolutions of approximately 6 m/pixel (Malin et al., 2007). While HiRISE will only ever be able to cover a fraction of the surface of Mars, CTX provides much larger swaths of coverage (30 km wide) and much needed context, enabling a global mosaic of CTX images to be made of Mars (Dickson et al., 2018).

1.2.3.3 MOLA

The primary goal of MOLA was to characterize the global topography of Mars, via the use of a laser altimeter (Smith et al., 2001; Zuber et al., 1992). MOLA has a vertical resolution of 1.5 m. It functioned as an active remote sensing instrument by sending a laser pulse from the instrument to the surface and wait for the signal to reflect back. The difference in reflected laser pulse timing can then be used to calculate the local elevation of the surface. During the MGS’s mapping orbit, MOLA shot spacing along-track was approximately 300 m in between shots and approximately 4 km in across-track spacing (Smith et al., 2001). The shots are recorded and collected to then create a global mosaic, where the spaces in between shots are interpolated in order to create a 3-dimensional surface. The spatial scale of the global mosaic is a 0.2º x 0.2º grid (Zuber et al., 1992).

1.3 Exterior Melt Deposit Characteristics

Impact melt emplacement is an important part of the impact cratering process. In addition to Earth, evidence for impact melt deposits have been found on all of the Solar System's largest terrestrial bodies, including the Moon, Venus, Ceres, Vesta, Mercury and Mars, as shown in Figure 5 and Figure 6 (e.g., Boyce et al., 2012; Chadwick & Schaber, 1993; Cintala & Grieve, 1998; Daniels, 2018; Denevi et al., 2012; Grieve & Cintala, 1995; Hawke & Head, 1977; Krohn et al., 2016; Leight & Ostrach, 2018; Marvin & Kring, 1992; Osinski & Pierazzo, 2013; Sizemore et al., 2017; Susorney et al., 2016; Tornabene et al., 2012).

1.3.1 Melt on the Moon and Other Volatile-Poor Bodies

Melt identified in and around lunar craters was originally thought to be of volcanic origin (Strom and Fielder, 1970, 1968). However, work by Howard & Wilshire (1975) showed that for a sample of lunar craters, the melt had a distribution similar to other impact-generated material, suggesting that the melt was mobile along with the ejecta during crater formation. In addition, Hawke & Head (1977) defined characteristic criteria for impact-related melt. These criteria included (1) deposit distribution being asymmetrical due to effects of impactor direction and/or the surface topography, (2) a lack of nearby volcanic sources, (3) distinct impact morphology, and (4) melt emplacement that is temporally closely associated with the impact itself. Impact melt differs from volcanic melt because volcanic melt is formed through decompression or hydration melting, whereas impact melt is generated through shock decompression and excess waste heat (Grieve et al., 1977; Osinski et al., 2018). Unlike endogenic metamorphism, the excess work from the adiabatic release of the shock wave will create waste heat, initially superheating the melt (Grieve et al., 1977; Osinski et al., 2011).

1.3.2 Melt on Mars and Other Volatile-Rich Bodies

Identification of impact melt on Mars remained challenging until the Mars Reconnaissance Orbiter (MRO) and the on-board High Resolution Imaging Science Experiment (HiRISE) delivered high-resolution images of the best-preserved craters showing densely pitted deposits initially referred to as a crater-related pitted material (Tornabene et al., 2007b, 2007a), and has since been demonstrated to be consistent with and interpreted to be volatile-rich impact melt-bearing deposits (Tornabene et al., 2007a, 2007b, 2012).

Crater-related pitted materials were first observed at Hale, Mojave, Tooting, Zumba and Zunil crater on Mars (Tornabene et al., 2007b). Follow up work by Tornabene et al. (2012) and Boyce et al., (2012) flushed out how melt-bearing impactite deposits form crater-related pitted materials due to the interaction between the impact event and subsurface volatiles. Later that year, the existence of pitted materials was further validated when Denevi et al., (2012) observed them on Vesta. They are quasi-circular depressions with subtly raised rims and are mostly found on the surfaces of ponded deposits and are contiguous with smooth flowing deposits where slopes are higher (Tornabene et al., 2012). On Mars, the diameter of pitted materials can reach up to three kilometers (Tornabene et al., 2012).The presence of crater-related pitted materials provide additional morphologic evidence for the role of target volatiles during the impact process (Tornabene et al., 2012); this is further supported by the lack of observation of them on volatile-poor bodies, such as the Moon and Mercury, and additional observations of them on other volatile-rich bodies such as Vesta and Ceres (Denevi et al., 2012; Sizemore et al., 2017; Tornabene et al., 2012).

There are two main morphologies for external melt deposits that we focus on here: 1) ponds, and 2) flows (Hawke and Head, 1977). While, melt veneers – what are generally thin coatings of melt – are observed where melt has traveled, such as central uplifts, crater walls and rims, they appear to be not very distinctive on Mars when compared to other bodies (Tornabene et al., 2012). As such, they will not be considered any further in this work. Melt flows often include lobate features, and levees/channels. Melt ponds can often be identified by the presence of cooling cracks, although this is not commonly seen on Mars, and their mostly flat surfaces. This is because when the fluidized melt ponds pool at a topographic low, the surface of the pond will be equipotential, much like the surface of a lake. Melt ponds on Mars, Vesta and Ceres are additionally characterized by the presence of pitted materials (Denevi et al., 2012; Sizemore et al., 2017; Tornabene et al., 2012). The most common distinctive morphologic expression of melt on Mars are melt ponds with pitted materials and we use this as a defining guide for identifying melt.

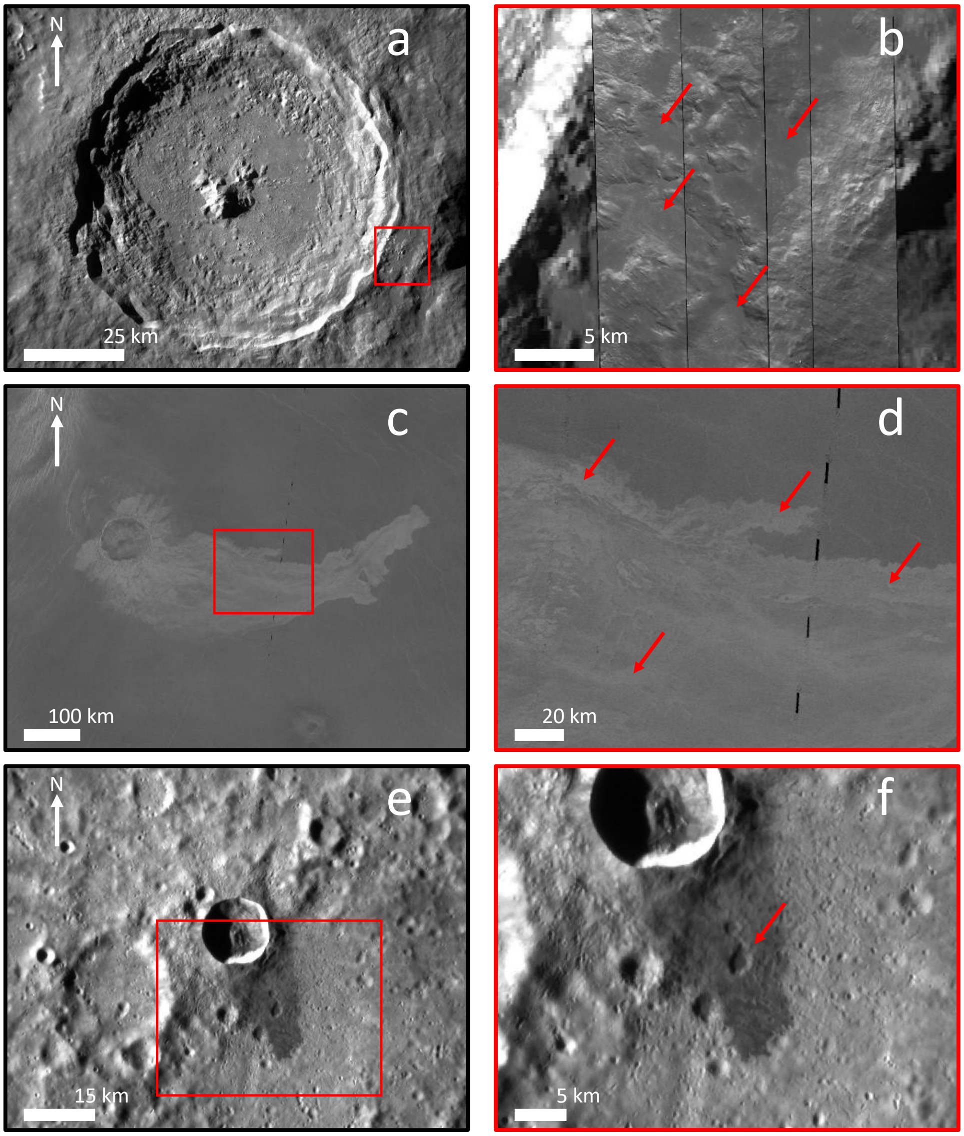

Figure 5. Morphology of impact melt on various planetary bodies. Red boxes show the inset boundary for the images to their right. Red arrows denote melt deposits. a) Tycho crater on the Moon (-43.30°, 348.79°), b) inset of Tycho crater with melt ponds exterior to crater, c) Addams crater on Venus (-56.20°, 98.90°), d) inset of Addams crater with a large melt flow, e) Waters crater on Mercury (-8.94°, 254.65°), f) inset of Waters crater with melt exterior to the crater. Images were made using JMARS.

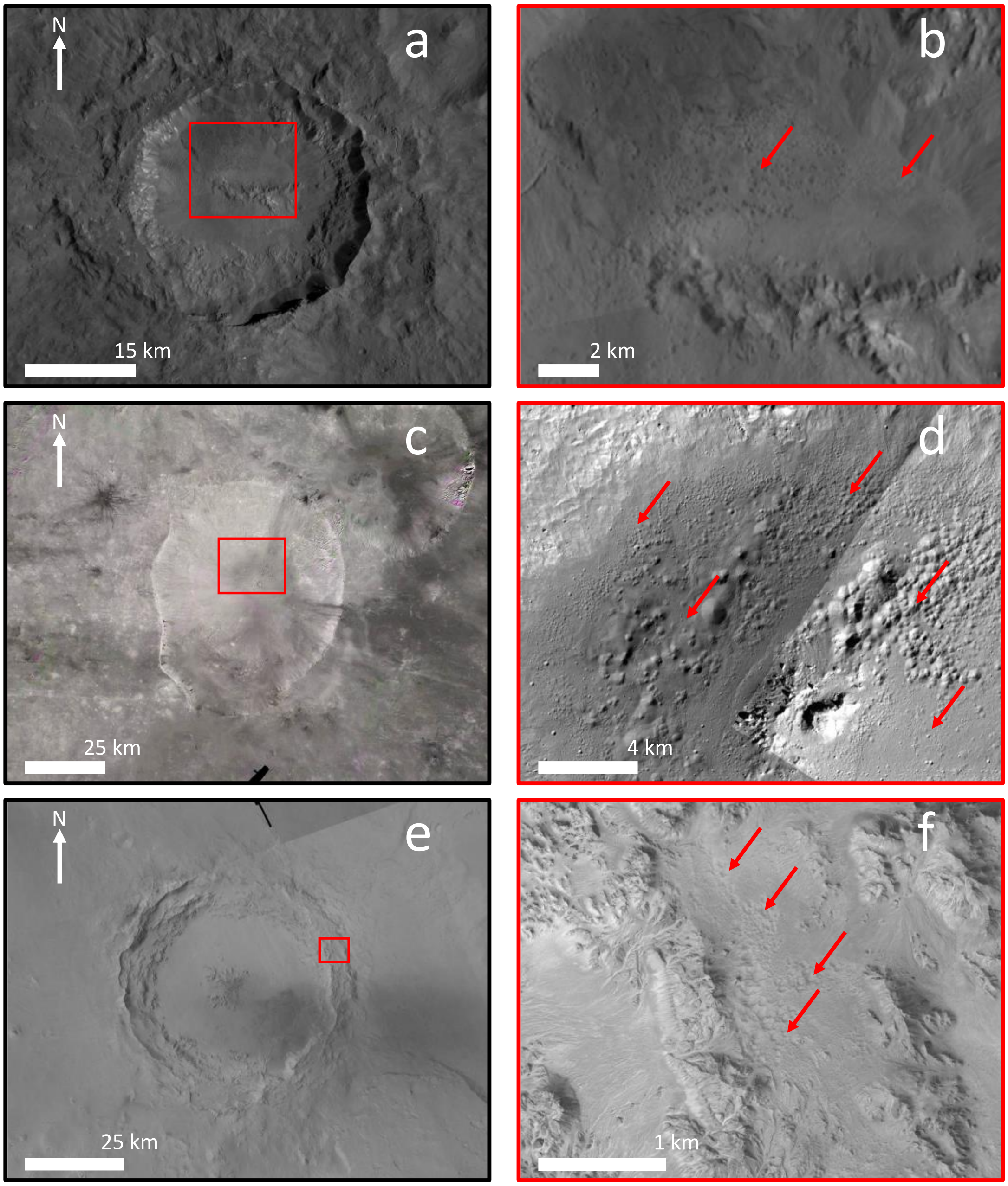

Figure 6. Morphology of impact melt/pitted materials on various planetary bodies. Symbols are the same as Figure 5. a) Haulani crater on Ceres (5.80°, 10.77°), b) inset of Haulani crater with melt ponds and pitted materials on the crater floor, c) Marcia crater on Vesta (8.98°, 339.55°), d) inset of Marcia crater with melt ponds and pitted materials on the crater floor, e) Mojave crater on Mars (7.48°, 327.01°), f) inset of Mojave crater with melt ponds and pitted materials exterior to crater. Images were made using JMARS.

1.4 Impact Melt Emplacement Hypotheses

The emplacement of impact melt is still not entirely understood. In one of the first studies to investigate the emplacement of impact melt, Hawke & Head (1977) noted that impactor angle and pre-existing impact topography both play an important role in influencing melt emplacement. Emplacement is sensitive to factors like surface gravity and impactor velocity, which in turn influence depth of craters and the amount of melt produced. Initial research suggests that impactor angle becomes the dominating factor with respect to melt distribution when impact velocities and surface gravity are high, while pre-impact topography becomes more dominant when impact velocities and surface gravity are low (Daniels, 2018; Neish et al, 2017). Mars has modest surface gravity and low impactor velocities, making it an intermediate data point in comparison the other rocky bodies. Mars has a similar gravity to Mercury, but Mercury has significantly higher impact velocities. Mercurian melt emplacement has been tentatively shown to somewhat resemble Venusian emplacement, perhaps suggesting that Mars too may resemble Venusian emplacement, if surface gravity plays the dominant role in emplacement. However, low impactor velocities for Mars may mean melt emplacement could resemble lunar emplacement, if pre-impact topography plays the more dominant role in emplacement.

1.4.1 Preimpact Topography-Controlled Emplacement

For the Moon, Neish et al. (2014) supported the hypothesis put forth by Hawke & Head, (1977) and found that pre-impact topography mainly influences the mobilization of melt exterior to the crater. They found that the exterior melt deposits of lunar complex craters are correlated with the “rim crest low” (RCL), or the lowest crater rim height, where n= 48 out of 55 for the complex crater sample population. This suggests that the melt is only able to mobilize across the lowest point of the crater rim or close to it, overcoming the lowest potential energy barrier. For this to happen, the melt is likely pushed up and over the crater rim by the rebounding uplift of the crater floor during the modification stage. This process is considered to be preimpact topography-controlled emplacement.

1.4.2 Impactor Direction-Controlled Emplacement

Chadwick & Schaber (1993) found that for Venusian craters, impactor angle was most influential to the emplacement of exterior melt deposits. The authors suggest for low incidence/oblique impacts, melt flows were found to be correlated to the downrange direction of the impact (n=55 out of a sample of 60 craters). This indicates momentum is imparted from the impactor to the melt, which subsequently pushes the melt up and over the crater rim in the downrange direction during late-stage crater formation. Impactor direction can be inferred by the asymmetry of the ejecta, where the forbidden zone – a wedge shaped lack of ejecta around a crater – indicates the uprange direction of the impactor (Gault and Wedekind, 1978; Herrick and Hessen, 2006). For example, in Figure 7, the forbidden zone of the ejecta can be seen to the east by northeast of the crater. This likely indicates that the direction of travel of the impactor was from ENE to WSW. This type of emplacement is considered to be impactor direction-controlled emplacement.

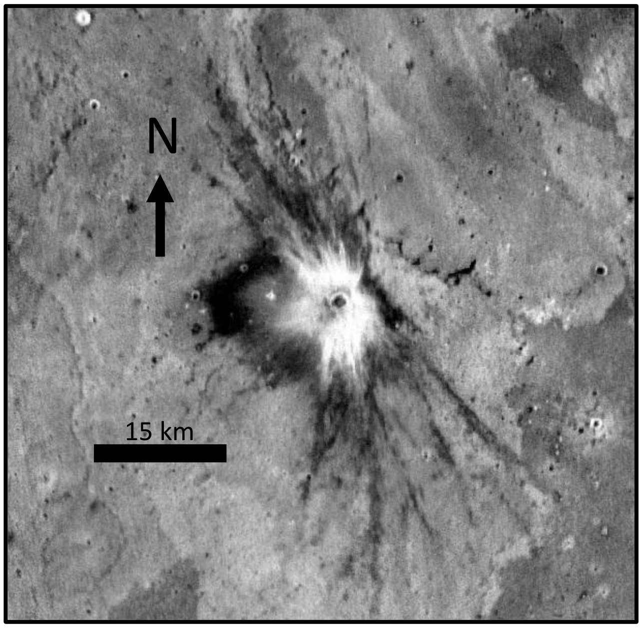

Figure 7. Rayed Martian crater Dilly (~2 km in diameter) at 13.3° N, 157.2° E with a forbidden zone to the east by northeast. Impactor direction of travel likely was from ENE to WSW (Tornabene et al., 2006). Well-preserved rayed craters on Mars are not as common as seen on the Moon (McEwen et al., 2005; Tornabene et al., 2006). Image was made using the JMARS and THEMIS Night IR 100m data.

1.4.3 Emplacement Factors

Later, Neish et al. (2017) put forward two possible explanations for why pre-existing impact topography influences emplacement for the Moon and impactor direction for Venus. They suggested surface gravity was the controlling factor for the emplacement of melt, while acknowledging that impactor velocity can play a role, too. These two factors are somewhat related; target surface gravity will draw the impactors in and increase their velocity. However, impact velocity is more strongly related to the impactor's proximity of the Sun, with impactors increasing in velocity as they accelerate towards the Sun (Schultz, 1988). The effects of velocity on the amount of melt production are squared, therefore the differences in impactor velocity can have a sizeable influence on the amount of melt produced during an impact. In addition to this, surface gravity can also influence the resultant topography of impact craters. The Moon, with its lower surface gravity, has comparatively high depth-to-diameter ratios, whereas Venus, with a higher surface gravity, has lower depth-to-diameter ratios (Ivanov et al., 1986; Pike, 1977a; Schaber et al., 1992). Figure 8 shows the trend for depth-to-diameter ratios of the inner Solar System rocky bodies, where Mars, the Moon, Earth and Mercury are represented by lines and Venus is represented by triangles. Craters with high depth-to-diameter ratios will be relatively deeper, while craters with low depth-to-diameter ratios will be relatively shallower. This depth can have a significant influence on the mobilization of melt, since melt will have a higher potential energy barrier to clear the deeper the crater. In addition to topographic influence, the amount of melt produced may also influence its ability to mobilize. For example, a large amount of melt will have more opportunity to overcome the crater rim than a small volume of melt, i.e. momentum imparted by the impactor could feasibly "push" the melt outside of the crater. Therefore, bodies with higher impactor velocities and high surface gravity (meaning large amounts of melt generated in shallower craters) will have more opportunity to mobilize melt, whereas bodies with lower impact velocities and low surface gravity (meaning small amounts of melt generated in deeper craters) will have less opportunity to mobilize melt exterior to the crater.

Neish et al. (2017) and Grieve & Cintala (1997, 1992) reasoned that a body with lower surface gravity, like the Moon, would produce a smaller volume of melt because of overall lower impact velocities and lower surface gravity, and that the melt generated would be more likely to be trapped in the crater unless it could escape at the RCL during the uplift stage. In contrast, a body with higher surface gravity, like Venus, will generally have larger volumes of melt due to higher impact velocities, and the melt can mobilize outside of the crater due to imparted momentum from the impactor. Additionally, Neish et al. (2017) note that emplacement mechanisms can take place at different times in the cratering process, depending on the planetary body. They suggest that melt emplacement on Venus would happen shortly after the start of the excavation stage, while on the Moon it would occur primarily during the modification stage.

Follow-up work by Daniels (2018) asked the same question as Neish et al. (2017), but with a focus on melt emplacement on Mercury. Mercury has modest surface gravity and high impact velocities. Therefore, Mercury’s depth-to-diameter ratio is modest, and the amount of melt produced is high. Daniels (2018) found that melt emplacement on Mercury most closely resembled that of melt emplacement on Venus rather than the Moon. They complemented the work by Neish et al. (2017) by adding a caveat that even though Mercury has lower gravity than Venus, more melt may be produced due to Mercury’s higher impact velocities (Cintala, 1992; Marchi et al. 2009; Schultz, 1988; Silber et al. 2017). The different hypothesized regimes for melt emplacement on the Moon, Mercury and Venus are shown in Figure 9.

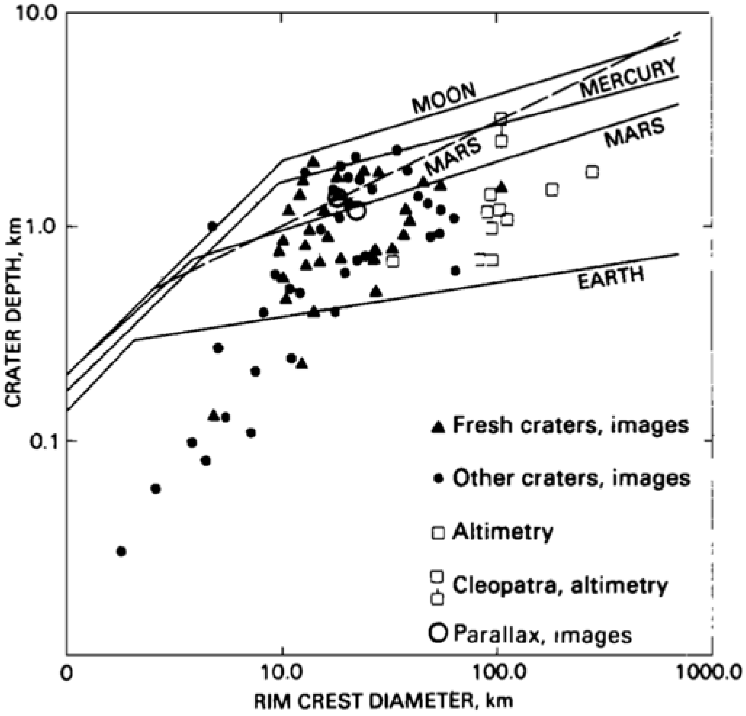

Figure 8. Trends for depth-to-diameter ratios of terrestrial bodies in the inner Solar System. Solid lines represent depth-to-diameter trends for Earth, Mars, Mercury, and the Moon. Plotted dots and triangles are individual Venusian craters. Note: The Moon has the highest ratio indicating the deepest craters, whereas Earth and Mars have lower ratios indicating shallower craters. From Schaber et al., (1992).

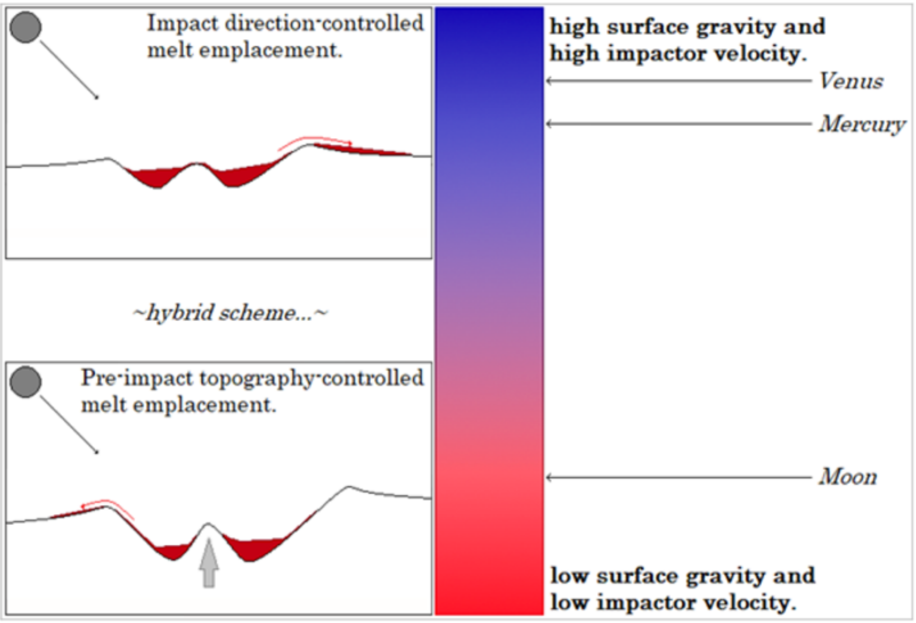

Figure 9. Hypothesized melt emplacement regimes for Venus, Mercury and the Moon. Note how Venus represents high surface gravity and high impactor velocity and the Moon represents low surface gravity and low impactor velocity. Mercury, with its modest surface gravity and high surface gravity, tends to be more Venus-like in terms of melt emplacement. Taken from Daniels (2018).

1.5 Impact Melt Emplacement about Martian Craters

The availability of data sets from HiRISE, CTX and MOLA allows for a detailed morphologic and morphometric analysis of the Martian surface. We utilize these data sets to perform a detailed study of the emplacement of impact melt deposits around Martian craters for the first time. Findings from Chadwick & Schaber (1993), Neish et al. (2014, 2017), and Daniels (2018) suggests that for lower-velocity impacts on less massive bodies, melt mobilization tends toward the RCL, whereas for higher-velocity impacts on more massive bodies, mobilization tends downrange of an oblique impactor. However, it remains unclear whether the impact velocity or the surface gravity plays a larger role in this process.

We therefore turn to Mars to understand melt emplacement on terrestrial planets. Mars provides a unique example with respect to this process due to its size and position within the solar system. To illustrate, Mars' location within the Solar System means it resides close by the main asteroid belt (the major source of impactors for Mars, as opposed to comets (Ivanov, 2001; Strom et al., 1992)). Perturbed asteroids mobilize from the asteroid belt to a Mars-crossing trajectory, is some cases resulting in a collision. The Martian impact velocity for asteroids, as studied by Ivanov (2001), is estimated at an average value of 8.62 km/s. In contrast, the average impact velocity of asteroids impacting the Moon is 19.7 km/s (Ivanov, 2001; Le Feuvre and Wieczorek, 2011), approximately 25 km/s for Venus (Tauber and Kirk, 1976), and approximately 40 km/s for Mercury (Cintala, 1992; Marchi et al., 2009). Figure 10 shows the probability distributions for impact velocities for the terrestrial planets and the Moon. The effects of velocity on the amount of melt production are squared, so the differences in impactor velocity can have a sizeable influence on melt production during an impact.

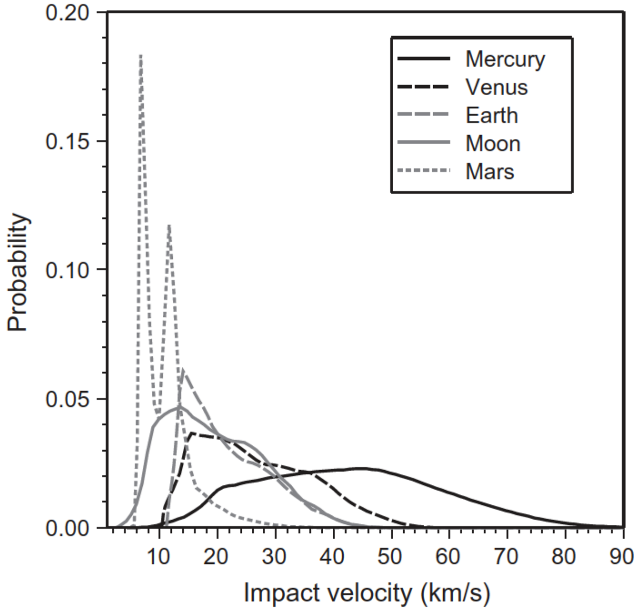

Figure 10. Graph showing the probability distribution of asteroid impact velocities for the terrestrial bodies. Make note of the high values and wide distribution of Mercurian impactors. Also of note, the probability distribution of impactor velocities for Mars is bimodal. This is likely due to the eccentricity of Mars and its proximity to the main asteroid belt (Ivanov, 2001). From Le Feuvre & Wieczorek (2011).

While the average impact velocity of Mars is the smallest among the terrestrial bodies. The mass and gravity of Mars are similar to Mercury, and in between that of the Moon and Venus. This gives us a direct comparison between the impact process on worlds with similar gravities but different impactor velocities, with the caveat that subsurface volatiles are more present on Mars, thus possibly contributing a greater role for interaction to the cratering process than for Mercury. Comparisons of impactor rate, surface gravity and impactor velocity normalized to lunar values can be seen in Table 1. However, the atmosphere of Mars poses a challenge in understanding melt emplacement. This is because the atmosphere allows for the enhanced weathering of and deposition on the surface, possibly obscuring the presence of melt. For this reason, only the most well-preserved craters will be investigated in this work.

Table 1. Mean impact velocity and surface gravity for the terrestrial planets, normalized to lunar values. Of note, while Mars has similar gravity to Mercury, the mean velocity of impactors on Mars is a quarter of that for Mercury, affecting melt production. Mars (today) represents the cratering rate for Mars over approximately the last 3 Ga. Values taken from Le Feuvre & Wieczorek (2011).

	Moon	*Mercury*	*Venus*	*Earth*	*Mars (today)*
Mean velocity ratio	1	2.16	1.28	1.04	0.54
Surface gravity ratio	1	2.2	5.3	5.9	2.2

It is important to identify the differences in melt characteristics between planetary bodies, namely the presence of pitted materials on Mars. The presence of pitted materials is likely tied to the presence of volatiles within the local target surface (Tornabene et al., 2012). However, for other planetary bodies, particularly the Moon and Mercury, pitted materials have not been observed, likely due to the volatile-poor nature of these bodies. Due to the dynamic nature of the Martian surface, crater-related pitted materials are currently the best indicator of impact melt, through remote sensing means. Therefore, we use them as a defining characteristic for our interpretation of impact melt on the Martian surface.

The well-documented presence of pits, associated with crater-related pitted materials, which is interpreted to be such bodies of melt, is often one of the first features to be degraded; therefore, craters hosting pitted materials are generally considered to be the most well-preserved (Tornabene et al., 2012). In addition, well-preserved melt deposit features can also include: distinct pond rims, cooling cracks, flat crater floors in transitional and complex craters, and albedo contrast with the surrounding material (Howard and Wilshire, 1975), although dust will often homogenize the albedo differences on Mars. The pitted materials Martian crater database compiled by Tornabene et al. (2012) serves as the source for candidate crater selection and is anticipated to provide craters providing the clearest insights into melt emplacement on Mars.

This thesis investigates and assesses melt emplacement for Mars and discusses implications for other terrestrial bodies. Chapter 1 covers a literature review and the relevant background information about impact melt emplacement and Mars. Chapter 2 details the methodologies used in this investigation. Chapter 3 compares and contrasts the results of this work with the works completed by Neish et al. (2017) and Daniels (2018) on the Moon, Venus, and Mercury. For Chapter 4, a theory is discussed and detailed to explain the differences between melt emplacement mechanisms for Mercury, Venus, the Moon, and Mars. Finally, in Chapter 5, a summary is presented of this study’s findings and future work will be elaborated upon.

Chapter 2

2 Methodology

In this section, we will cover how the data was acquired, processed, and analyzed. First, we identified the best candidate craters with exterior melt deposits for mapping and analysis. The Martian pitted materials crater database from Tornabene et al. (2012) was utilized for candidate crater selection. The database catalogues all craters that show crater-related pitted materials in some state of preservation and observed at the very least associated with the crater-fill deposits. Collectively, the craters in this database represent the mostly highly preserved craters on Mars, of which retain clear examples of deposits, which are thought to be indicative of melt-bearing bodies. Craters are validated to determine whether each candidate site has viable exterior melt that can be mapped. Particularly, candidate sites are examined within the Java Mission-planning and Analysis for Remote Sensing (JMARS) software and assessed for overlapping CTX and HiRISE coverage. The images were then checked to see if melt ponds/pitted materials exterior to the candidate crater were visible.

After validating the presence of exterior, pitted, melt-bearing deposits, CTX and HiRISE images of the site were downloaded from the Planetary Data System (PDS). We obtained MOLA data from the Mars Orbital Data Explorer, or ODE (https://ode.rsl.wustl.edu/mars/).The HiRISE images were preprocessed by the HiRISE team and were not manipulated any further for this work. The CTX images were downloaded through the Planetary Image Locator Tool (https://pilot.wr.usgs.gov/) and processed using the USGS's Integrated Software for Imagers and Spectrometers (ISIS3) software. Additionally, ISIS3 was utilized to mosaic Digital Terrain Models (DTMs) together.

Once the images of a candidate crater site were processed and collected, they were loaded into ArcMap, a Geographic Information Systems (GIS) software package that is a part of ArcGIS. This included a MOLA tile, CTX images, and HiRISE images. The crater floor, crater rim, and melt exterior to the crater rim were then identified and mapped, as will be discussed in the following sections. Finally, a statistical analysis was conducted to determine if there was any correlation between the distribution of melt and the position of the rim crest low, which will be discussed in the following chapter. The results were then compared to work by Neish et al. (2014), Neish et al. (2017), and Daniels, (2018).

2.1 Candidate Crater Selection and Mapping Conditions

The Martian crater database provided by Tornabene et al., (2012) provides a simple ranking system classifying the preservation state of each crater. The ranking system takes into account different factors of preservation, such as well-defined crater walls, a flat crater floor, in addition to the clear presence of pitted materials and the preservation state of the pits. Each crater has a designated number of stars, indicating the preservation state, where the highest ranking of five stars is given to best-preserved craters with the sharpest least degraded pits and the lowest ranking of one star is given to craters with pits that have been degraded to the point of being almost undiscernible. At the beginning of this work, the most up-to-date version of the database consisted of 277 craters on Mars, while the original published database included 204 craters. Craters from the up-to-date database with a ranking of three or more stars were considered for this work (n~141). Of the 141 craters, 14 had identifiable and extensive external pitted materials on their ejecta and had sufficient CTX and HiRISE coverage. Good image coverage to meet the objectives of this study depends on the preservation and average size of the pits. For example, Tornabene et al., (2012) showed that the average of the ten largest pits observed on the ejecta of Tooting crater (D = 27 km) was ~25 m; more than sufficient to be resolved with CTX. In this case CTX images could be utilized, but if HiRISE coverage was present it was used instead. For craters much less than 30 km, HiRISE coverage becomes more necessary and at least a third of the ejecta needs to be covered by HiRISE for the crater to be used in this work.

In a few particular cases, additional HiRISE images were acquired of candidate sites over the course of the thesis through HiWish (a publicly available image requesting website for HiRISE images, located at https://www.uahirise.org/hiwish/). Images such as ESP_058621_2205 and ESP_063933_1680 were acquired specifically for this thesis.

For the candidate sites, the correspondingly appropriate images were collected from the MOLA, CTX, and HiRISE instruments, except for Mojave and Pál craters where only MOLA and CTX were utilized. These sites had minimal HiRISE coverage, but the pitted materials were large enough to resolved by CTX images and therefore could be used in place of HiRISE images. Pál crater, for example, the entire site is mapped using CTX, shown in Figure 11. Once a crater was identified from the database, images of that site were then downloaded from the PDS through the Mars Orbital Data Explorer. An example of a candidate crater with exquisite HiRISE coverage is shown in Figure 12, where nearly all of the ejecta blanket of Resen crater is covered by HiRISE images. Maps for all of the candidate sites can be found in Appendix A.

The craters in our catalogue range in size from ~2-75 km in diameter. We did not consider impact craters smaller than roughly 2 km in diameter, because (1) less exterior melt is likely present (although exterior melt has been found in rare cases around small lunar craters, see Denevi et al., 2012 and Stopar et al., 2014), and (2) if much smaller than 2 km, craters are likely to be secondaries (McEwen et al., 2005). We did not consider impact craters larger than ~75 km in diameter, since at these scales Martian craters start resembling impact basins/protobasins. It is important to identify that protobasin morphology is transitional from complex craters to multi-ring basins. Protobasins generally exhibit a rim crest and interior ring with a central peak (see Baker, (2016) for protobasin example). Features like melt, crater rims, central peaks/pits and crater floors can be difficult to distinguish from each other in relation to the preservation state of the basin and in relation to the local topography. With a limited number of well-preserved protobasins/basins on Mars and to stay consistent with previous studies, we choose to focus on complex craters for this work.

The craters are restricted between ~50° N and 50° S. We selected this range because Robbins & Hynek (2012) found that terrain can influence the depth of Martian craters, in particular when considering high latitude craters. Beyond these latitudes, crater ejecta and pitted materials are challenging to observe and map, due to the presence of seasonal and glacial/periglacial processes overprinting/degrading them (Tornabene et al., 2012). Craters are thought to be shallower (due to crater collapse) at higher latitudes because of the higher concentration of volatiles contained within the polar Martian regolith and the subsequent interaction with heated ejecta during an impact event (Robbins and Hynek, 2012). This is important to consider when observing the distribution of melt exterior to craters, since we are interested in how melt is distributed around the crater and what role crater depth plays in the mobility of melt past the crater rim.

In this work, we predominantly focus on complex craters in order to make a comparison to previous studies' work (e.g., Neish et al., 2017; Daniels, 2018); however, of our sample population, two craters do not meet the criteria of being "complex". This includes Zumba crater, one of the best-preserved examples of a melt-bearing crater on Mars. Unfortunately, we cannot compare melt distributions around simple craters for all terrestrial planets, because simple craters on Venus are rare due the presence of a thick atmosphere, which breaks up small impactors before they reach the surface (Herrick et al., 1997; Korycansky & Zahnle, 2005). Daniels (2018) also focused on studying only complex craters on Mercury because there are very few high-resolution images of the surface and melt around smaller craters wasn't easily identifiable.

To map the melt, we defined the region of interest to be from the crater rim to the edge of the continuous (layered) ejecta. The rim was traced out by overlaying a contour layer, a DTM derived product, on top of the visible georeferenced CTX/HiRISE images and then using the Freehand tool in ArcMap to follow the steepest points around the crater rim. The continuous ejecta is defined similar to Barlow (2008) where the ejecta is composed of a continuous blanket of debris that generally extends from one to three crater radii from the crater rim. In this region of interest, we mapped multiple ejecta layers/ramparts of the continuous ejecta blanket, if present. To assess where the edge of the region of interest lay, we used the difference in elevation (contours) and difference in visual roughness as a guide. We utilized the presence of pitted materials as a guide to identify the units of impact melt. Further characterization of melt included looking for distinct associated features, such as a well-defined edge and nearby flow features, to give a higher confidence to the unit being mapped.

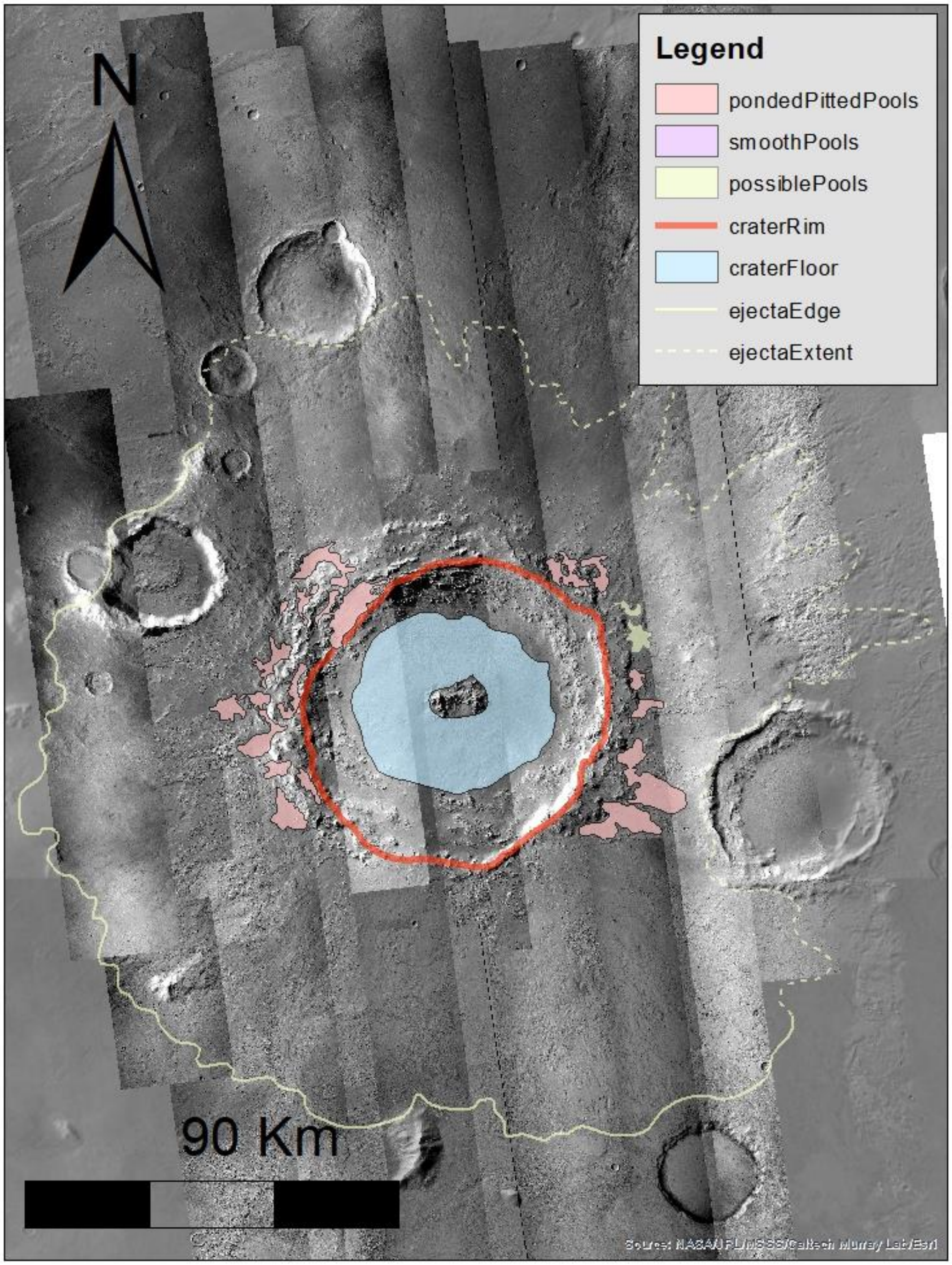

Source: NASA/JPL/MSSS/Caltech Murray Lab/Esri

Figure 11 Example of an ArcMap project with CTX-based coverage for Pál crater. Melt ponds were large enough around Pál crater to be resolved by CTX; HiRISE was not needed in this case.

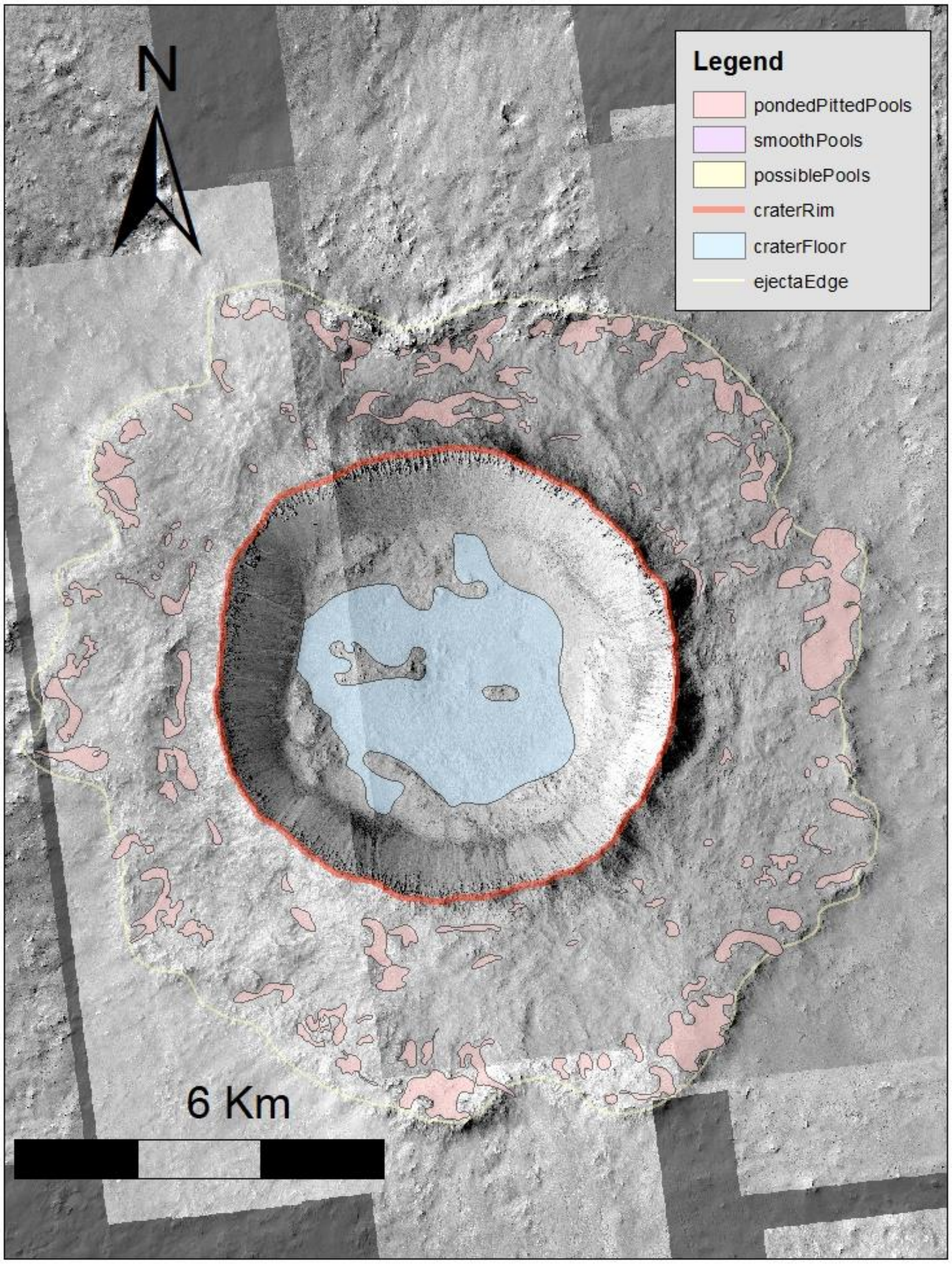

Figure 12 Example of an ArcMap project with HiRISE-based coverage for Resen crater. Almost the entire ejecta blanket has HiRISE coverage.

2.2 Data Processing

Below, we give a step-by-step review of the data processing for each dataset that was utilized. Additionally, we provide a section on the creation of higher-level data products like Digital Terrain Models (DTM).

2.2.1 MOLA

The MOLA data were downloaded from the Mars ODE. This includes the .IMG file and the associated .LBL file, where the .IMG file is the disk image file and the .LBL is the label, or header, file. The associated .LBL file contains key metadata about the image, such as emission angle, incidence angle and phase angle. The MOLA tiles did not need to be manipulated any further. From here, the MOLA tile could be loaded into ArcMap.

2.2.2 CTX

The CTX images were downloaded from the Mars ODE. They were then run through a series of ISIS3 commands in order to process the images. An in-house bash script was made in order to speed the processing of the CTX images without intervention by the user.

The first step, *mroctx2isis*, converts the raw PDS image file into a .cub file, an ISIS3 friendly format. Next, the spacecraft and image variables (e.g., observation angles, etc.) are associated with the image with the *spiceinit* command. This step is important as it associates the camera's metadata and geometry with the image itself. The image then goes through *ctxcal*, which radiometrically calibrates the image. From here, *ctxevenodd* is executed in order to remove a systematic image anomaly from the CTX images. Next, *cam2map* is run to convert the image to a map projection. Finally, *gdal_translate* is executed in order to convert the image into an ArcMap friendly format (a .tif file). At this stage, the image has been fully processed and is ready to be loaded into ArcMap for further analysis.

A recent data product made available has been the new CTX global mosaic map layer by Dickson, Kerber, & Ehlmann (2018) for JMARS and ArcMap. It has provided unprecedented resolution detail of Mars on a global scale. However, exterior melt ponds can exist below the resolution of CTX images, therefore utilizing this data product can provide a quick way to assess whether HiRISE coverage is needed for the highest-resolution identification of the smallest melt ponds.

2.2.3 HiRISE

HiRISE images are unique in the sense that the image data often requires minimal processing. Images are first downloaded from the PDS through the Mars ODE. They come in the form of .JP2 and .LBL files, which can be directly loaded into ArcMap.

2.2.4 DTM Production

One of the higher-level data products that we created in this work are DTMs. They predominantly serve as a basis for determining the rim crest low about crater rims. The rim crest was traced through the synthesis of visual and elevation data.

After a candidate crater site is selected, the crater is then assessed for images that could be made into a DTM. A sufficient DTM could be made if the images are suitably overlapping each other, the emission angle between the images are adequately spaced apart (e.g. A difference in emission angle of about 20º from opposite camera looking angles would be acceptable, whereas a difference in emission angle of about 10º from the same camera looking angle would be unacceptable.), and if the terrain wasn’t too flat or too extreme, generally. For most places on Mars, there is sufficient CTX coverage to create a CTX DTM, which generally have a vertical resolution of about 6 m. For candidate complex crater sites, the melt ponds associated with them can be large enough to be resolved by a CTX DTM. However, for candidate transitional and simple craters (those that are up to about 9 km in diameter on Mars), the associated melt ponds are generally smaller than their complex crater counterparts and therefore require a HiRISE DTM to resolve their melt deposits.

To make both a HiRISE and CTX DTM, we utilize the NASA Ames Stereo Pipeline (ASP). The pipeline is a suite of tools that enable stereo processing of planetary satellite images. First, *hiedr2mosaic.py* is run to prepare the images for further processing. This step includes applying a number of ISIS3 calibration commands to the stereo images, such as *spiceinit.* Next, *cam2map4stereo.py* is executed to register the images to a common map projection system and area. It also resamples the images to a matching resolution. The resolution of the DTM will only be as good as the worst-resolution image that was provided. The heart of the ASP is the tool *stereo*, which is run next. Here, the computer creates a series of autonomously generated tie-points between the two images. These points are then assessed for how close they match in each image based on a collection of neighboring pixel values, where the points that fall outside a tolerance range are then excluded. The images are then co-registered with each other and a point cloud is made. *Point2dem*, the final step, converts the point cloud to a GeoTIFF terrain model. At this point the DTM is complete and can be uploaded to ArcMap. From here, data products like contours or a slope-derived map can be made through ArcMap while using the DTM as the base product. Figure 13 shows a HiRISE DTM of Zumba crater with contours overlain at 20 m intervals.

DTMs also provide elevation data that can possibly be used to identify melt ponds. As reasoned by Tornabene et al. (2012), the surface of melt ponds should be roughly equipotential, meaning that the slope of the surface should be roughly flat. If true, melt ponds should have slope measurements that are roughly horizontal and the ejecta that encompasses the melt ponds should be slightly inclined. Figure 14 shows the mapping technique utilizing a HiRISE DTM-derived slope data product in order to map the distribution of melt ponds for Zumba crater.

DTMs provide useful contextual information but they come with a few caveats. The spatial resolution of a CTX DTM is often too low (~20 m resolution in the XY-direction and ~6 m in the Z-direction) to assess the slope of each melt pond. HiRISE DTMs are more favorable for assessing the slope of putative melt ponds as the vertical resolution is on the order of tens of centimeters (~0.3 m). DTMs made with the ASP can also have systematic and random errors. Systematic errors might include an image from a stereo pair that has been misaligned or mis-projected, possibly due to pointing errors of the camera or misregistration of tie points made by the computer. This could result in tilting, warping, or an offset in the final DTM. Random errors in the DTM could be caused by the mis-registration of tie points to certain geologic features. For example, flat and/or heavily sandy areas can often be hard for the ASP to find good registration points to make the final DTM, resulting in an incorrectly warped image. Additionally, we acknowledge that the DTMs have not been registered to MOLA data and therefore the DTMs are only accurate in a relative sense. Both HiRISE and CTX slope data products appear quite noisy, which is particularly observable when stretching the slope range to just a few degrees. The amplitude of slope noise can rival the amplitude of the (presumably) mostly flat surfaces. Therefore, we encourage caution when incorporating DTM data into mapping efforts.

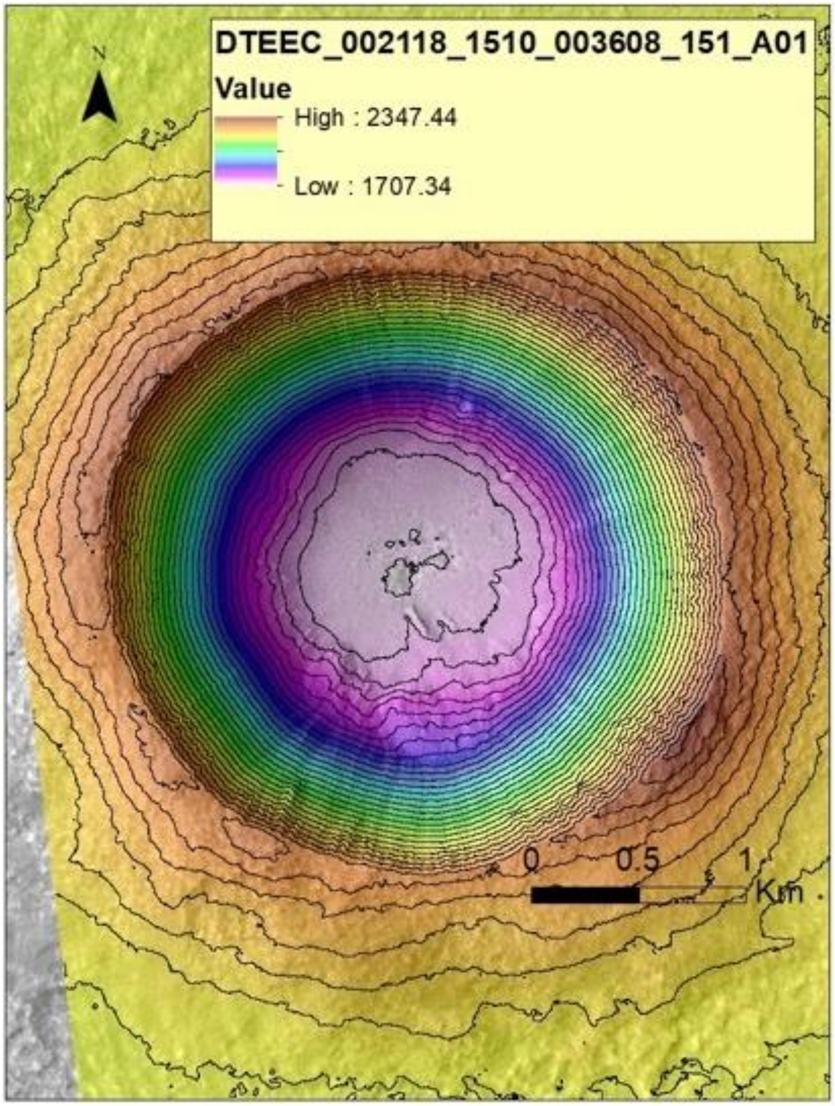

Figure 13. HiRISE DTM of Zumba crater. Black lines represent contours at 20 m intervals.

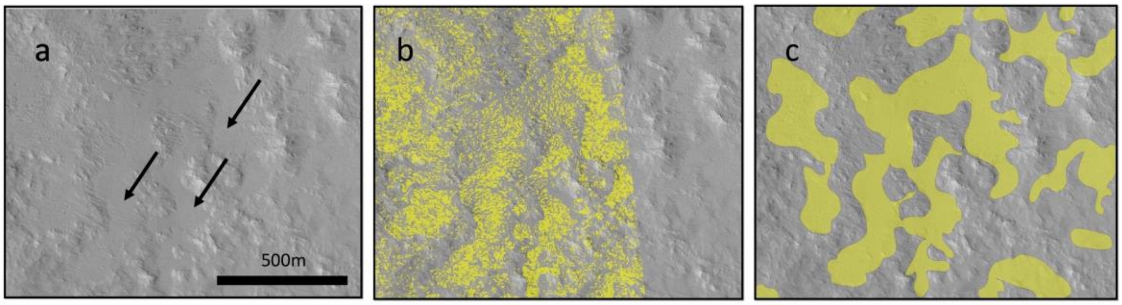

Figure 14. Ejecta and melt to the east of Zumba crater. North is up. (a) HiRISE image PSP_003608_1510 of Zumba ejecta. Black arrows point to putative melt-bearing deposits. (b) Slope data derived from a HiRISE DTM of Zumba crater, where yellow represents a slope of five degrees or less. The clusters of yellow pixels can be interpreted to be melt ponds with a roughly equipotential surface. (c) A synthesis of the visual and DTM-based analysis used to map melt bearing deposits.

2.3 Data Analysis

Once the data was collected and processed, ArcMap was utilized to identify and map the distribution of exterior melt deposits. New shape layers were created to identify the units of ponded and pitted materials, smooth ponded materials, the crater rim, the crater floor, ejecta edge and ejecta extent. The units were then traced within ArcMap Editor using the Freehand tool, keeping in mind the defining characteristics of melt ponds. As previously mentioned, a collection of criteria, such as distinct ponds edges, nearby flow features, and the presence of pitted materials were employed in determining each type of unit. An effort was made to distinguish between units of smooth and pitted melt ponds. We defined the ejecta edge to be the edge of rampart crater ejecta, where there is a notable difference in elevation between the ejecta and the local topography, and where there was a distinct change in surface roughness. The ejecta extent unit is related to the ejecta edge unit with the caveat that the rampart edge is not clearly defined, but a difference in surface roughness is noted; this unit is an approximation of the extent to which the ejecta lays. Once all of the shape layers were created, we analyzed how the melt pond distribution related to the local topography.

2.3.1 Rim Crest Low and Melt Deposit Distribution

The rim crest low, or RCL, was calculated using the Zonal Statistics tool within ArcMap on the crater rim shapefile. The tool computes a variety of simple statistical properties for the topographic profile extracted from the shapefile, including the maximum, minimum, mean and standard deviation. By running the Zonal Statistics tool on the trace of the crater rim and elevation data products, we can obtain the minimum and maximum of our rim crest elevation. Figure 15 shows the elevation profile for Noord crater.

Additionally, a second part of our analysis calculated the rim-to-floor depth of each crater. The ArcGIS tool Contours was utilized to help trace out a polygon in the crater floor. Central peaks and pits were avoided during polygon tracing in order to obtain a more accurate crater floor measurement. Again, the Zonal Statistics tool was utilized to obtain an average floor depth and standard deviation within the polygon.

Melt deposit distribution was assessed and estimated visually in relation to the crater. The distribution of melt ponds around each crater was not always straightforward as there may exist multiple groupings of melt around each crater. When this was the case, each grouping was listed in the spreadsheet.

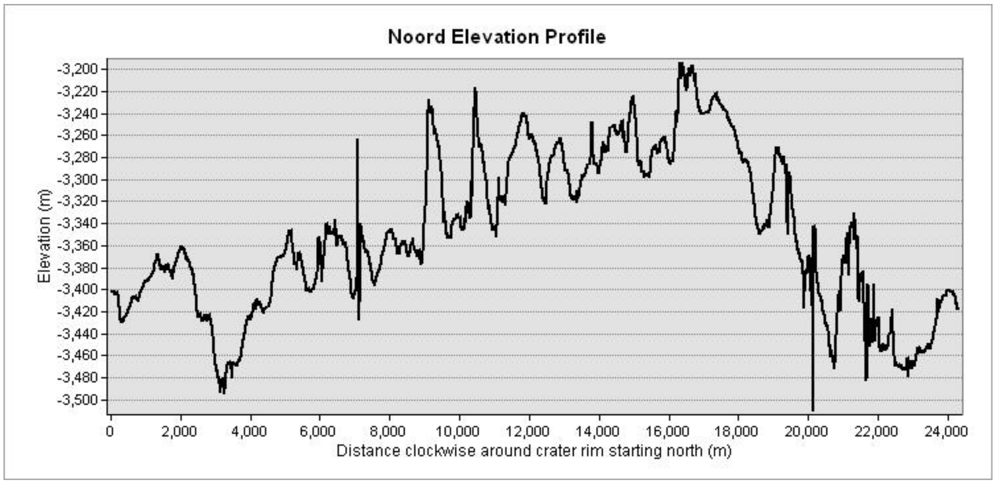

Figure 15 Rim Elevation for Noord crater. The elevation profile starts on the northernmost point of the crater rim, then circles clockwise around the crater until north is reached again. The RCL is between 3,000 - 4,000 m on the x-axis, corresponding to a RCL direction of northeast.

Chapter 3

3 Results

In this work, 14 impact craters on Mars were identified that showed evidence for exterior melt-bearing material. Below, Table 2 and Table 3 have been composed detailing the results of this work.

3.1 Final Crater Catalogue

In the final crater catalogue, values for latitude, longitude, crater diameter, melt direction(s), RCL direction, rim crest elevation difference, rim crest elevation difference error, crater depth, crater depth error, R value, and R value error were recorded for each crater, as detailed in Table 2 and Table 3. In this catalogue, we separate craters into two broad categories: simple and complex. We acknowledge that a number of craters (n=7) fall within the transitional crater range for Mars, ~4-12 km in diameter (Tornabene et al., 2018). However, after careful inspection of each crater, a designation of simple or complex was made in order to simplify crater comparison, with the exception of Istok, which is a transitional crater. Of the fourteen craters in the catalogue, twelve are considered to be complex; the exceptions are Zumba and Istok crater.

Candidate craters exhibit multiple lines of evidence towards the existence of melt at their corresponding locations. A candidate crater was required to have at least two distinct features of melt, such as pitted materials in the crater floor and dissection – eroded channel-like features – near putative exterior melt-bearing material, in order to be viable for mapping. Additional melt features include distinct pond rims, pitted materials within putative exterior melt, a flat crater floor, lobate flows, and/or a flat elevation slope of supposed exterior melt.

3.1.1 Sources of Error

In this section, we report on the source and degree of error for the final crater catalogue. We report error for the measurement of the rim crest elevation difference, crater depth, and R value in Table 3. Error for the rim crest elevation difference was measured by propagating the error in the two values being subtracted (i.e. the CTX DEM vertical resolution of 6 m) in quadrature. Error for the crater depth was based on the standard deviation of the crater rim elevation and the crater floor elevation and was also propagated in quadrature. Error for the R value measurement was based off the rim crest elevation difference and crater depth and was similarly propagated in quadrature.

Additionally, there is an element of subjectivity when it comes to determining the rim crest low and the direction of the melt deposit distribution. For example, for the rim crest low, a number of elevation profiles showed multiple possible low elevation regions, but only the lowest point on the profile was taken as the rim crest low. The RCL was measured by utilizing the Zonal Statistics tool within ArcMap to assist in eliminating subjective interpretation of the lowest point along the crater rim. Determining the melt deposit distribution was done by eye and so there is a degree of interpretation as to where the melt lies in relation to the crater. One of the more challenging examples, for example, is Resen crater, seen in Appendix A Figure 9. Here, melt ponds are distributed rather evenly around the crater making it difficult to determine where the largest ponds lie. In follow up work, it may prove beneficial to divide the ejecta into wedges and to then determine the area covered by melt ponds within each wedge to assess which wedge has the largest fraction of melt present.

Further assessment could be made if the second lowest point in the crater rim was measured against the melt deposit distribution direction. This would likely skew the results away from the “coincide” classification. This is because if more than one RCL was available, the one closest to the primary melt deposit was taken to assess the separation angle from the RCL.

Table 2. Final crater catalogue for 14 Martian craters analyzed in this study. This table shows the latitude, longitude, crater diameter, melt direction and RCL direction of each crater.

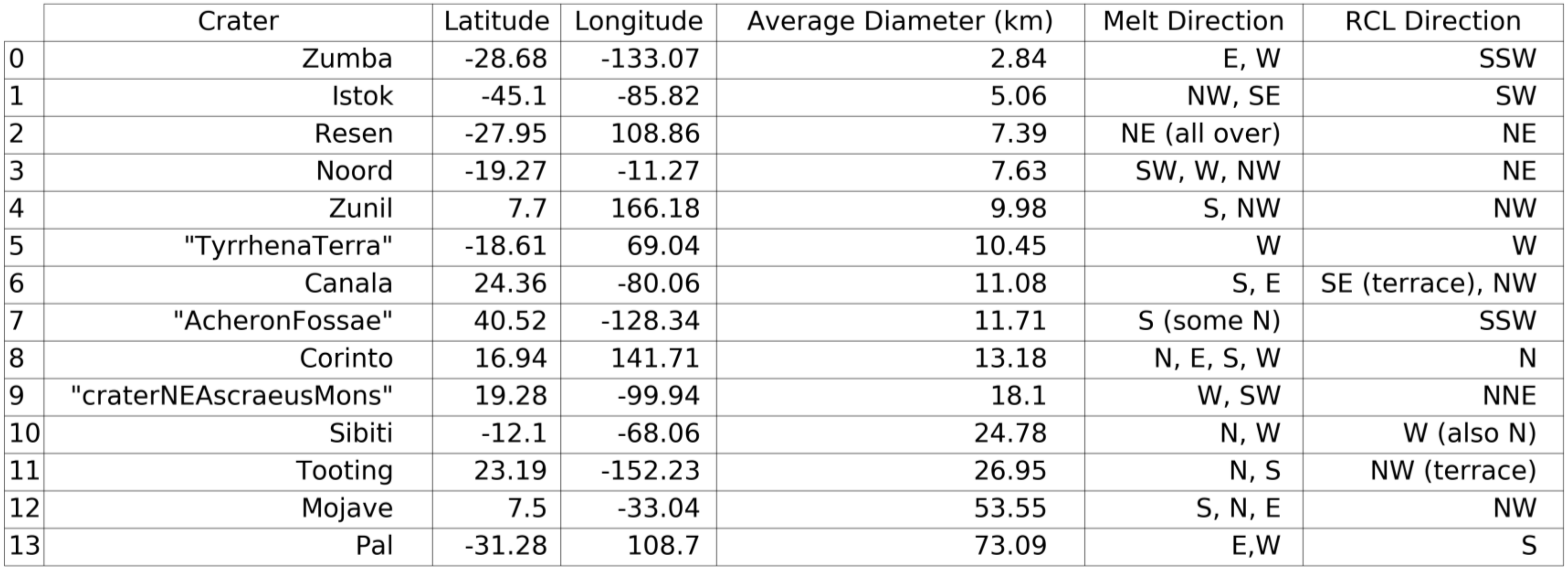

	Crater	Latitude	Longitude	Average Diameter (km)	Melt Direction	RCL Direction
0	Zumba	-28.68	-133.07	2.84	E, W	SSW
1	Istok	-45.1	-85.82	5.06	NW, SE	SW
2	Resen	-27.95	108.86	7.39	NE (all over)	NE
3	Noord	-19.27	-11.27	7.63	SW, W, NW	NE
4	Zunil	7.7	166.18	9.98	S, NW	NW
5	"TyrrhenaTerra"	-18.61	69.04	10.45	W	W
6	Canala	24.36	-80.06	11.08	S, E	SE (terrace), NW
7	"AcheronFossae"	40.52	-128.34	11.71	S (some N)	SSW
8	Corinto	16.94	141.71	13.18	N, E, S, W	N
9	"craterNEAscraeusMons"	19.28	-99.94	18.1	W, SW	NNE
10	Sibiti	-12.1	-68.06	24.78	N, W	W (also N)
11	Tooting	23.19	-152.23	26.95	N, S	NW (terrace)
12	Mojave	7.5	-33.04	53.55	S, N, E	NW
13	Pal	-31.28	108.7	73.09	E,W	S

Table 3. Final crater catalogue for 14 Martian craters analyzed in this study. This table shows the difference in rim elevation (from the rim crest low to the rim crest high), depths measured for each crater, and the calculated R value, where the R value represent the difference in rim height normalized to the crater depth. Errors were propagated in quadrature from each measurement.

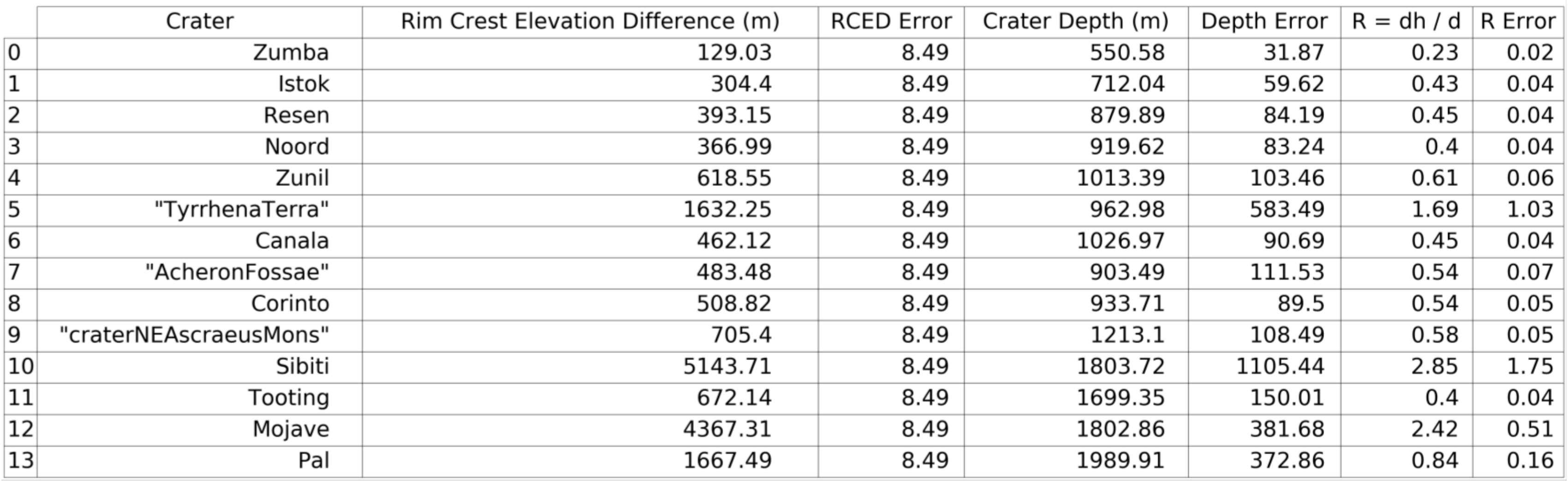

	Crater	Rim Crest Elevation Difference (m)	RCED Error	Crater Depth (m)	Depth Error	R = dh / d	R Error
0	Zumba	129.03	8.49	550.58	31.87	0.23	0.02
1	Istok	304.4	8.49	712.04	59.62	0.43	0.04
2	Resen	393.15	8.49	879.89	84.19	0.45	0.04
3	Noord	366.99	8.49	919.62	83.24	0.4	0.04
4	Zunil	618.55	8.49	1013.39	103.46	0.61	0.06
5	"TyrrhenaTerra"	1632.25	8.49	962.98	583.49	1.69	1.03
6	Canala	462.12	8.49	1026.97	90.69	0.45	0.04
7	"AcheronFossae"	483.48	8.49	903.49	111.53	0.54	0.07
8	Corinto	508.82	8.49	933.71	89.5	0.54	0.05
9	"craterNEAscraeusMons"	705.4	8.49	1213.1	108.49	0.58	0.05
10	Sibiti	5143.71	8.49	1803.72	1105.44	2.85	1.75
11	Tooting	672.14	8.49	1699.35	150.01	0.4	0.04
12	Mojave	4367.31	8.49	1802.86	381.68	2.42	0.51
13	Pal	1667.49	8.49	1989.91	372.86	0.84	0.16

3.2 Mapping Results: Distribution of Melt Deposits

The distribution of mapped melt deposits will be covered in this section. We defined the region of interest for each candidate crater to be from the crater rim to the edge of the continuous ejecta. We also define a melt deposit to be a cluster of melt ponds. The melt deposit distribution showed interesting results. Patterns that we observed include: 1) multiple deposits around one impact crater, 2) deposit symmetry (e.g. roughly equal deposits distributions to the east and west of a crater), and 3) extreme topography resulting in deposits skewed towards the topographic low.

One observation to note is that most of the craters in the catalogue exhibit more than one melt deposit. Multiple clusters of melt ponds were often present in the ejecta. This made assessing melt deposit direction a challenge. For example, in Figure 12, Resen crater has a number of melt deposits, relatively evenly distributed around the ejecta. In this case, since there was a large melt pond to the north, the melt deposit direction was taken to be north. Because there is a degree of subjectivity to this interpretation, one could also argue that there is no preferred melt deposit distribution direction for Resen crater. A similar challenge was encountered with Sibiti crater, in Figure 16, where the melt deposits could be argued to be to the north or to the west of the crater. Since the melt ponds were denser and larger to the north, that is the direction we chose for the melt direction.

Another observation we made about the melt deposit distribution is the relative symmetry of some of the distributions. Candidates crater sites Istok and Zumba (Appendix A Figure 5 and Appendix A Figure 13), have melt distributions that are relatively symmetrical along an axis possibly associated with impactor direction. Interestingly, Pál crater also shows similar symmetry to the east and west of the crater, in Appendix A Figure 8.

Symmetry is not seen everywhere, however. In the case of candidate sites in extreme topography the melt direction is particularly skewed towards the local topographic lows. For example, for the three extreme topography candidate sites, “AcheronFossae”

(Appendix A Figure 1), Sibiti (Appendix A Figure 10), and “TyrhenaTerra” (Appendix A Figure 12), melt distributions have been heavily influenced by topography.

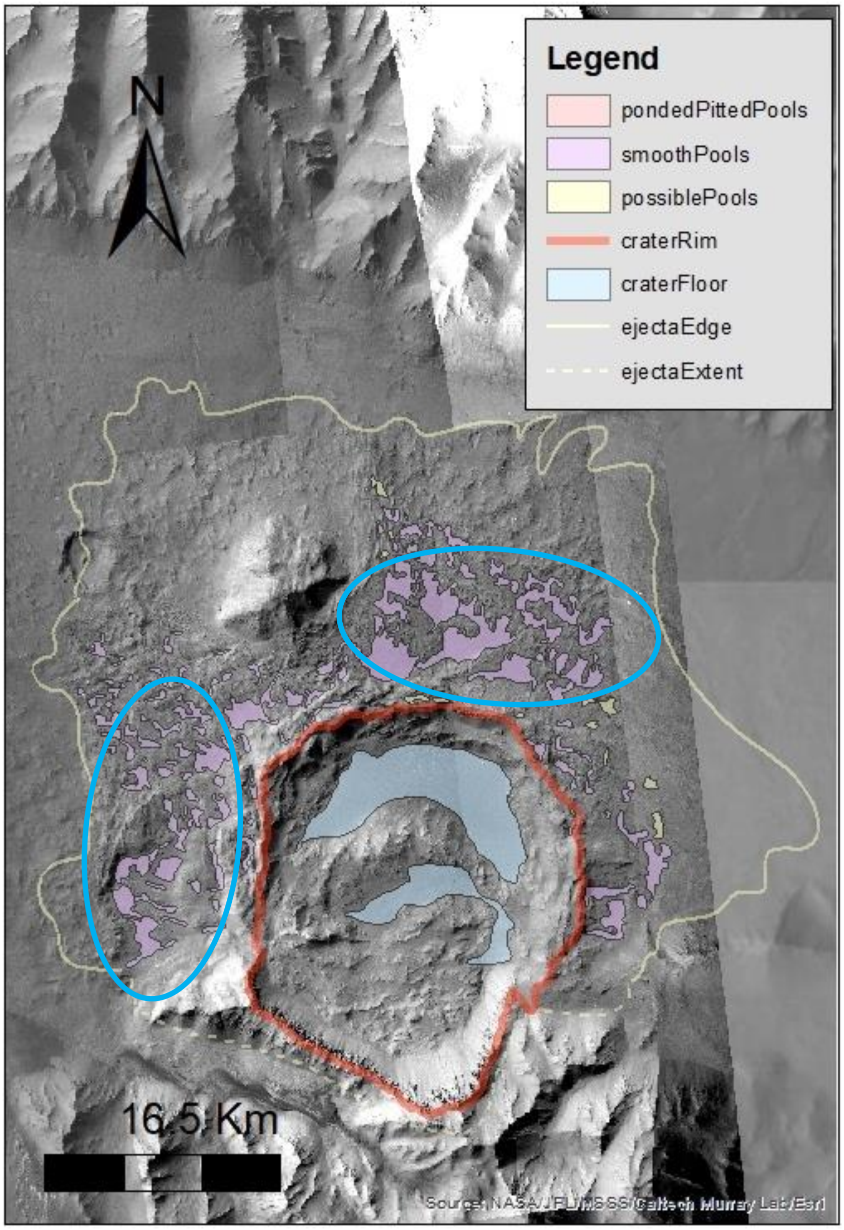

Figure 16 Candidate site Sibiti crater. In some cases, the melt deposit distribution can be a challenge to assess; for this candidate site two major clusters of melt ponds can be gleaned to the north and to the west (outlined in blue). Because of the denser distribution of larger ponds, the primary melt direction for this crater was assumed to be to the north.

3.3 Melt Distribution Relation to Rim Crest Low (RCL)

The crater depth and rim crest variation were determined for each mapped crater in our catalogue. The rim crest low was determined by analyzing CTX DTMs of each site, the collection of which can be found in Appendix B. We calculated the degree of separation between the direction of the distribution of melt-bearing deposits and the direction of the RCL. To categorize the degree of separation, four distinct groupings are made. The first grouping, "coincide", is defined as the distribution of melt occurring at the same angle as the RCL. The second grouping, "within 45°", refers to the distribution of melt being within 45° of the RCL. "Within 90" refers to the melt distribution being within 90° of the RCL. The fourth regime, "90° or greater", refers to the melt distribution being at or greater than 90° from the RCL. The direction of melt to the RCL does not exceed 180°. For example, candidate crater "craterNEAscreausMons", shown in Appendix A Figure 4, shows a predominant melt direction to the west and an RCL to the north by northeast; therefore, the degree of separation is considered to be "90° or greater". In the case of multiple melt directions, the degree of separation of RCL to the closest melt-bearing deposit was recorded. For example, Zunil crater, shown in Appendix A Figure 14, shows multiple melt directions, one to the northwest and another to the south. The RCL was determined to be towards the northwest; therefore, the degree of separation for Zunil is 0.

Of the fourteen mapped craters, five craters fall within "coincide", one crater falls under "within 45°", four craters fall under "within 90°", and the remaining four craters are classified as "90° or greater". Of the fourteen mapped craters, twelve are considered complex, where Zumba crater is considered simple, and Istok is considered transitional. Zumba is classified as "within 90°" and Istok is classified as "90° or greater", the remaining twelve craters have been plotted as a stacked bar chart in Figure 17. We have plotted the R values of all craters in our catalogue in Figure 18, and the cumulative distribution function of R for each of the terrestrial bodies in Figure 19.

3.4 Anderson-Darling Goodness-of-Fit

The data in our catalogue, particularly the degree of separation between the melt distribution and the rim crest low, is plotted against that of previous work on Mercury by

Daniels (2018) and on Venus and the Moon by Neish et al. (2017) (shown in Figure 17). To assess the role that topographic variation plays in melt emplacement on Mars, we use a statistical analysis to determine how well the Martian melt distribution correlates to the RCL. We apply the Anderson-Darling goodness-of-fit technique to determine if Martian craters follow the same distribution as that on Venus, the Moon, or Mercury.

$$A^2 = n\int \frac{\left(F_n(R) - F(R)\right)^2}{F(R)\left(1 - F(R)\right)} dR$$

The equation above shows the Anderson Darling equation in its integral form. The A^2 value represents the Anderson-Darling statistic and can be used to find associated p-values, n represents the sample size, F(R) represents the cumulative probability distribution of the known datasets (i.e. the Venusian, lunar and Mercurian datasets), and F_n(R) represents the cumulative probability distribution of the measured dataset (i.e. the Mars dataset).

The Anderson-Darling goodness-of-fit technique determines how well a collection of data points match a particular distribution. The probability of observing some value of A^2 by chance increases with the increasing difference between the data and the model probability distribution.

Using the calculated A^2 value, we can calculate the *p* value for our hypothesis. We have two separate hypotheses when it comes to the Anderson-Darling test; the data follow the given distribution, or the data do not follow the given distribution. The distributions in our case are the Venusian, lunar, and Mercurian data sets and the data is our Martian distribution. If the data follow the given distribution, then the hypothesis is true. In other words, a high *p* value would indicate that the observed result is likely representative of the given distribution. If the *p* value is low, then the null hypothesis is true and the data is likely not part of the given distribution.

We have calculated the multivariate Anderson Darling goodness-of-fit statistic for the distribution of R values – a value that represent the range of heights, from the rim crest low to the rim crest high, normalized to depth of the crater – and degree of separation of melt from the RCL for Mars against the distributions for Mercury, Venus, and the Moon. We have found *p* values for the comparison against the Venusian distribution to be *p*=0.009, against the lunar distribution to be *p*=0.097, and against the Mercurian distribution to be *p*=0.493. Thus, the Martian distribution is unlike the lunar and Venusian distributions, and more similar to the and Mercurian distribution.

We have also calculated the AD statistic for the Martian distribution with cases of extreme topography removed. We have specifically removed candidate sites "AcheronFossae", Sibiti, and "TyrrhenaTerra" for this calculation. This is because the melt directions for these sites is inextricably influenced by the local topography; "AcheronFossae" is an impact into a preexisting crater, Sibiti crater is in the side of a canyon wall, and "TyrrhenaTerra" is in the wall of a much larger crater. We have found *p* values without extreme topographic influences (n=9) compared to the Venusian distribution to be *p*=0.109, against the lunar distribution to be *p*=0.122, and against the Mercurian distribution to be *p*=0.600. However, we acknowledge the small sample size of our Martian distribution compared to the lunar (n=49), Venus (n=21), and Mercury (n=24) distributions.

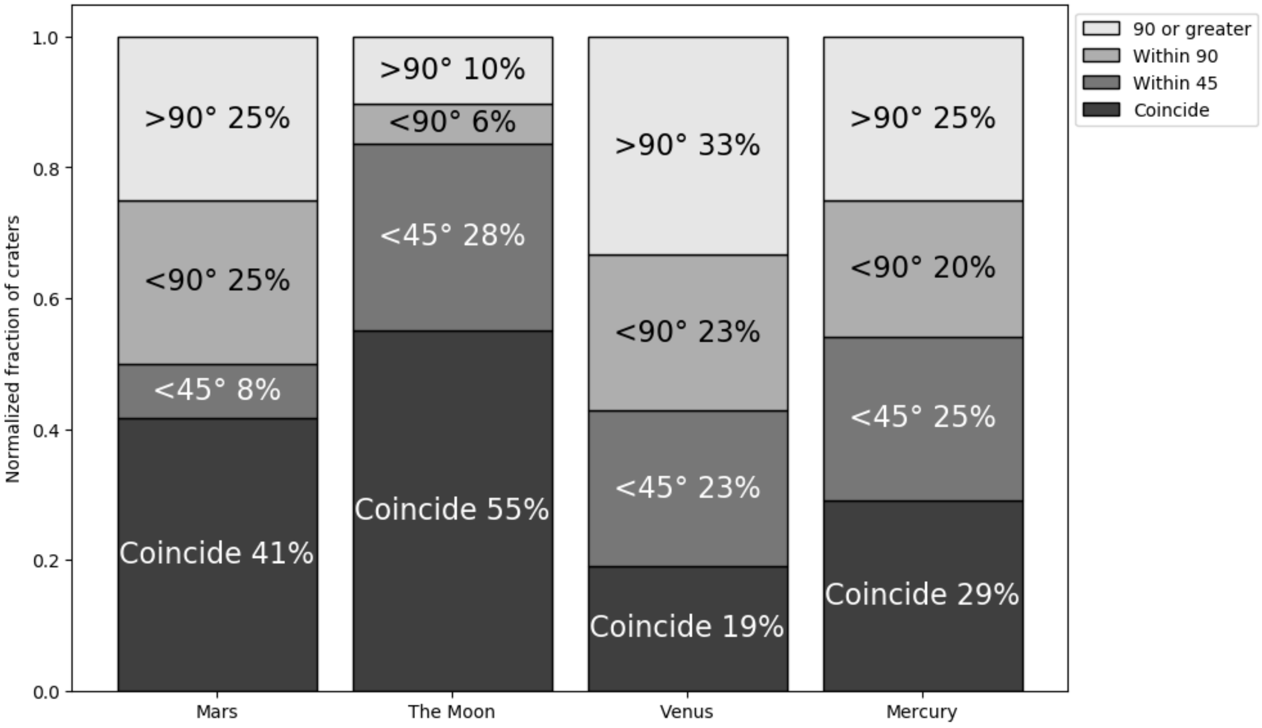

Figure 17 Stacked bar chart showing the relative amounts of each degree of separation classification for Mars, the Moon, Venus and Mercury. The number of complex craters studied for each world are as follows: Mars (n=12), the Moon (n=49), Venus (n=21), and Mercury (n=24). Included in the Martian distribution are the three complex craters with extreme topography, which are described in the text, where two "coincide" and one is "within 45" of the RCL. Of note, the lunar distribution seems unique amongst these four bodies, where more than 80% of studied craters "coincide" or are "within 45" of the RCL, suggesting a different emplacement process for the Moon.

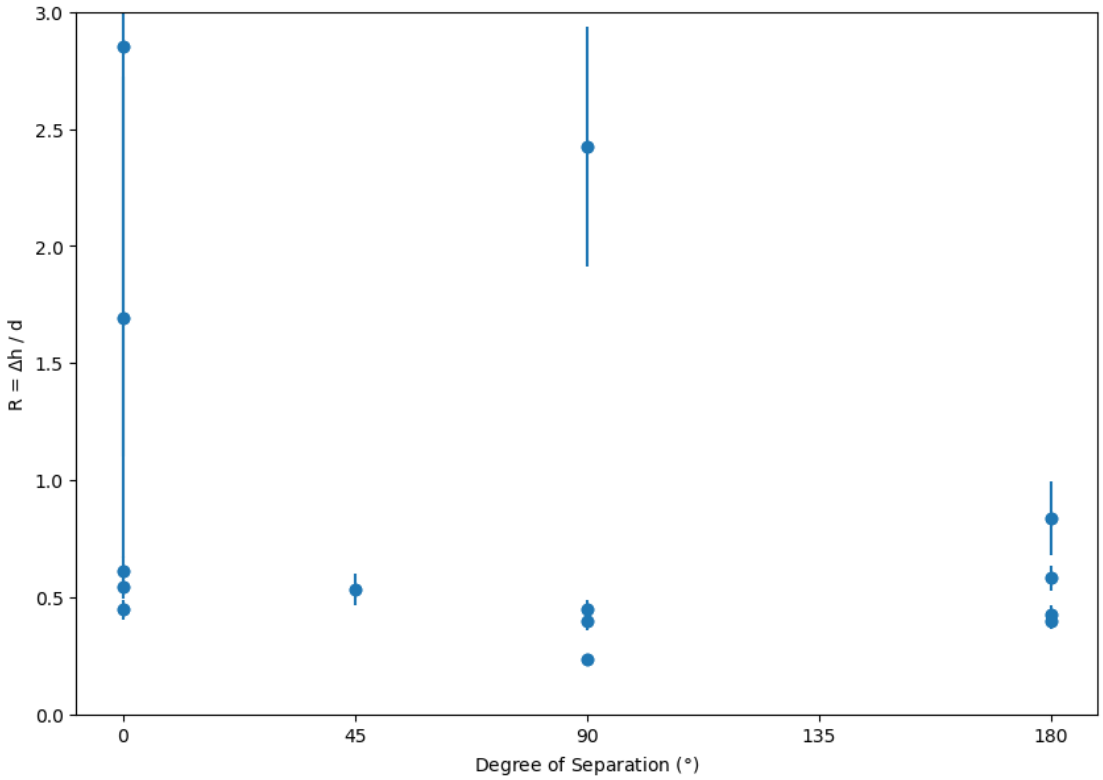

Figure 18 R value plotted against the degree of separation. R represents the range of heights of a crater rim divided by the crater depth. Degree of separation refers to the separation between the melt deposit distribution and the rim crest low. Generally, the more variable the topography, the larger the errors. The y-axis is cut off at 3, but the error bar for a point that lies at 0 degrees of separation extends beyond.

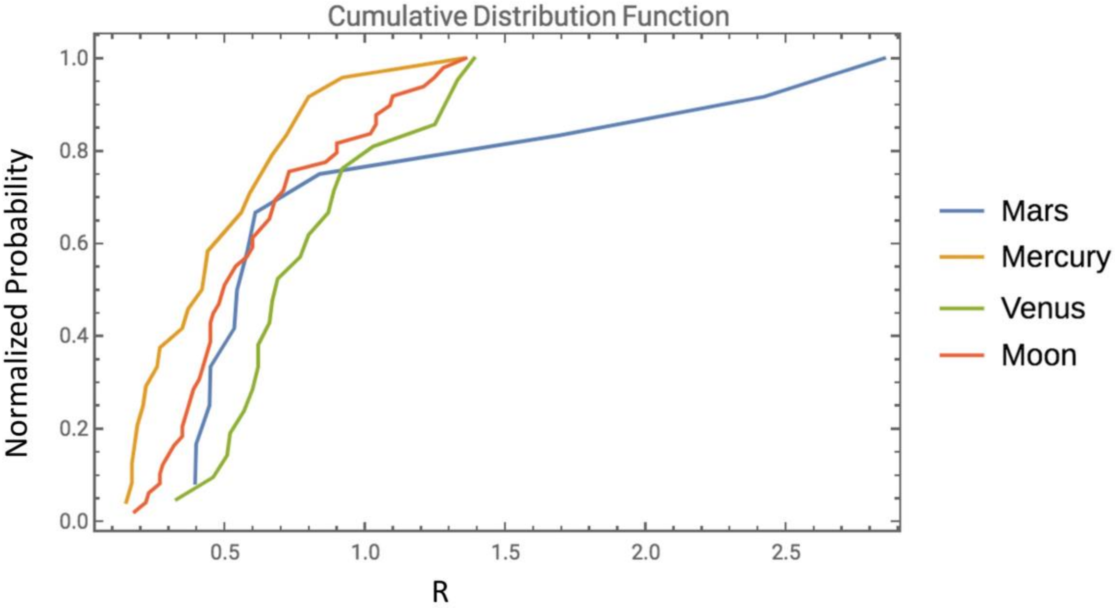

Figure 19 Cumulative distribution function showing the normalized probability of observing any particular value of R for the terrestrial bodies.

Chapter 4

4 Discussion

This work is an important building block in understanding impact melt emplacement on different planetary bodies within the Solar System. Mars is a key connecting bridge between the other terrestrial planets because it offers a world that has relatively low impactor velocities, with moderate gravity similar to that of Mercury. In this chapter, we will discuss the roles of impactor velocity and surface gravity in the impact cratering process, and their implications for melt emplacement. We will also discuss the limitations of this work and future directions for this research.

4.1 Relation to Other Bodies

In this work, we have tentatively found that melt emplacement on Mars may resemble Mercurian melt emplacement more closely than lunar or Venusian-style emplacement for our limited data set. We have calculated the multivariate Anderson Darling goodness-of-fit statistic for the distribution of R values for Mars against the distributions for Mercury, Venus, and the Moon. For our catalogue of complex craters (n=12), we have found *p* values that indicate more correlation with the Venusian (*p*=0.009, n=21) and Mercurian (*p*=0.493, n=24) distributions, rather than the lunar distribution (*p*=0.097, n=49). Previous work by Daniels (2018) has tentatively shown that Mercurian emplacement resembles Venusian emplacement with moderate *p* values reported, although after reexamination it appears that the interpreted correlation of Mercurian emplacement with Venusian emplacement is perhaps too generous. This places Mars and Mercury in a similar melt emplacement regime separate from the Moon and Venus. This potentially indicates there is a third melt emplacement regime, distinct from the lunar regime and the Venusian regime. This third regime could be a hybrid scheme for worlds with moderate surface gravity. These results suggest that surface gravity – not impactor velocity - is the dominant factor determining the style of melt emplacement. Venus, Mercury, and Mars all have gravities that are higher than that of the Moon, but impactor velocities that span the range from very large (Mercury) to very small (Mars). If impactor velocity is more important to the melt emplacement process, we would likely observe a difference in emplacement styles between Mars and Mercury, but that does not appear to be the case.

To understand why surface gravity plays such an important role in melt emplacement, we consider the amount of melt generated in an impact, and the depths of the resultant craters. We have put together Table 4 to help give a relative sense of how much melt on average is produced per crater on the different planetary bodies. A more detailed calculation has been provided in Appendix C, where each equation is identified and discussed. In Figure 20, we have plotted the percentage of melt volume per transient crater volume against the depth of our craters. Here, we assumed a number of conditions. First, we held the density of the projectile and target constant at 3 g/cm^3, based on the density of target material (presumed anorthosite) and the density of the projectile (presumed chondrite). Secondly, we assumed a projectile diameter of 1 km because estimates from size frequency distributions of the main asteroid belt suggest this diameter is the most common amongst currently observed asteroids (n~10^6, Bottke et al., (2005)). Our third assumption held the angle of impact for each body at the values found in Table 2 from Le Feuvre & Wieczorek, (2008). Our fourth assumption approximates the volume of a transient crater through the technique implemented by Pierazzo & Melosh, (2000). We advise caution when interpreting these numbers, as there are a number of factors that this back-of-the-envelope calculation does not account for, such as the porosity of the target.

We wish to draw attention to the right-most column of the Table 4, the percentage of melt per crater volume on each body. It would appear that for less massive worlds, like the Moon and Ceres, the lower surface gravity and hence deeper crater depths play a significant role in melt emplacement. Neish et al., (2017) suggests that in these situations, melt that manages to escape does so at the lowest rim height, which is also the lowest potential energy barrier. This implies that for lunar impacts with exterior melt deposits, the melt receives *only* enough momentum to cross the RCL threshold. This transfer of momentum likely takes place during the modification stage of crater formation, as the central uplift mobilizes the melt upward and outward (Osinski et al., 2011).

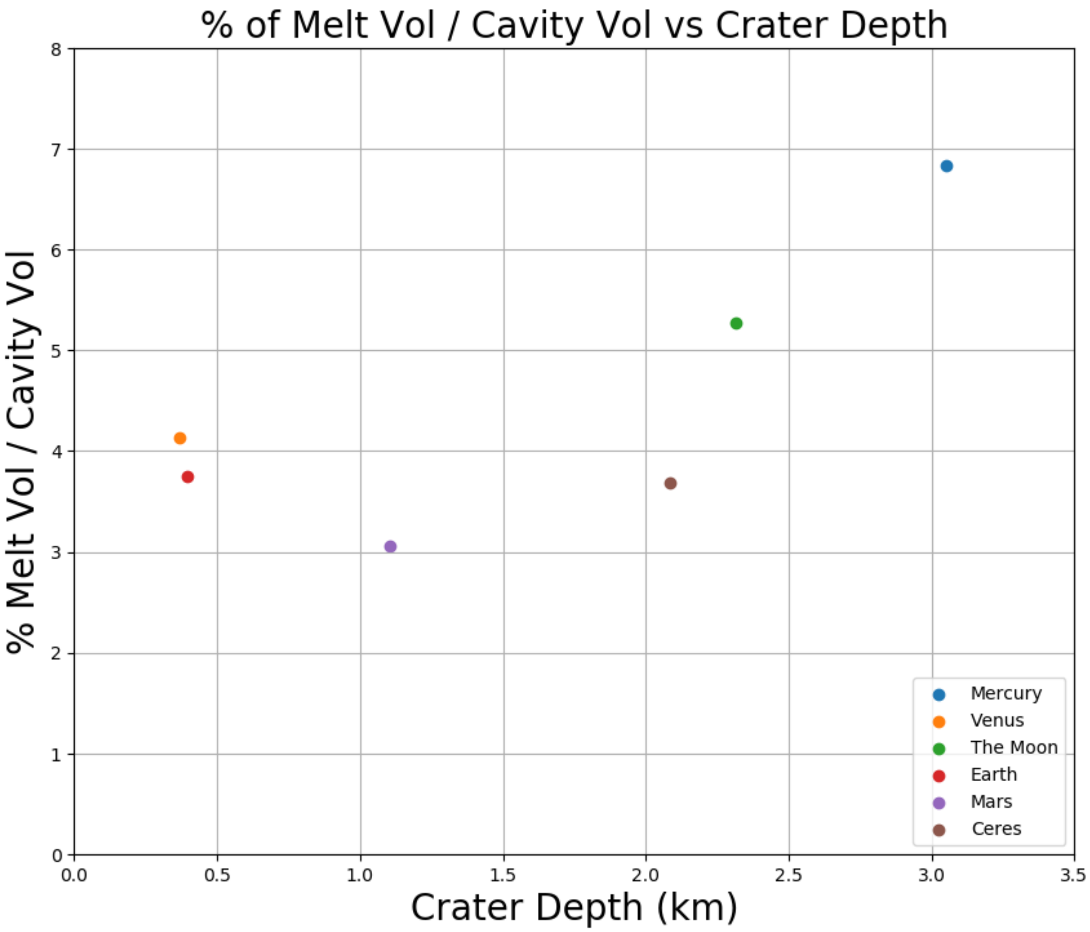

Figure 20 Percentage of melt volume to transient crater volume, plotted against estimated crater depth. Plot shows the results presented from Table 4. Melt percentage is given in terms of total crater volume for the terrestrial planets. Initial conditions and the assumptions that went into this calculation are referenced in the text. Further explanation for how the values in this table are calculated can be found in Appendix A.

Table 4. **Percent melt volume per transient crater cavity volume for rocky worlds. Melt volume was calculated from equations in Grieve & Cintala (1992) and cavity volume was calculated from equations in Pierazzo & Melosh (2000). A more detailed explanation for this table can be found in Appendix C.**

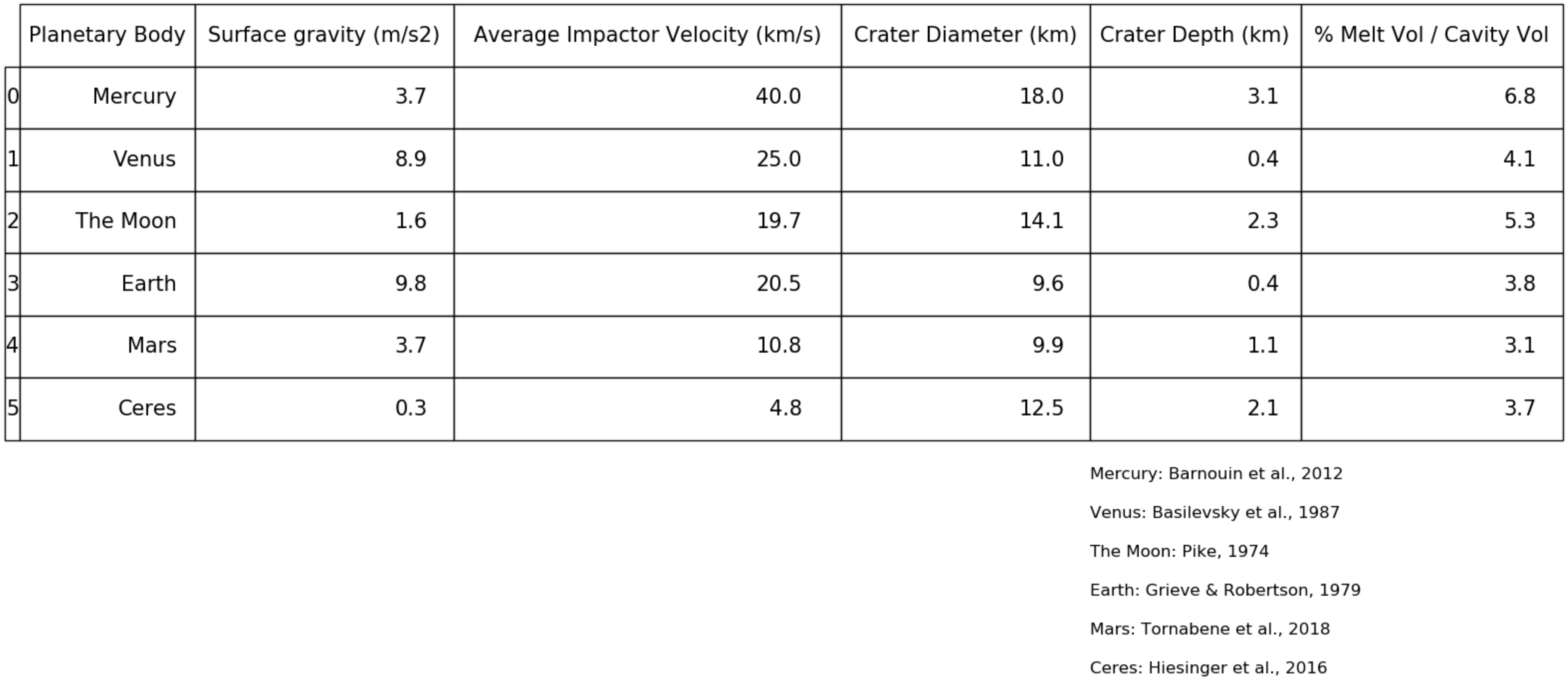

	Planetary Body	Surface gravity (m/s2)	Average Impactor Velocity (km/s)	Crater Diameter (km)	Crater Depth (km)	% Melt Vol / Cavity Vol
0	Mercury	3.7	40.0	18.0	3.1	6.8
1	Venus	8.9	25.0	11.0	0.4	4.1
2	The Moon	1.6	19.7	14.1	2.3	5.3
3	Earth	9.8	20.5	9.6	0.4	3.8
4	Mars	3.7	10.8	9.9	1.1	3.1
5	Ceres	0.3	4.8	12.5	2.1	3.7

Mercury: Barnouin et al., 2012

Venus: Basilevsky et al., 1987

The Moon: Pike, 1974

Earth: Grieve & Robertson, 1979

Mars: Tornabene et al., 2018

Ceres: Hiesinger et al., 2016

Mercury also has relatively deep craters, but the amount of melt generated is generally larger, an aspect that favors the mobilization of melt. This could mean that there is more opportunity for the melt to mobilize and be emplaced exterior to the crater rim. Even though melt generation is proportional to velocity squared, this calculation helps to characterize the amount of melt generated in relation to the size of the crater; the relationship is nonlinear. For example, Mercury's average impactor velocity is roughly four times that of Mars but the average percentage of melt per crater volume is only twice that of Mars. Furthermore, Mercury resembles the Moon in regard to melt volume per transient cavity volume, highlighting the overlap between the two effects of impactor velocity and surface gravity in melt production. The Moon is a less massive body with modest impactor velocities, while Mercury is a more massive body with higher impactor velocities. This calculation suggests that, similar to the Moon, the melt on Mercury may have more difficulty mobilizing past the crater rim than compared to Venus or Mars. However, mobilization of melt would be easier on Mercury than on the Moon since lunar craters produce less melt than Mercurian craters.

Venus is an end member amongst the bodies in the inner Solar System, with both high surface gravity and high impactor velocities. It also has a hot, thick atmosphere which may provide more favorable conditions for generating melt and keeping it molten for longer periods of time (Chadwick & Schaber, 1993; Grieve & Cintala, 1997). Neish et al., (2017) showed that there is no preference between the RCL and melt deposit distribution on Venus. Melt on Venus is likely emplaced during the excavation stage of impact crater formation, pushed outward by the downrange displacement of the flow field.

Work by Daniels (2018) investigated the melt emplacement mechanisms for Mercury. Melt emplacement on Mercury appears to lie between that of Venus and the Moon. It has moderate surface gravity and high impactor velocities, in contrast to Mars, which has similar surface gravity but low impactor velocities. Mars and Mercury offer an intriguing point of comparison, since they have the same gravity but different average impactor velocities. From our calculation from Table 4, we can make interpretations about the mobilization of melt on Mars and Mercury. Mars has less melt volume per crater volume than Mercury, but craters on Mars are shallower than those on Mercury. The R ratios for Mercury, Venus, and Mars all show little correlation between the degree of separation from the melt to the RCL. As a reminder, the R values represent the range of heights, from the rim crest low to the rim crest high, normalized to depth of the crater. So, a low R value can represent either a small range of crater rim heights, or it can represent large depths. A large R value could indicate the inverse; either a wide range of crater rim heights or a small crater depth. An R value of about 1 suggests that rim height variation is comparable to the depth of the crater. Along these lines, the R ratios presented by Neish et al. (2017) (Figure 7 in their study) and Daniels (2018) (Figure 18 in their work) indicate that 1) the craters on Mercury are generally deep compared to their rim variation, where R values generally range in from about 0.1-1, and/or 2) the rim variation for Mercury is relatively limited. For comparison, lunar R values reported by Neish et al. (2017) tend to be somewhat smaller than for those reported for Venus. This effect may be largely due to the size of the two worlds, where craters tend to be shallower on Venus and so therefore the R values tend to be larger.

We can interpret Martian R values a couple of ways: 1) the lack of correlation between the RCL and the distribution of melt suggests that the rebound experienced by complex crater floors, at least on Mars, is not sufficient enough for the melt to mobilize across the potential energy barrier of the RCL, or 2) more likely, the lack of correlation means there is not enough melt left over after being ejected in the excavation stage to mobilize during the modification stage. In other words, impact melt may have two main opportunities to escape the crater rim: first during the excavation stage and then during central uplift within the modification stage. Given a total amount of generated impact melt, there may only be a fraction of impact melt that is capable of mobilizing past the crater rim. So, if that fraction of melt mobilizes during the excavation stage, there may not be enough left over to mobilize during the modification stage. For lunar conditions, where the craters are deep and the melt volume is low, there may not be enough energy/momentum imparted to move the impact melt during the excavation stage, so instead the fraction of melt within the crater is retained until the modification stage, when it can escape past the rim with the assistance of a rebound mechanism.

This body of work, along with previous research on Mercury, Venus, and the Moon, support the hypothesis originally put forth by Hawke & Head, (1977). They hypothesized that pre-impact topography and the angle of incidence of the impactor both play an important role in the distribution of exterior melt deposits. Osinski et al., (2011) and Neish et al., (2017) were the first to compare emplacement mechanisms for different worlds, and showed that impactor velocity and gravity are the more pertinent factors in melt emplacement. Here, we refine this idea further, showing that surface gravity plays a more dominant role in melt emplacement than impactor velocity. For bodies with higher surface gravity, melt is primarily mobilized exterior to the crater during the excavation stage of impact crater formation. For bodies with smaller surface gravity, melt is only able to overcome the potential barrier of the rim during central uplift in the modification stage.

To summarize, we find that the melt emplacement on Mars most closely resembles that of Mercury, rather than the Moon or Venus (see Figure 21). It would appear that an intermediate regime for moderate surface gravity worlds is needed to describe the melt emplacement process for Mars and Mercury. Thus, we propose a third melt emplacement regime, in addition to impactor-direction controlled emplacement and pre-impact topography controlled emplacement, to describe intermediate surface gravity worlds, like Mars and Mercury. It would seem that the grouping of Mars and Mercury separate from the Moon and Venus indicates that a planetary body’s surface gravity plays a more important role in the mobilization of melt than impact velocity.

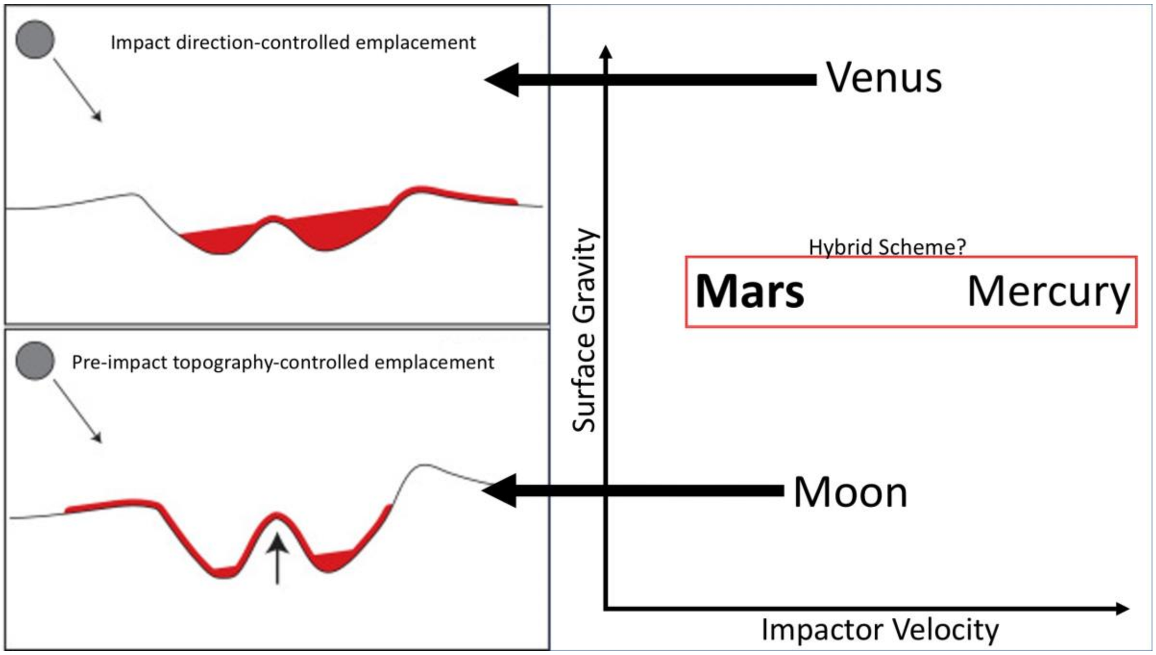

Figure 21. Modified from Daniels, (2018) and Neish et al., (2017). This study tentatively finds the Martian melt emplacement regime to resemble the Mercurian regime more closely than the lunar or Venusian regimes.

4.2 Limitations of CTX Data

We seek to address the limitations of our study and where future research can improve upon this work. While there is an abundance of high-resolution data for Mars compared to other bodies in the Solar System, they do come with a number of limitations. HiRISE images have provided unprecedented, sub-meter scale detail of the Martian surface; however, such high resolution comes at the expense of surface coverage (as of 2016, after ten years of operation, HiRISE has imaged less than three per cent of the Martian surface, https://uanews.arizona.edu/story/hirise-45000-mars-orbits-and-counting).The recent production of a CTX global mosaic by Dickson et al., (2018) may provide a means to quickly identify larger scale melt ponds. This comes with a caveat that the size of the pitted materials scale with the size of the deposit (Tornabene et al., 2012). In other words, only the largest melt ponds will have pitted materials resolvable by CTX and the global mosaic will be insensitive to pitted materials less than about 24 m in diameter (some of the smallest pitted materials have been observed with diameters down to about 10 m (Tornabene et al., 2012)).

HiRISE image coverage was also a source of bias in choosing the craters for our study. The crater-related pitted material database by Tornabene et al., (2012), which was used for our candidate crater selection, was further refined based on the amount of HiRISE coverage present around each crater. This selection process naturally favored smaller craters more easily covered by HiRISE, although CTX is sufficient for craters larger than about 30 km. Thus, there are a number of craters within our catalogue that reside within the transitional range between simple and complex craters, although the features of our craters more closely resemble complex craters than simple craters. While we can make comparisons to the complex craters studied for Mercury, Venus and the Moon in the style of Daniels, (2018), Chadwick & Schaber, (1993), and Neish et al., (2017), it should be noted that the craters in the transitional range tend to be deeper than their purely complex counter parts. Generally, simple craters have d/D ratios around 1:5 and complex craters are around 1:10 (Melosh, 1989; Pike, 1980), where transitional craters fall between these two values. If melt emplacement exterior to a crater is dependent on crater depth, as may be pertinent for lunar-like melt emplacement, then this bias needs to be accounted for.

Another limitation we experienced in our study was the resolution and quality of the DTM data. We initially looked to HiRISE DTMs and corresponding slope-derived data to show the equipotential melt pond surfaces, as seen in Tornabene et al., (2012). We found that even when the slope-derived data was masked out for values greater than 3 degrees, it was noisy and difficult to determine where the edges of the ponds lay. When combined with the visual data, however, a determination could generally be made. We also caution that a topographically enclosed equipotential surface by itself does not constitute a melt pond necessarily, but when looked at jointly with visual images, the determination can become somewhat clearer. CTX DTMs were too noisy to determine if melt was present and were avoided as a diagnostic tool. Many times in CTX DTM generation, crater rims cast deep shadows, causing the pixel registration to fail at the shadowed regions. The DTMs were also not tied to MOLA data, and so are only representative of crater elevation in a relative sense.

4.3 Future Work

In this section, we reflect upon future directions for this work.

4.3.1 Larger Sample Size for Martian Craters

If follow up work on this topic for Mars were to take place, a larger, more representative sample population would be desired. Craters should be sourced from the same crater database used in this work (Tornabene et al., 2012), or at the very least should show signs of the crater-related pitted materials, as they constitute a morphologically characteristic feature consistent with melt deposits on Mars. More emphasis should be placed on craters that are not severely influenced by extreme slopes and topography. This body of work included 3 craters with extreme terrain (e.g. craters in the side of canyon walls have all but predetermined melt emplacement directions), craters with various processes affecting their appearance (e.g. an extra dusty region or in a region of periglacial process), and craters that that are on the smaller side of the complex morphology (e.g. CTX could have been used more often for larger craters to try to identify melt ponds instead of primarily relying on HiRISE). In addition to these factors, we also suggest that a higher quantity of complex craters be studied. The sample size in the work is rather limited in scope and so having a higher quantity of craters could help further contextualize the results found here.

4.3.2 Impactor Direction

Previous work studied melt emplacement directions in comparison to the RCL, but also looked at the correlation of impactor direction to the direction of melt emplacement (Chadwick and Schaber, 1993; Daniels, 2018; Neish et al., 2017). Identifying impactor direction has been a particular challenge for Mars, and was not part of this work, in part because of the dynamic geologic and atmospheric processes that can obscure the distal parts of the ejecta, namely crater rays. On Mars, rayed craters have been observed (Tornabene et al., 2006), but are not as common as on the Moon and Mercury (Morota and Furumoto, 2003; Neish et al., 2013). The asymmetric ejecta blanket and crater rays that are associated with oblique impacts are often obscured by dust from the atmosphere on Mars. Since the asymmetric ejecta blanket is most often used to determine impactor direction and is often lacking on Mars, another method may be needed to identify impactor direction. As mentioned in the section above, a more “representative” crater sample population may be needed in order to make any observations about impactor direction. If at a later date it is shown that exterior melt ponds to Martian craters exhibit bilateral symmetry, then that may be a useful key to identify impactor direction, or narrow down the impactor direction to two choices. For example, if there has been an oblique impact and there are roughly similar proportions of melt to the east and west of the crater, this likely indicates that impactor direction either from north to south or vice versa. If impactor direction can be determined with some degree of certainty, follow up work examining the correlation to melt emplacement would be pertinent.

4.3.3 Ceres

To provide another data point in the Solar System, Ceres would make a great candidate for studying melt emplacement. It is a body with both low surface gravity and low impactor velocities (O’Brien and Sykes, 2011). If melt emplacement is indeed dependent on surface gravity, we might expect melt emplacement on Ceres to resemble that of the Moon. And based on our melt-volume-per-transient-crater-volume calculations in Appendix C, we might expect that melt may be harder to mobilize past the crater rim. For an average impact, Cerean craters are relatively deep. Compound this with low impact velocities (i.e., relatively less melt is generated) and it would seem that melt mobilization on Ceres would be rather limited. In other words, there may be in general a higher potential energy barrier for the melt to overcome in order to be emplaced exterior to the crater. Some of the prominent craters with exterior melt ponds on Ceres, such as Dantu or Ikapati, may have been influenced by their pre-impact topography guiding the melt out of the crater (Hibbard et al., 2018).

Chapter 5

5 Conclusions

In this work, we present results for exterior impact melt emplacement around Martian craters. We then compare our results to melt emplacement processes on Venus, the Moon, and Mercury. We also comment on the roles of surface gravity and impactor velocity for melt emplacement on Mars and on other rocky planetary bodies.

We have utilized the Anderson Darling goodness-of-fit statistic for the distribution of R values versus the degree of separation of melt from the RCL for Mars against the distributions for Mercury, Venus, and the Moon. We have found p values for the comparison against the Venusian distribution to be p=0.009, against the lunar distribution to be p=0.097, and against the Mercurian distribution to be p=0.493. These p values suggest that for Mars, the melt emplacement regime more closely resembles the Mercurian regime, rather than the lunar or Venusian regimes. This now places Mars and Mercury into one grouping, distinct from both lunar and Venusian-style emplacement. We propose a third regime to describe melt emplacement for moderate surface gravity worlds, where surface gravity plays the larger role in emplacement, compared to impactor velocity.

We can make a direct comparison of the effects of impact velocity on melt emplacement because Mercury and Mars have similar gravity. Mercury exhibits high impact velocities while Mars has relatively low impact velocities, as shown in Figure 10. Even though Mercury and Mars have amongst the highest and lowest average impact velocities of terrestrial bodies in the Solar System, a large difference of melt emplacement regimes is not observed. The p values for Mars against the Mercurian distribution suggest emplacement is somewhat related for the two bodies, possibly coming from similar sample distributions (e.g. similar emplacement styles). If this work holds true, impact velocity likely has less of an influence on higher gravity worlds for the melt emplacement process than surface gravity. In other words, it seems that for sufficiently massive worlds, surface gravity may play the more important role in melt emplacement than impactor velocity.

For less massive worlds, like the Moon, the effects of surface gravity and impact velocity may be comparable, or impact velocity may play the more dominant role in determining how impact melt is emplaced. Additionally, it seems that crater depth (which is related primarily to surface gravity) could play an important role in melt emplacement; the shallower the crater, the more opportunity for the melt to mobilize. For low-gravity worlds, it would seem that craters will be deeper, constraining melt emplacement opportunities.

The majority of melt mobilization for Venus occurs during the excavation stage of a cratering event, whereas the majority of melt mobilization takes place during the modification stage for the Moon. For Mars and Mercury, the timing for melt mobilization is not fully clear; emplacement could feasibly take place at the excavation and/or the modification stage. As a high gravity terrestrial world, Venus has generally shallower craters, and has larger volumes of melt generated. In contrast, the Moon has deeper craters with less volumes of melt generated. Mars is intermediary with smaller volumes of melt generated and shallower craters, in comparison to the Moon, but less melt generated and deeper craters than Venus, in general. The momentum needed for the melt to exceed the crater rim could come at 1) during the excavation stage, 2) during the modification stage, or 3) a combination of 1) and 2).

In this work, we emphasize the melt emplacement process for complex craters. While there are two craters in our catalogue that do not meet the criteria for being a complex crater, the remaining twelve are complex. This sampling of craters, as previously discussed, is biased towards smaller complex craters, due to the limitations of HiRISE coverage of larger complex craters. It is possible these smaller complex craters contain smaller volumes of melt available for mobilization than their larger counterparts, although this may not be a limiting factor. If the amount of melt available for mobilization is important to melt emplacement, then this bias will need to be accounted for. We emphasize melt emplacement for complex craters because previous studies, such as for Chadwick & Schaber, (1993), have been limited by the rarity of simple craters on Venus. Additionally, simple craters and corresponding melt on Mercury can be difficult to study because of the limited resolution and coverage of data products from the

MESSENGER mission. Follow up research for Mars and Mercury could investigate the melt emplacement regimes for simple craters. Previous work, by Neish et al., (2014), studied both simple and complex craters on the Moon and found that while roughly 80% of lunar complex craters coincided with the RCL, only about 60% of simple craters with exterior melt distributions also aligned, or mostly aligned, with the RCL. The difference may be due to the lack of central uplifting in simple crater formation.

For future study, work on Ceres or Vesta can elucidate melt emplacement regimes for less massive bodies. Average impact velocities on Ceres are around 4.8 km/s (O'Brien and Sykes, 2011) and a quick calculation in the same manner as Table 4 shows that the percentage of melt volume for a transient crater on Ceres may be closer to Venus and Mars, rather than the Moon and Mercury. Because of its small size, Ceres has relatively deep craters. With smaller volumes of melt generated per impact, compounded by relatively deep craters, this might suggest that melt emplacement on Ceres may resemble the style of emplacement seen on the Moon. If Cerean melt emplacement resembles lunar emplacement, it would further support the idea that melt emplacement regimes are more dependent on surface gravity rather than impact velocity.

References

Abramov, O., Wong, S.M., Kring, D.A., 2012. Differential melt scaling for oblique impacts on terrestrial planets. Icarus 218, 906–916. https://doi.org/10.1016/j.icarus.2011.12.022

Acuña, M.H., Connerney, J.E.P., Ness, N.F., Lin, R.P., Mitchell, D., Carlson, C.W., McFadden, J., Anderson, K.A., Rème, H., Mazelle, C., Vignes, D., Wasilewski, P., Cloutier, P., 1999. Global distribution of crustal magnetization discovered by the Mars Global Surveyor MAG/ER experiment. Science (80-.). 284, 790–793. https://doi.org/10.1126/science.284.5415.790

Acuña, M.H., Connerney, J.E.P., Wasilewski, P., Lin, R.P., Mitchell, D., Anderson, K.A., Carlson, C.W., McFadden, J., Reme, H.R., Mazelle, C., Vignes, D., Bauer, S.J., Cloutier, P., Ness, N.F., 2001. Magnetic field of Mars: Summary of results from the aerobraking and mapping orbits. J. Geophys. Res. Planets 106, 23403–23417.

Ahrens, T.J., O’Keefe, J.D., 1972. Shock melting and vaporization of lunar rocks and minerals, Conference on Lunar Geophysics. https://doi.org/10.1007/BF00562927

Albee, A.L., Palluconi, F.D., Arvidson, R.E., 1998. Mars Global Surveyor Mission : Overview and Status The Structure of the Upper Atmosphere of Mars : In Situ Accelerometer Measurements from Mars Global Surveyor. Science (80-.). 279, 1671–1672.

Baker, D.M.H., 2016. Updated Catalogs of peak-ring basins and protobasins on Mars. Lunar Planet. Sci. Conf. XLVII.

Bandfield, J.L., 2002. Global mineral distributions on Mars. J. Geophys. Res. E Planets 107. https://doi.org/10.1029/2001je001510

Bandfield, J.L., Hamilton, V.E., Christensen, P.R., 2000. A global view of martian surface compositions from MGS-TES. Science (80-.). 287, 1626–1630. https://doi.org/10.1126/science.287.5458.1626

Barlow, N.G., 2008. Mars: An Introduction to Its Interior, Surface and Atmosphere. Cambridge University Press.

Barlow, N.G., 2005. A review of Martian impact crater ejecta structures and their implications for target properties. Spec. Pap. Geol. Soc. Am. 384, 433–442. https://doi.org/10.1130/0-8137-2384-1.433

Barlow, N.G., 1988. Crater size-frequency distributions and a revised Martian relative chronology. Icarus 75, 285–305. https://doi.org/10.1016/0019-1035(88)90006-1

Barlow, N.G., Boyce, J.M., Costard, F.M., Craddock, R.A., Garvin, J.B., Sakimoto, S.E.H., Kuzmin, R.O., Roddy, D.J., Soderblom, L.A., 2000. Standardizing the nomenclature of Martian impact crater ejecta morphologies. J. Geophys. Res. 105, 26733–26738. https://doi.org/10.1029/2000JE001258

Barlow, N.G., Bradley, T.L., 1990. Martian impact craters: Correlations of ejecta and interior morphologies with diameter, latitude, and terrain. Icarus 87, 156–179. https://doi.org/10.1016/0019-1035(90)90026-6

Barnouin-Jha, O.S., Schultz, P.H., Lever, J.H., 1999a. Investigating the interactions between an atmosphere and an ejecta curtain 1. Wind tunnel tests. J. Geophys. Res. 104, 27105–27115.

Barnouin-Jha, O.S., Schultz, P.H., Lever, J.H., 1999b. Investigating the interactions between an atmosphere and an ejecta curtain 2. Numerical experiments. J. Geophys. Res. 104, 27117–27131.

Barnouin, O.S., Zuber, M.T., Smith, D.E., Neumann, G.A., Herrick, R.R., Chappelow, J.E., Murchie, S.L., Prockter, L.M., 2012. The morphology of craters on Mercury: Results from MESSENGER flybys. Icarus 219, 414–427. https://doi.org/10.1016/j.icarus.2012.02.029

Basilevsky, A.T., Ivanov, B.A., Burba, G.A., Chernaya, I.M., Kryuchkov, V.P., Nikolaeva, O. V., Campbell, D.B., Ronca, L.B., 1987. Impact craters of Venus: A continuation of the analysis of data from the Venera 15 and 16 spacecraft. J.

Geophys. Res. 92, 12869. https://doi.org/10.1029/jb092ib12p12869

Bottke, W.F., Durda, D.D., Nesvorný, D., Jedicke, R., Morbidelli, A., Vokrouhlický, D., Levison, H., 2005. The fossilized size distribution of the main asteroid belt. Icarus 175, 111–140. https://doi.org/10.1016/j.icarus.2004.10.026

Boyce, J.M., Garbeil, H., 2007. Geometric relationships of pristine Martian complex impact craters, and their implications to Mars geologic history. Geophys. Res. Lett. 34, 1–5. https://doi.org/10.1029/2007GL029731

Boyce, J.M., Mouginis-Mark, P., Garbeil, H., Tornabene, L.L., 2006. Deep impact craters in the Isidis and southwestern Utopia Planitia regions of Mars: High target material strength as a possible cause. Geophys. Res. Lett. 33, 2–5. https://doi.org/10.1029/2005GL024462

Boyce, J.M., Wilson, L., Mouginis-Mark, P.J., Hamilton, C.W., Tornabene, L.L., 2012. Origin of small pits in martian impact craters. Icarus 221, 262–275. https://doi.org/10.1016/j.icarus.2012.07.027

Bridges, N.T., Geissler, P.E., McEwen, A.S., Thomson, B.J., Chuang, F.C., Herkenhoff, K.E., Keszthelyi, L.P., Martínez-Alonso, S., 2007. Windy Mars: A dynamic planet as seen by the HiRISE camera. Geophys. Res. Lett. 34, 1–7. https://doi.org/10.1029/2007GL031445

Carr, M.H., 2006. The Surface of Mars. Cambridge University Press.

Carr, M.H., Crumpler, L.S., Cutts, J.A., Greeley, R., Guest, J.E., Masursky, H., 1977. Martian impact craters and emplacement of ejecta by surface flow. J. Geophys. Res. 82, 4055–4065. https://doi.org/10.1029/js082i028p04055

Carr, M.H., Head, J.W., 2010. Geologic history of Mars. Earth Planet. Sci. Lett. 294, 185–203. https://doi.org/10.1016/j.epsl.2009.06.042

Chadwick, D.J., Schaber, G.G., 1993. Impact crater outflows on Venus: morphology and emplacement mechanisms. J. Geophys. Res. 98. https://doi.org/10.1029/93je02605

Chojnacki, M., Burr, D.M., Moersch, J.E., Michaels, T.I., 2011. Orbital observations of contemporary dune activity in Endeavor crater, Meridiani Planum, Mars. J. Geophys. Res. E Planets 116, 1–20. https://doi.org/10.1029/2010JE003675

Cintala, M.J., 1992. Impact-induced thermal effects in the lunar and mercurian regoliths. J. Geophys. Res. 97, 947–973. https://doi.org/10.1029/91JE02207

Cintala, M.J., Grieve, R.A.F., 1998. Scaling impact melting and crater dimensions:Implications for the lunar cratering record. Meteorit. Planet. Sci. 33, 889–912. https://doi.org/10.1111/j.1945-5100.1998.tb01695.x

Daniels, J., 2018. Impact Melt Emplacement on Mercury. Electron. Thesis Diss. Repos. 5657.

DeMeo, F.E., Carry, B., 2013. The Taxonomic Distribution of Asteroids from Multi-filter All-sky Photometric Surveys. Icarus 226, 723–741. https://doi.org/10.1016/j.icarus.2013.06.027

Dence, M.R., 1968. Shock zoning at Canadian craters: petrography and structural implications, in: Shock Metamorphism of Natural Materials. pp. 169–184.

Dence, M.R., 1965. the Extraterrestrial Origin of Canadian Craters. Ann. N. Y. Acad. Sci. 123, 941–969. https://doi.org/10.1111/j.1749-6632.1965.tb20411.x

Denevi, B.W., Blewett, D.T., Buczkowski, D.L., Capaccioni, F., Al, E., 2012. Pitted Terrain on Vesta and Implications for the Presence of Volatiles. Science (80-.). 338, 246–250.

Dickson, J.L., Kerber, L.A., Ehlmann, B.L., 2018. A Global, Blended CTX Mosaic of Mars with Vectorized Seam Mapping: A New Mosaicking Pipeline Using Principles of Non-Destructive Image Editing. 49th Lunar Planet. Sci. Conf.

Edgett, K.S., Malin, M.C., 2000. New views of Mars eolian activity, materials, and surface properties: Three vignettes from the Mars Global Surveyor Mars Orbiter Camera. J. Geophys. Res. E Planets 105, 1623–1650.

https://doi.org/10.1029/1999JE001152

Feldman, W.C., Prettyman, T.H., Maurice, S., Plaut, J.J., Bish, D.L., Vaniman, D.T., Mellon, M.T., Metzger, A.E., Squyres, S.W., Karunatillake, S., Boynton, W. V., Elphic, R.C., Funsten, H.O., Lawrence, D.J., Tokar, R.L., 2004. Global distribution of near-surface hydrogen on Mars. J. Geophys. Res. E Planets 109, 1–13. https://doi.org/10.1029/2003JE002160

French, B.M., 1998. Impact Melts, in: Traces of Catastrophe: A Handbook of Shock-Metamorphic Effects in Terrestrial Meteorite Impact Structures. Lunar and Planetary Institute, pp. 79–96.

Gault, D.E., Oberbeck, V.R., Quaide, W.L., 1968. Impact cratering mechanics and structures, in: French, B.M., Short, N.M. (Eds.), Shock Metamorphism of Natural Materials. pp. 87–99.

Gault, D.E., Wedekind, J.A., 1978. Experimental studies of oblique impacts. Proc. Lunar Planet. Sci. Conf. 9th 3483–3875.

Grieve, R.A.F., Cintala, M.J., 1997. Planetary differences in impact melting. Adv. Sp. Res. 20, 1551–1560. https://doi.org/10.1016/S0273-1177(97)00877-6

Grieve, R.A.F., Cintala, M.J., 1995. Impact Melting on Venus: Some Considerations for the Nature of the Cratering Record. Icarus 114, 68–79.

Grieve, R.A.F., Cintala, M.J., 1992. An analysis of differential impact melt-crater scaling and implications for the terrestrial impact record. Meteorit. 27 526–538.

Grieve, R.A.F., Cintala, M.J., 1981. A method for estimating the intial impact conditions of terrestrial cratering events, exemplified by its application to Brent crater, Ontario. Lunar Planet. Sci. Conf. 12th 1607–1621.

Grieve, R.A.F., Dence, M.R., Robertson, P.B., 1977. Cratering processes: As interpreted from the occurance of impact melts. Impact Explos. Cratering 791–814.

Grieve, R.A.F., Robertson, P.B., 1979. The Terrestrial Cratering Record. Icarus 212–229.

Hartmann, W.K., Neukum, G., Zentrum, D., Berlin, D.-, 2001. CRATERING CHRONOLOGY AND THE EVOLUTION OF MARS 1 . Background : Cratering Studies and the Relation to Martian Rocks Through the process of impact cratering , Nature randomly stamps circular bowls of known shape on planetary surfaces . This fact offers us. Space Sci. Rev. 96, 165–194.

Hawke, B.R., Head, J.W., 1977. Impact melt on lunar crater rims. Impact Explos. Cratering 815–841.

Herrick, R.R., Hessen, K.K., 2006. The planforms of low-angle impact craters in the northern hemisphere of Mars. Meteorit. Planet. Sci. 41, 1483–1495. https://doi.org/10.1111/j.1945-5100.2006.tb00431.x

Herrick, R.R., Sharpton, V.L., Malin, M.C., Lyons, S.N., Feely, K., 1997. Morphology and Morphometry of Impact Craters, in: Bougher, S.W., Hunten, D.M., Philips., R.J. (Eds.), Venus II : Geology, Geophysics, Atmosphere, and Solar Wind Environment. University of Arizona Press, p. 1015.

Hibbard, S.M., Osinski, G.R., Tornabene, L.L., 2018. CRATER-RELATED SURFACE MORPHOLOGIES OF THE IKAPATI CRATER, CERES. Lunar Planet. Sci. Conf. 49th 2083.

Hiesinger, H., Marchi, S., Schmedemann, N., Schenk, P., Pasckert, J.H., Neesemann, A., O’Brien, D.P., Kneissl, T., Ermakov, A.I., Fu, R.R., Bland, M.T., Nathues, A., Platz, T., Williams, D.A., Jaumann, R., Castillo-Rogez, J.C., Ruesch, O., Schmidt, B., Park, R.S., Preusker, F., Buczkowski, D.L., Russell, C.T., Raymond, C.A., 2016. Cratering on ceres: Implications for its crust and evolution. Science (80-.). 353. https://doi.org/10.1126/science.aaf4759

Howard, K.., Wilshire, H.G., 1975. Flows of Impact Melt at Lunar Craters. Abstr. Lunar Planet. Sci. Conf. 3, 287–251.

Ivanov, B.A., 2001. Mars/Moon cratering rate ratio estimates. Space Sci. Rev. 96, 87–

104. https://doi.org/10.1023/A:1011941121102

Ivanov, B.A., Basilevsky, A.T., Kryuchkov, V.P., Chernaya, I.M., 1986. Impact Craters of Venus: Analysis of Venera 15 and 16 Data. J. Geophys. Res. 91, 413–430.

Johnson, C.L., Mittelholz, A., Langlais, B., Russell, C.T., Ansan, V., Banfield, D., Chi, P., Fillingim, M., Forget, F., Haviland, H.F., Golombek, M., Joy, S., Lognonné, P., Liu, X., Michaut, C., Pan, L., Quantin-Nataf, C., Spiga, A., Stanley, S., Thorne, S., Wieczorek, M., Yu, Y., Smrekar, S.E., Banerdt, W.B., 2020. Crustal and time-varying magnetic fields at the InSight landing site on Mars. Nat. Geosci. 13. https://doi.org/10.1038/s41561-020-0537-x

Kieffer, S.W., Simonds, C.H., 1980. The role of volatiles and lithology in the impact cratering process. Rev. Geophys. 18, 143–181. https://doi.org/10.1029/RG018i001p00143

Korycansky, D.G., Zahnle, K.J., 2005. Modeling crater populations on Venus and Titan. Planet. Space Sci. 53, 695–710. https://doi.org/10.1016/j.pss.2005.03.002

Krohn, K., Jaumann, R., Stephan, K., Otto, K.A., Schmedemann, N., Wagner, R.J., Matz, K.D., Tosi, F., Zambon, F., von der Gathen, I., Schulzeck, F., Schröder, S.E., Buczkowski, D.L., Hiesinger, H., McSween, H.Y., Pieters, C.M., Preusker, F., Roatsch, T., Raymond, C.A., Russell, C.T., Williams, D.A., 2016. Cryogenic flow features on Ceres: Implications for crater-related cryovolcanism. Geophys. Res. Lett. 43, 11,994-12,003. https://doi.org/10.1002/2016GL070370

Le Feuvre, M., Wieczorek, M.A., 2011. Nonuniform cratering of the Moon and a revised crater chronology of the inner Solar System. Icarus 214, 1–20. https://doi.org/10.1016/j.icarus.2011.03.010

Le Feuvre, M., Wieczorek, M.A., 2008. Nonuniform cratering of the terrestrial planets. Icarus 197, 291–306. https://doi.org/10.1016/j.icarus.2008.04.011

Leight, C., Ostrach, L.R., 2018. Characterizing Impact Melt on Mercury. Lunar Planet. Sci. Conf. 49th.

Leighton, R.B., Murray, B.C., 1966. Behavior of Carbon Dioxide and Other Volatiles on Mars. Science (80-.). 153, 137–144.

Lillis, R.J., Robbins, S., Manga, M., Halekas, J.S., Frey, H. V., 2013. Time history of the Martian dynamo from crater magnetic field analysis. J. Geophys. Res. E Planets 118, 1488–1511. https://doi.org/10.1002/jgre.20105

Malin, M.C., Bell, J.F., Cantor, B.A., Caplinger, M.A., Calvin, W.M., Clancy, R.T., Edgett, K.S., Edwards, L., Haberle, R.M., James, P.B., Lee, S.W., Ravine, M.A., Thomas, P.C., Wolff, M.J., 2007. Context Camera Investigation on board the Mars Reconnaissance Orbiter. J. Geophys. Res. E Planets 112, 1–25. https://doi.org/10.1029/2006JE002808

Marchi, S., Mottola, S., Cremonese, G., Massironi, M., Martellato, E., 2009. A new chronology for the Moon and Mercury. Astron. J. 137, 4936–4948. https://doi.org/10.1088/0004-6256/137/6/4936

Marvin, U.B., Kring, D.A., 1992. Authentication controversies and impactite petrography of the New Quebex Crater. Meteorit. 27 58–595.

McCauley, J.F., 1973. Mariner 9 evidence for wind erosion in the equatorial and mid-latitude regions of Mars. J. Geophys. Res. 78, 4123–4137. https://doi.org/10.1029/jb078i020p04123

McEwen, A.S., Eliason, E.M., Bergstrom, J.W., Bridges, N.T., Hansen, C.J., Delamere, W.A., Grant, J.A., Gulick, V.C., Herkenhoff, K.E., Keszthelyi, L., kirk, R.L., Mellon, M.T., Squyres, S.W., Thomas, N., Weitz, C.M., 2007. Mars reconnaissance orbiter's high resolution imaging science experiment (HiRISE). J. Geophys. Res. E Planets 112, 1–40. https://doi.org/10.1029/2005JE002605

McEwen, A.S., Preblich, B.S., Turtle, E.P., Artemieva, N.A., Golombek, M.P., Hurst, M., Kirk, R.L., Burr, D.M., Christensen, P.R., 2005. The rayed crater Zunil and interpretations of small impact craters on Mars. Icarus 176, 351–381. https://doi.org/10.1016/j.icarus.2005.02.009

Melosh, H.J., 1989. Planetary Surface Processes. Cambridge University Publishing. https://doi.org/https://doi.org/10.1017/CBO9780511977848

Melosh, H.J., Ivanov, B.A., 1999. Impact Crater Collapse. Annu. Rev. Earth Planet. Sci. 27, 385–415. https://doi.org/10.1146/annurev.earth.27.1.385

Morota, T., Furumoto, M., 2003. Asymmetrical distribution of rayed craters on the Moon. Earth Planet. Sci. Lett. 206, 315–323. https://doi.org/10.1016/S0012-821X(02)01111-1

Neish, C.D., Blewett, D.T., Harmon, J.K., Coman, E.I., Cahill, J.T.S., Ernst, C.M., 2013. A comparison of rayed craters on the moon and mercury. J. Geophys. Res. E Planets 118, 2247–2261. https://doi.org/10.1002/jgre.20166

Neish, C.D., Herrick, R.R., Zanetti, M., Smith, D., 2017. The role of pre-impact topography in impact melt emplacement on terrestrial planets. Icarus 297, 240–251. https://doi.org/10.1016/j.icarus.2017.07.004

Neish, C.D., Madden, J., Carter, L.M., Hawke, B.R., Giguere, T., Bray, V.J., Osinski, G.R., Cahill, J.T.S., 2014. Global distribution of lunar impact melt flows. Icarus 239, 105–117. https://doi.org/10.1016/j.icarus.2014.05.049

Neish, C.D., Molaro, J.L., Lora, J.M., Howard, A.D., Kirk, R.L., Schenk, P., Bray, V.J., Lorenz, R.D., 2016. Fluvial erosion as a mechanism for crater modification on Titan. Icarus 270, 114–129. https://doi.org/10.1016/j.icarus.2015.07.022

Neukum, G., Ivanov, B.A., Hartmann, W.K., 2001. Cratering records in the inner solar system in relation to the lunar reference system. Space Sci. Rev. 96, 55–86. https://doi.org/10.1023/A:1011989004263

Neumann, G.A., Zuber, M.T., Wieczorek, M.A., McGovern, P.J., Lemoine, F.G., Smith, D.E., 2004. Crustal structure of Mars from gravity and topography. J. Geophys. Res. E Planets 109, 1–18. https://doi.org/10.1029/2004JE002262

O’Brien, D.P., Sykes, M. V., 2011. The origin and evolution of the asteroid belt-implications for Vesta and Ceres. Space Sci. Rev. 163, 41–61. https://doi.org/10.1007/s11214-011-9808-6

Oberbeck, V.R., 1975. The role of ballistic erosion and sedimentation in lunar stratigraphy. Rev. Geophys. 13, 337–362. https://doi.org/10.1029/RG013i002p00337

Osinski, G.R., Grieve, R.A.F., Bleacher, J.E., Neish, C.D., Pilles, E.A., Tornabene, L.L., 2018. Igneous rocks formed by hypervelocity impact. J. Volcanol. Geotherm. Res. 353, 25–54. https://doi.org/10.1016/j.jvolgeores.2018.01.015

Osinski, G.R., Pierazzo, E., 2012. Impact Cratering: Processes and Products, Planetary Surface Processes. https://doi.org/10.1017/cbo9780511977848.007

Osinski, G.R., Tornabene, L.L., Grieve, R.A.F., 2011. Impact ejecta emplacement on terrestrial planets. Earth Planet. Sci. Lett. 310, 167–181. https://doi.org/10.1016/j.epsl.2011.08.012

Pierazzo, E., Melosh, H.J., 2000. Melt Production in Oblique Impacts. Icarus 145, 252–261. https://doi.org/10.1006/icar.1999.6332

Pike, R.J., 1980. Formation of complex impact craters: Evidence from Mars and other planets. Icarus 43, 1–19. https://doi.org/10.1016/0019-1035(80)90083-4

Pike, R.J., 1977a. Size-dependence in the shape of fresh impact craters on the moon. Impact Explos. Cratering 489–509.

Pike, R.J., 1977b. Apparent depth/apparent diameter relation for lunar craters. Lunar Planet. Inst. Sci. Conf. Abstr. 3427–3436.

Pike, R.J., 1974. Depth/Diameter relations of fresh lunar craters: revision from spacecraft data. Geophys. Res. Lett. 1, 291–294.

Robbins, S.J., Hynek, B.M., 2012. A new global database of Mars impact craters ≥1 km: 2. Global crater properties and regional variations of the simple-to-complex transition diameter. J. Geophys. Res. E Planets 117, 1–21. https://doi.org/10.1029/2011JE003967

Schaber, G.G., Strom, R.G., Moore, H.J., Soderblom, L.A., Kirk, R.L., Chadwick, D.J., Dawson, D.D., Gaddis, L.R., Boyce, J.M., Russell, J., 1992. Geology and Distribution of Impact Craters on Venus: What are they telling us? J. Geophys. Res. 97, 13,257-13,301.

Schmidt, R.M., Housen, K.R., 1987. Some recent advances in the scaling of impact and explosion cratering. Int. J. Impact Eng. 5, 543–560.

Schubert, G., Russell, C.T., Moore, W.B., 2000. Timing of the Martain dynamo. Nature 408, 666–667.

Schultz, P.H., 1993. Impact crater growth in an atmosphere. Int. J. Impact Eng. 14, 659–670.

Schultz, P.H., 1992. Atmospheric effects on ejecta emplacement. J. Geophys. Res. 97. https://doi.org/10.1029/92je00613

Schultz, P.H., 1988. Cratering on Mercury: a relook, in: Vilas, F., Chapman, C., Matthews, M. (Eds.), Mercury. The University of Arizona Press, pp. 274–335.

Shoemaker, E.M., 1960. Penetration mechanics of high velocity meteorites, illustrated by Meteor Crater, Arizona. Berlingske bogtr.

Silber, E.A., Osinski, G.R., Johnson, B.C., Grieve, R.A.F., 2017. Effect of impact velocity and acoustic fluidization on the simple-to-complex transition of lunar craters. J. Geophys. Res. Planets 122, 800–821. https://doi.org/10.1002/2016JE005236

Sizemore, H.G., Platz, T., Schorghofer, N., Prettyman, T.H., De Sanctis, M.C., Crown, D.A., Schmedemann, N., Neesemann, A., Kneissl, T., Marchi, S., Schenk, P.M., Bland, M.T., Schmidt, B.E., Hughson, K.H.G., Tosi, F., Zambon, F., Mest, S.C., Yingst, R.A., Williams, D.A., Russell, C.T., Raymond, C.A., 2017. Pitted terrains on

(1) Ceres and implications for shallow subsurface volatile distribution. Geophys. Res. Lett. 44, 6570–6578. https://doi.org/10.1002/2017GL073970

Smith, D.E., Zuber, M.T., Frey, H. V., Garvin, J.B., Head, J.W., Muhleman, D.O., Pettengill, G.H., Phillips, R.J., Solomon, S.C., Zwally, H.J., Banerdt, W.B., Duxbury, T.C., Golombek, M.P., Lemoine, F.G., Neumann, G.A., Rowlands, D.D., Aharonson, O., Ford, P.G., Ivanov, A.B., Johnson, C.L., McGovern, P.J., Abshire, J.B., Afzal, R.S., Sun, X., 2001. Mars Orbiter Laser Altimeter: Experiment summary after the first year of global mapping of Mars. J. Geophys. Res. E Planets 106, 23689–23722. https://doi.org/10.1029/2000JE001364

Sohl, F., Spohn, T., 1997. The interior structure of Mars: Implications from SNC meteorites. J. Geophys. Res. 102, 1613–1635.

Stevenson, D.J., 2001. Mars' core and magnetism. Nature 412, 214–219. https://doi.org/10.1038/35084155

Stewart, S.T., O'Keefe, J.D., Ahrens, T.J., 2001. The relationship between rampart crater morphologies and the amount of subsurface ice. Lunar Planet. Sci. Conf. 32nd abstract #2092.

Stöffler, D., Ryder, G., Ivanov, B.A., Artemieva, N.A., Cintala, M.J., Grieve, R.A.F., 2006. Cratering history and Lunar Chrnology. Rev. Mineral. Geochemistry 60, 519–596. https://doi.org/10.2138/rmg.2006.60.05

Stopar, J.D., Hawke, B.R., Robinson, M.S., Denevi, B.W., Giguere, T.A., Koeber, S.D., 2014. Occurrence and mechanisms of impact melt emplacement at small lunar craters. Icarus 243, 337–357. https://doi.org/10.1016/j.icarus.2014.08.011

Strom, R.G., Banks, M.E., Chapman, C.R., Fassett, C.I., Forde, J.A., Head, J.W., Merline, W.J., Prockter, L.M., Solomon, S.C., 2011. Mercury crater statistics from MESSENGER flybys: Implications for stratigraphy and resurfacing history. Planet. Space Sci. 59, 1960–1967. https://doi.org/10.1016/j.pss.2011.03.018

Strom, R.G., Croft, S.K., Barlow, N.G., 1992. The Martain impact cratering record, in:

Mars. The University of Arizona Press, pp. 383–423.

Strom, R.G., Fielder, G., 1970. MULTIPHASE ERUPTIONS ASSOCIATED WITH THE LUNAR CRATERS TYCHO AND ARISTARCHUS. Commun. Lunar Planet. Lab 8, 235–288.

Strom, R.G., Fielder, G., 1968. Multiphase development of the lunar crater tycho. Nature 217, 611–615. https://doi.org/10.1038/217611a0

Susorney, H.C.M., Barnouin, O.S., Ernst, C.M., Johnson, C.L., 2016. Morphometry of impact craters on Mercury from MESSENGER altimetry and imaging. Icarus 271, 180–193. https://doi.org/10.1016/j.icarus.2016.01.022

Tauber, M.E., Kirk, D.B., 1976. Impact Craters on Venus. Icarus 351–357.

Tornabene, L.L., McEwen, A.S., Grant, J.A., Mouginis-Mark, P.J., Squyres, S.W., Wray, J.J., 2007a. Evidence for the role of volatiles on martian impact craters as revealed by HiRISE. Lunar Planet. Sci. Conf. 38th.

Tornabene, L.L., McEwen, A.S., Osinski, G.R., Mouginis-Mark, P.J., Boyce, J.M., Williams, R.M.E., Wray, J.J., Grant, J. a, 2007b. Impact melting and the role of subsurface volatiles: Implications for the formation of valley networks and phyllosilicate-rich lithologies on early Mars. Seventh Int. Conf. Mars Abstract 3288.

Tornabene, L.L., Moersch, J.E., McSween, H.Y., McEwen, A.S., Piatek, J.L., Milam, K.A., Christensen, P.R., 2006. Identification of large (2-10 km) rayed craters on Mars in THEMIS thermal infrared images: Implications for possible Martian meteorite source regions. J. Geophys. Res. E Planets 111, 1–25. https://doi.org/10.1029/2005JE002600

Tornabene, L.L., Osinski, G.R., McEwen, A.S., Boyce, J.M., Bray, V.J., Caudill, C.M., Grant, J.A., Hamilton, C.W., Mattson, S., Mouginis-Mark, P.J., 2012. Widespread crater-related pitted materials on Mars: Further evidence for the role of target volatiles during the impact process. Icarus 220, 348–368. https://doi.org/10.1016/j.icarus.2012.05.022

Tornabene, L.L., Watters, W.A., Osinski, G.R., Boyce, J.M., Harrison, T.N., Ling, V., McEwen, A.S., 2018. A depth versus diameter scaling relationship for the best-preserved melt-bearing complex craters on Mars. Icarus 299, 68–83. https://doi.org/10.1016/j.icarus.2017.07.003

Trilling, D.E., 2016. The surface age of sputnik planum, pluto, must be less than 10 million years. PLoS One 11, 5–9. https://doi.org/10.1371/journal.pone.0147386

Ward, A.W., 1979. Yardangs on Mars: Evidence of recent wind erosion. J. Geophys. Res. 84, 8147. https://doi.org/10.1029/jb084ib14p08147

Yoder, C.F., Konopliv, A.S., Yuan, D.N., Standish, E.M., Folkner, W.M., 2003. Fluid core size of Mars from detection of the solar tide. Science (80-.). 300, 299–303. https://doi.org/10.1126/science.1079645

Zuber, M.T., 2000. Internal structure and early thermal evolution of Mars from Mars global surveyor topography and gravity. Science (80-.). 287, 1788–1793. https://doi.org/10.1126/science.287.5459.1788

Zuber, M.T., Smith, D.E., Solomon, S.C., Muhleman, D.O., Head, J.W., Garvin, J.B., Abshire, J.B., Bufton, J.L., 1992. The Mars Observer laser altimeter investigation. J. Geophys. Res. 97, 7781–7797. https://doi.org/10.1029/92JE00341

Appendix A

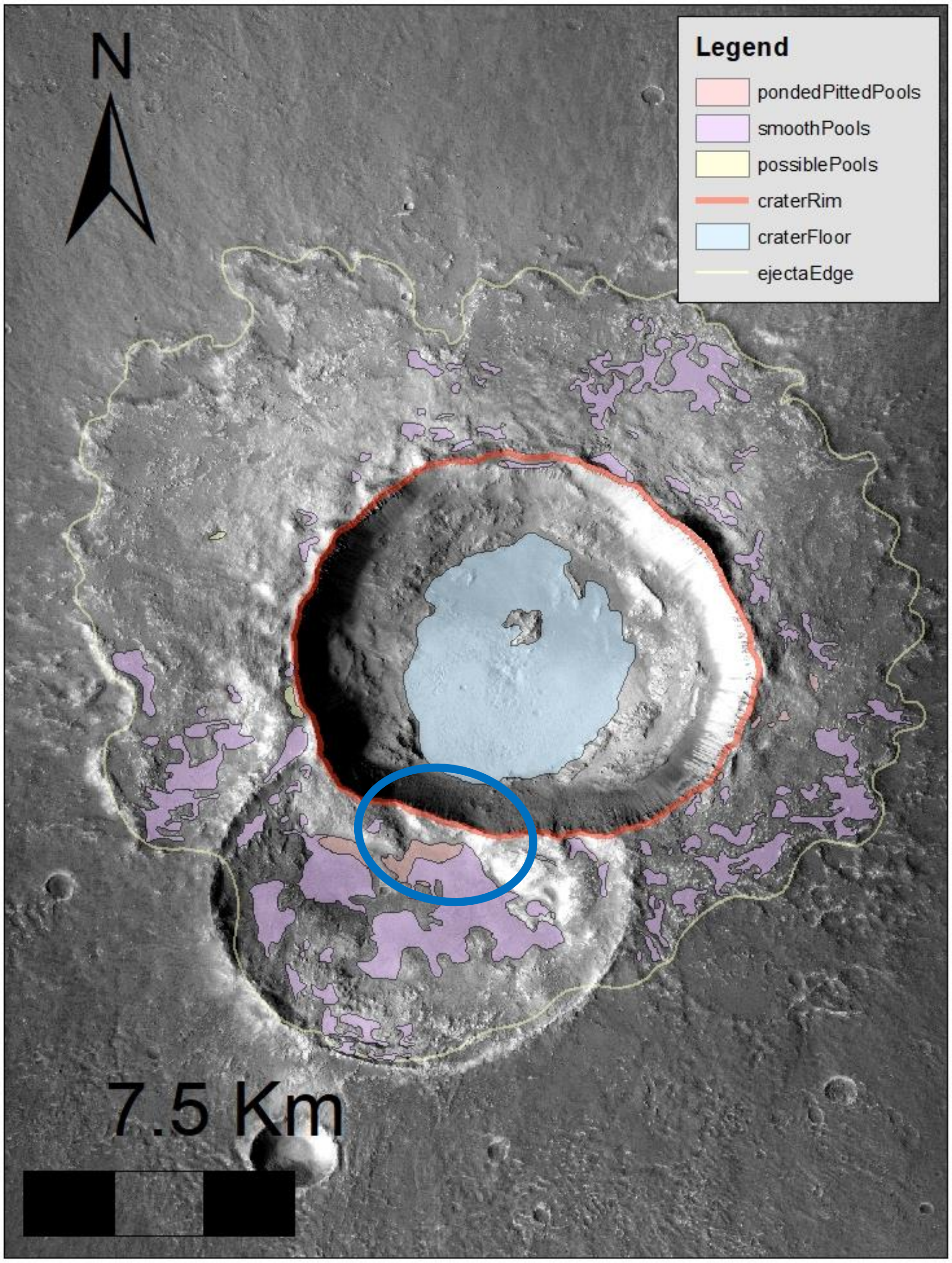

Appendix A Figure 1. Map of candidate crater "AcheronFossae". Rim crest low is annotated by blue oval.

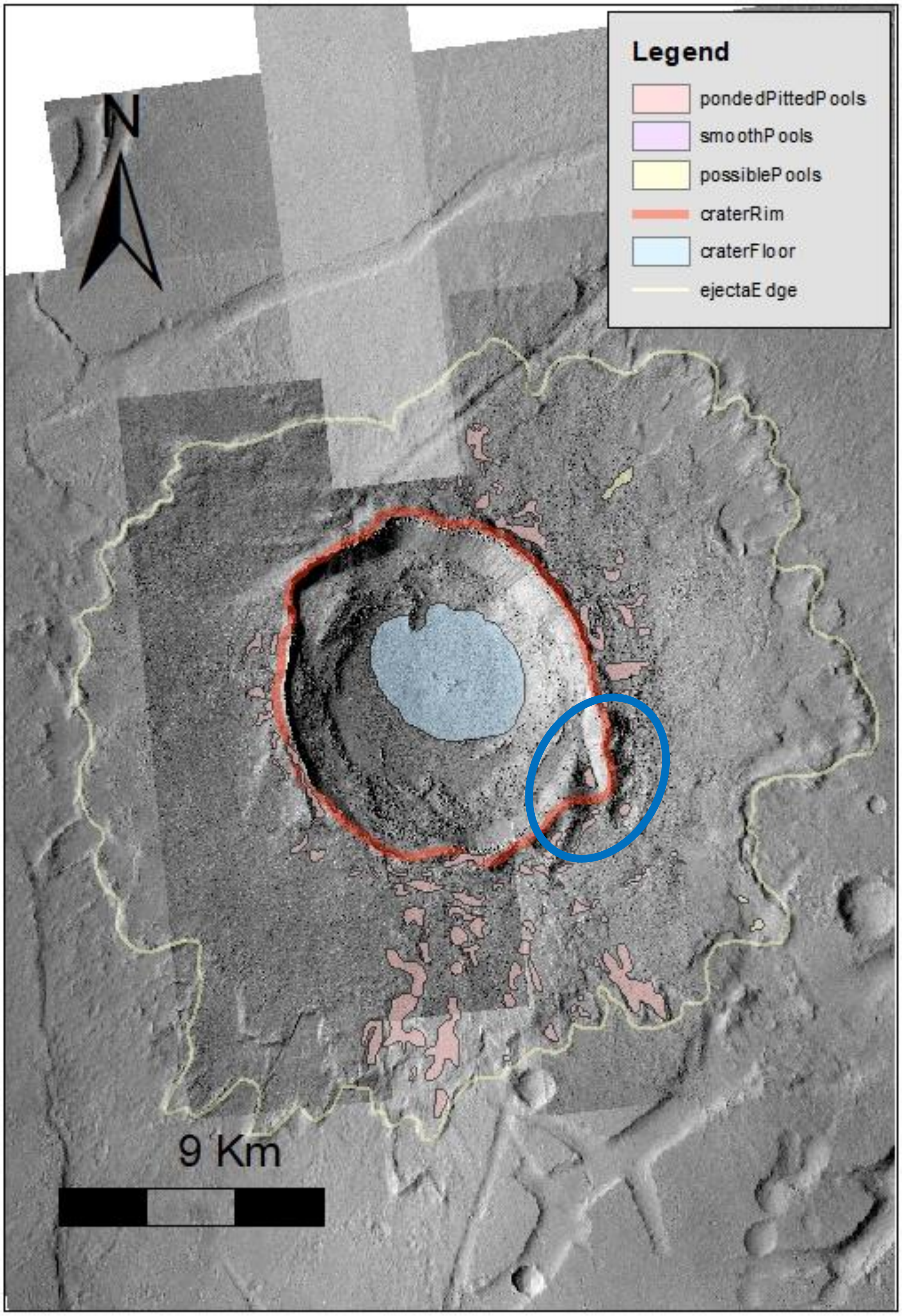

Appendix A Figure 2 Map of candidate crater Canala. Rim crest low is annotated by blue oval.

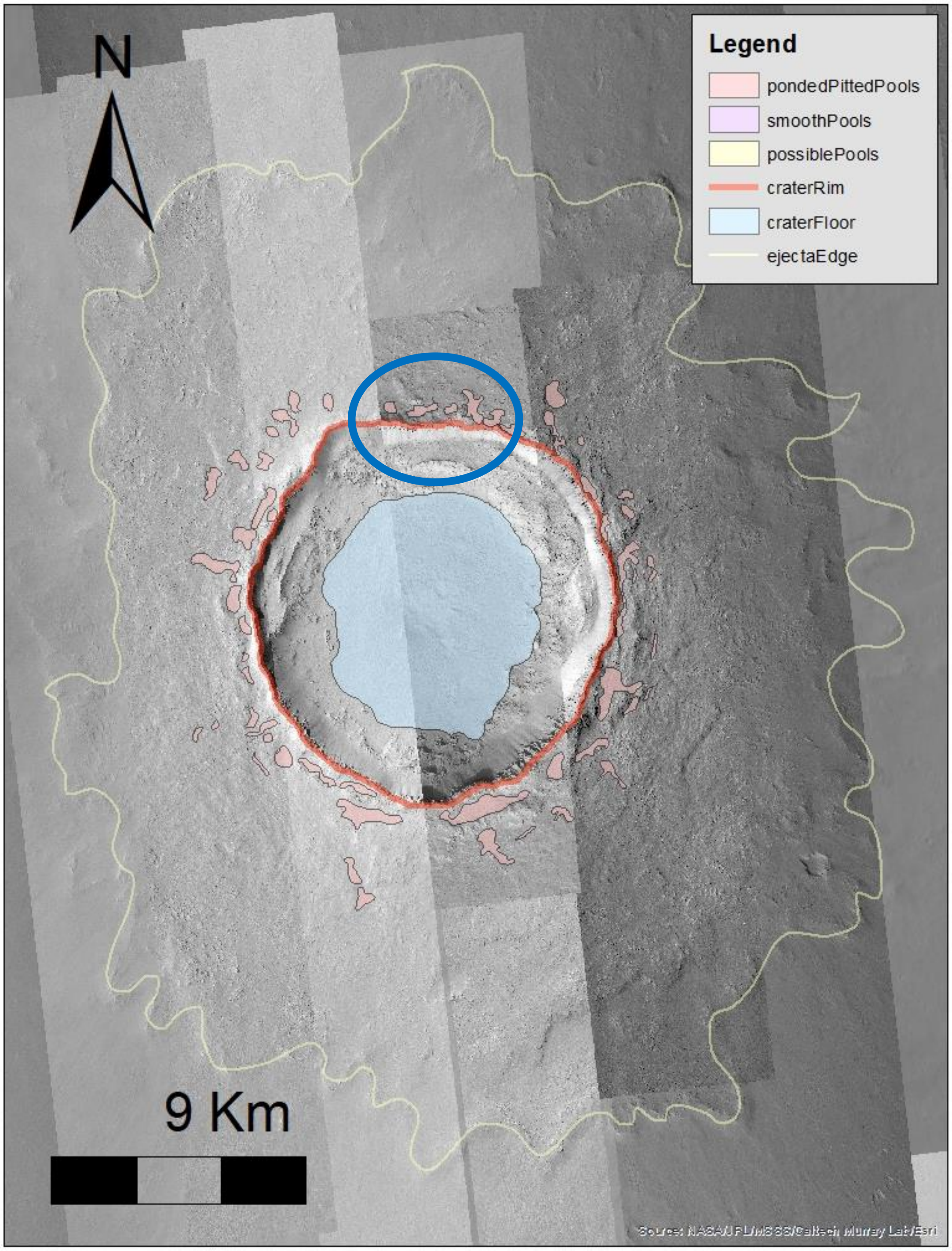

Appendix A Figure 3 Map of candidate crater Corinto. Rim crest low is annotated by blue oval.

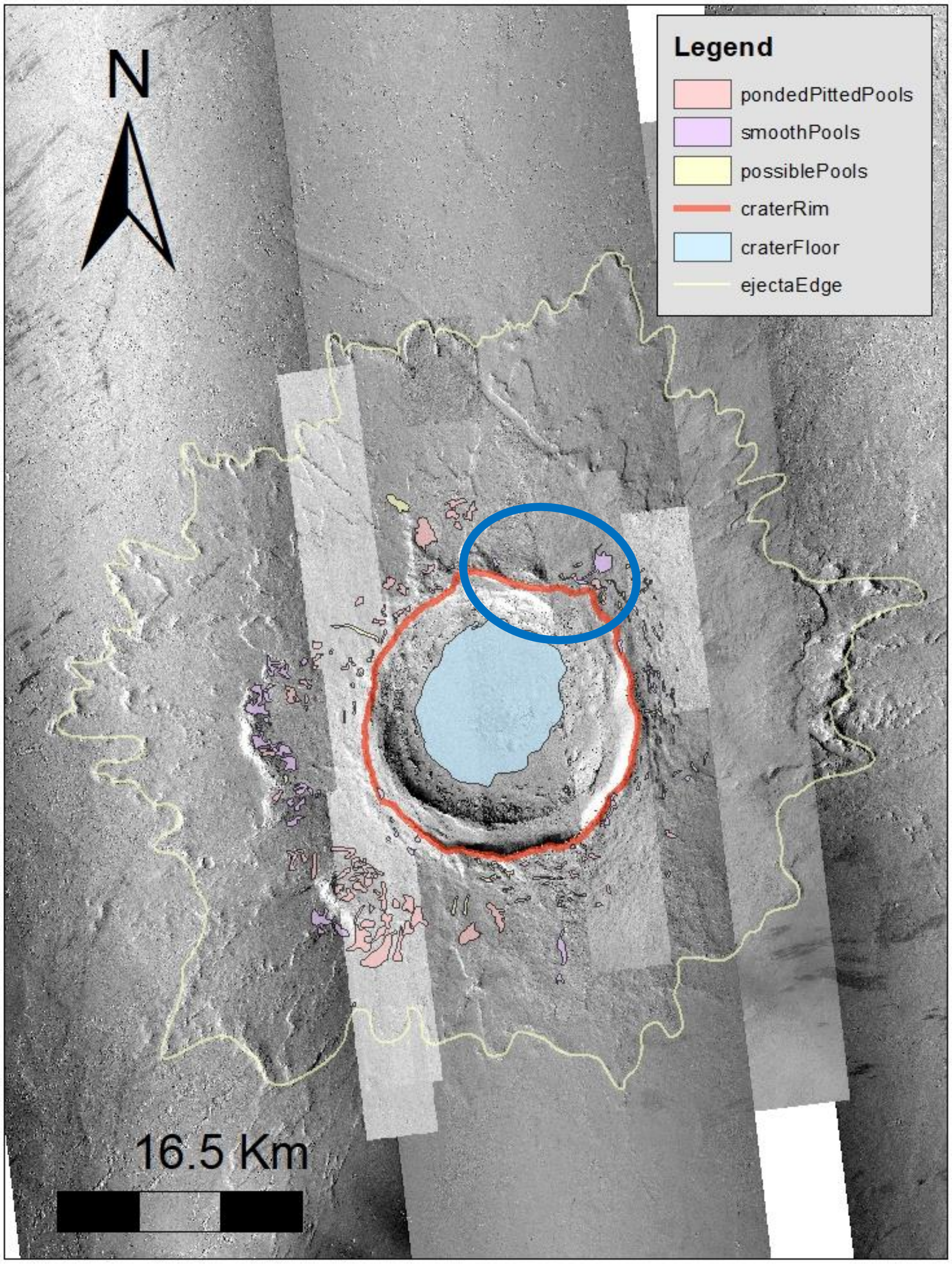

Appendix A Figure 4 Map of candidate crater "craterNEAscreausMons". Rim crest low is annotated by blue oval.

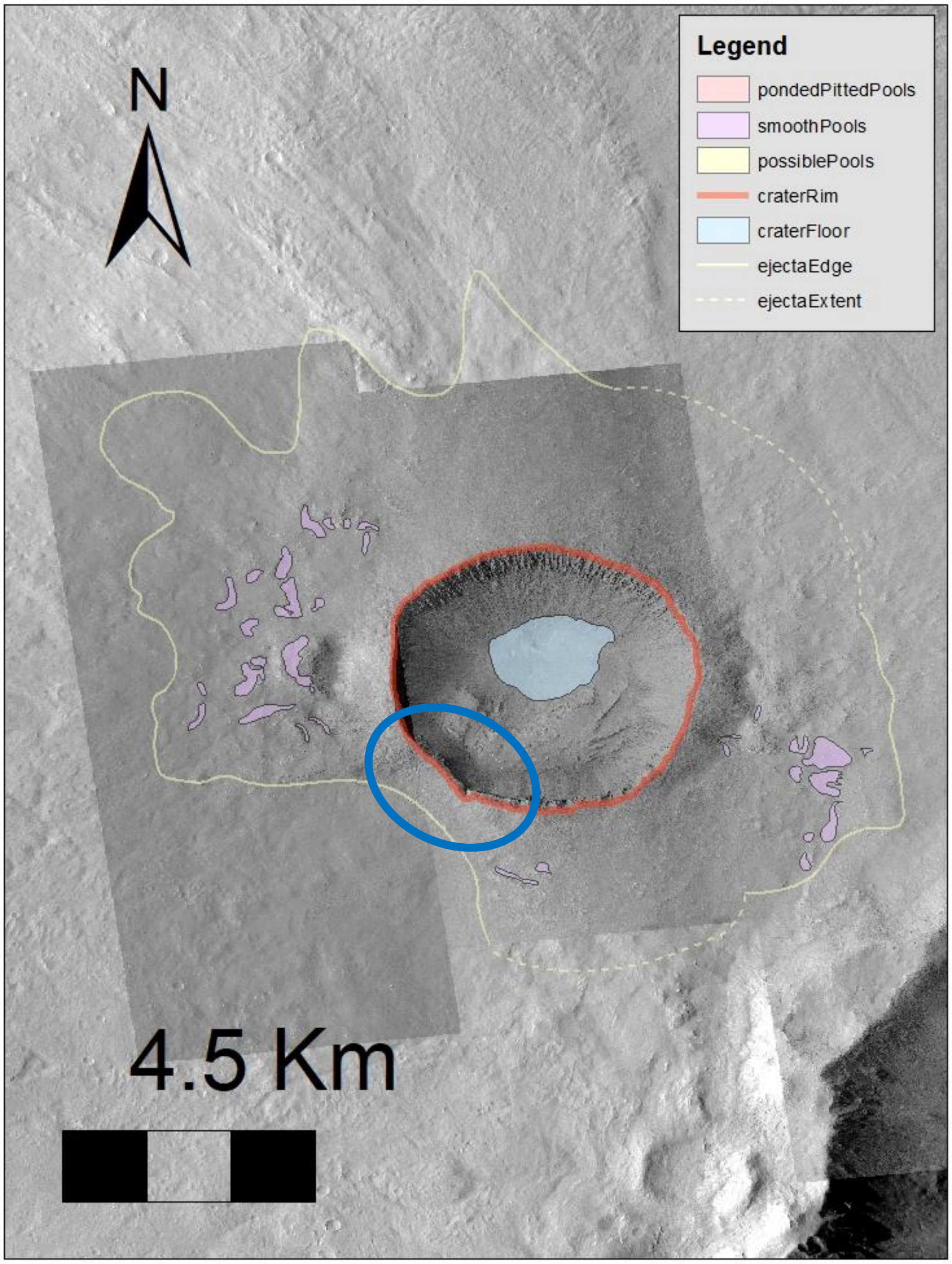

Appendix A Figure 5 Map of candidate crater Istok. Rim crest low is annotated by blue oval.

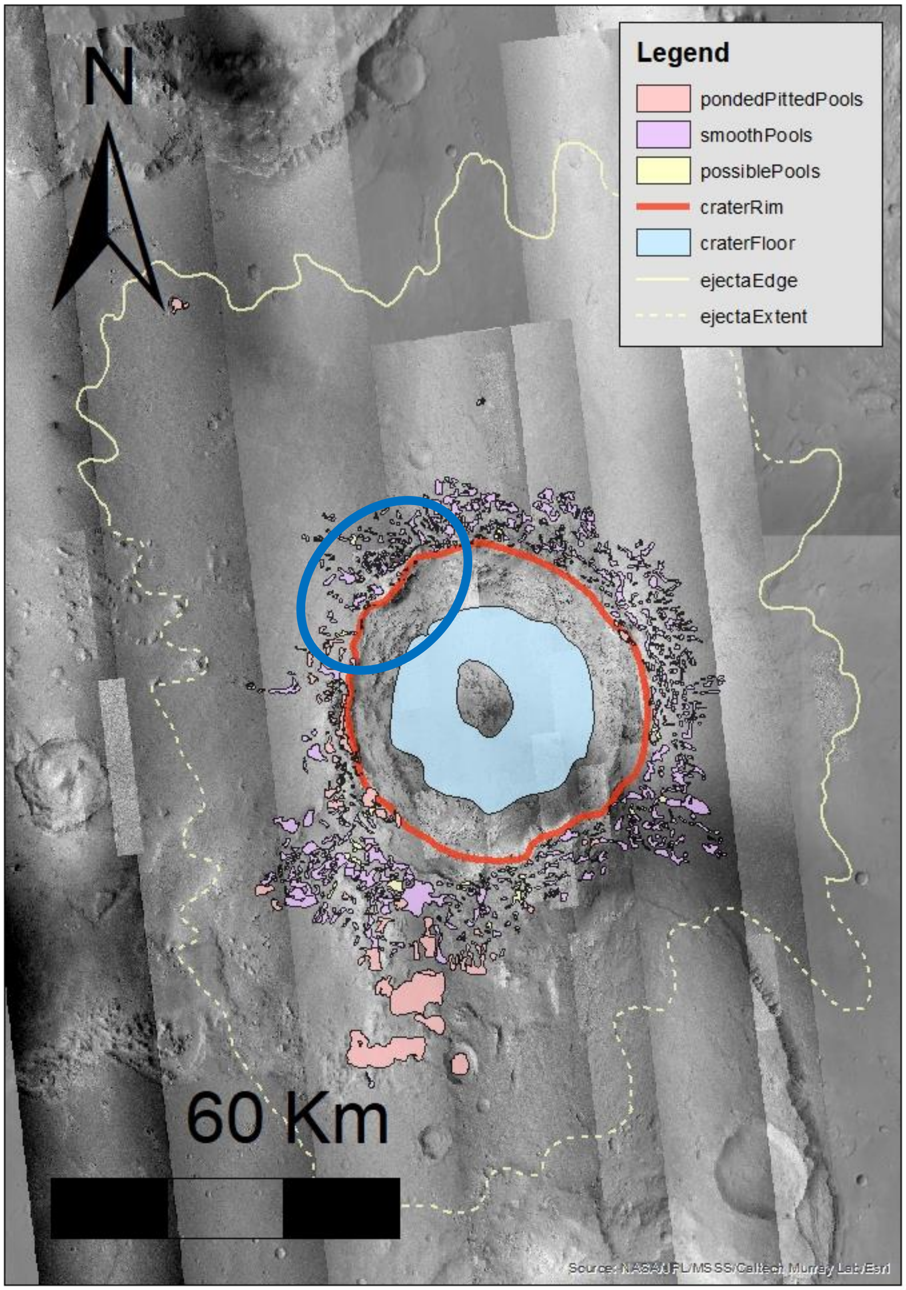

Appendix A Figure 6 Map of candidate crater Mojave. Base map by NASA JPL/MSSS/Caltech Murray Lab/Esri. Rim crest low is annotated by blue oval.

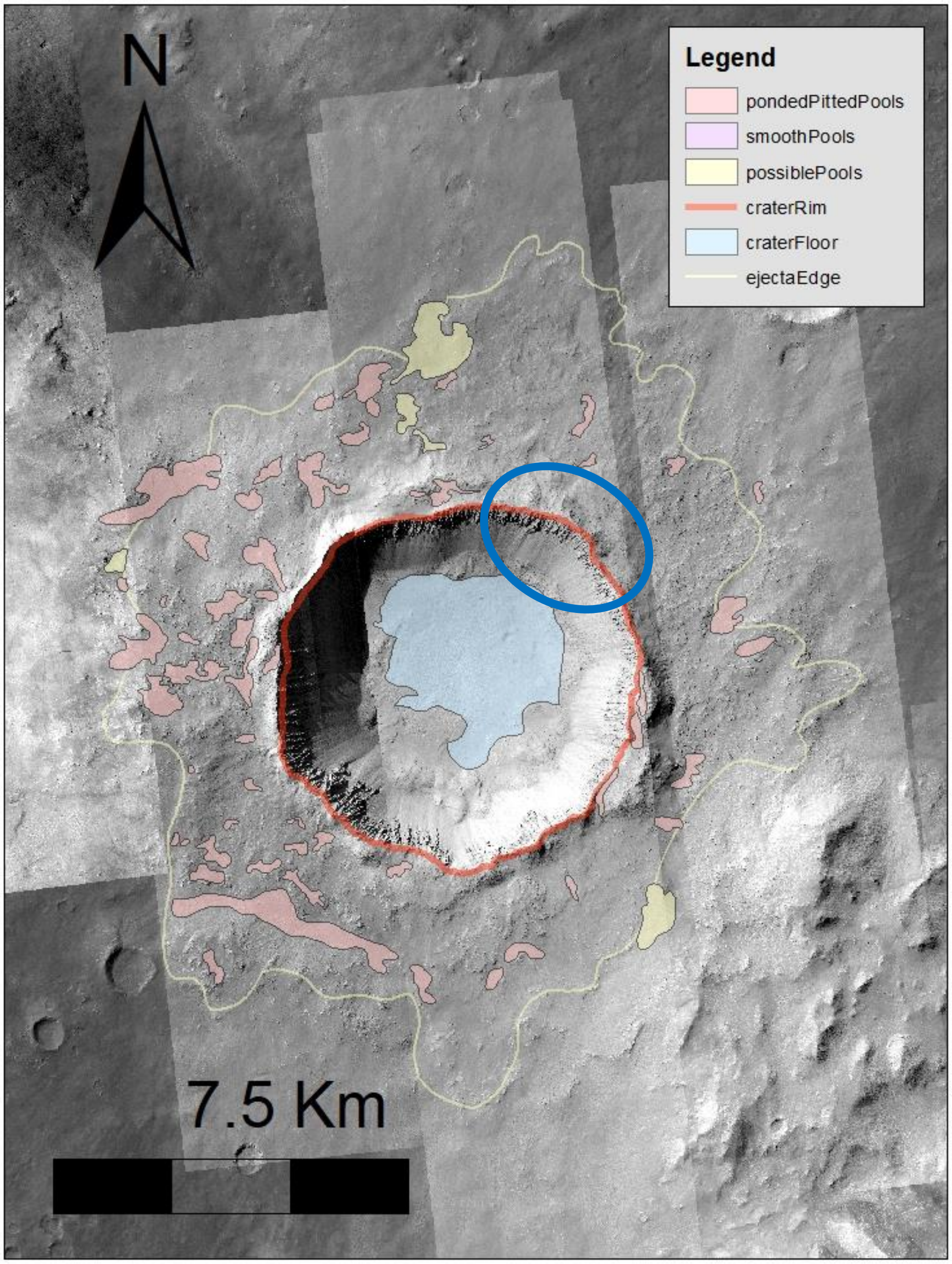

Appendix A Figure 7 Map of candidate crater Noord. Rim crest low is annotated by blue oval.

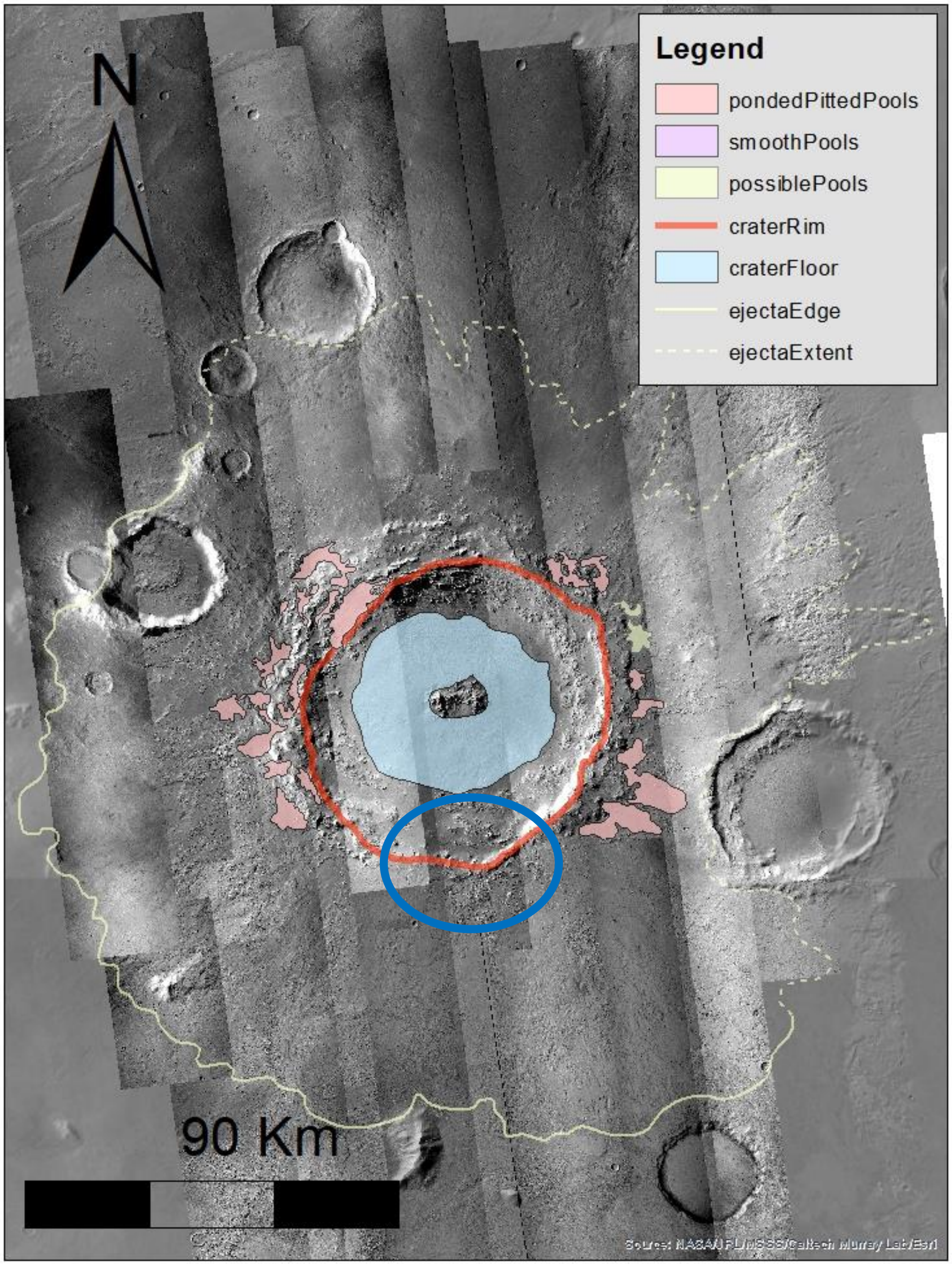

Appendix A Figure 8 Map of candidate crater Pál. Base map by NASA JPL/MSSS/Caltech Murray Lab/Esri. Rim crest low is annotated by blue oval.

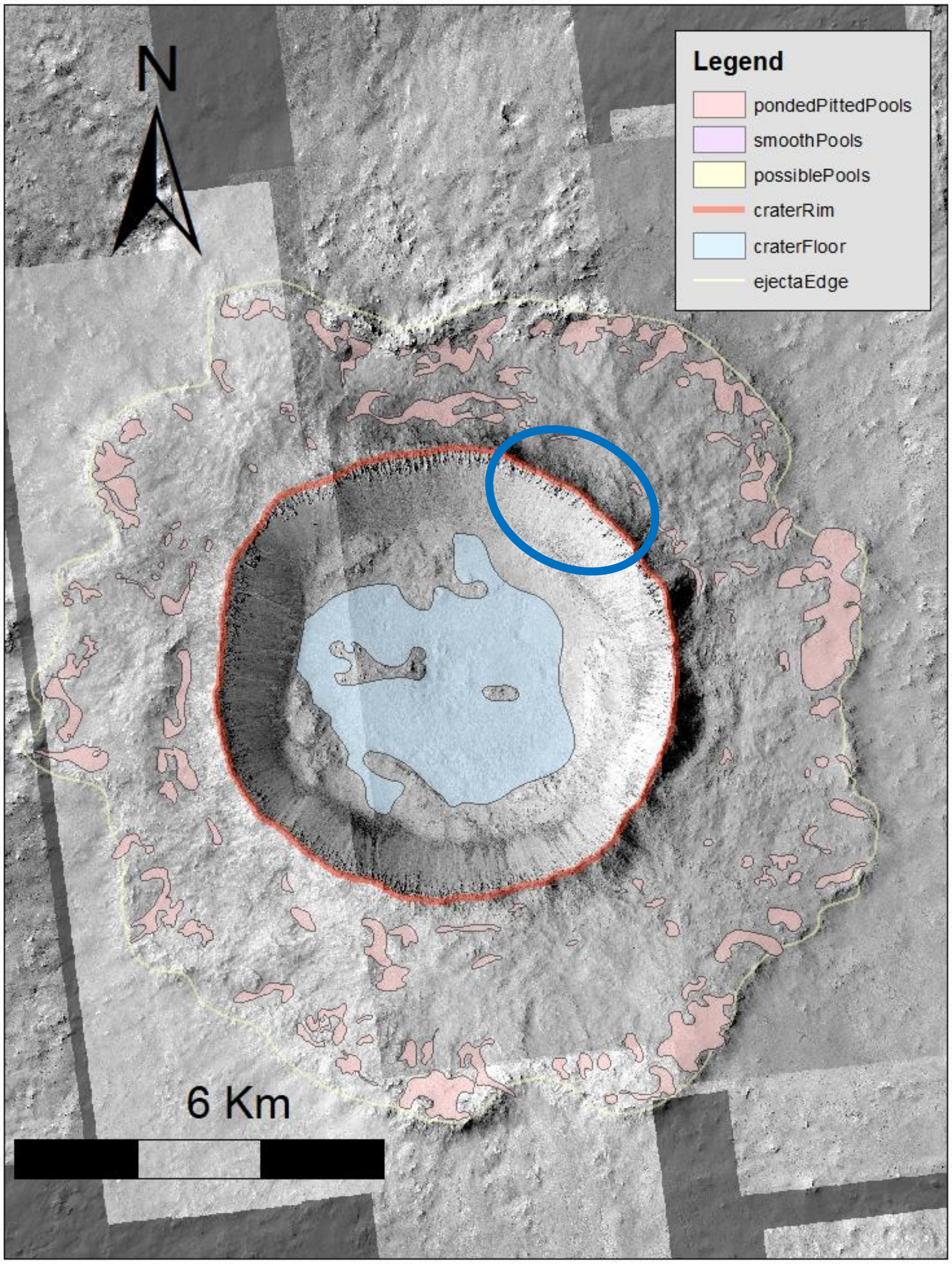

Appendix A Figure 9 Map of candidate crater Resen. Rim crest low is annotated by blue oval.

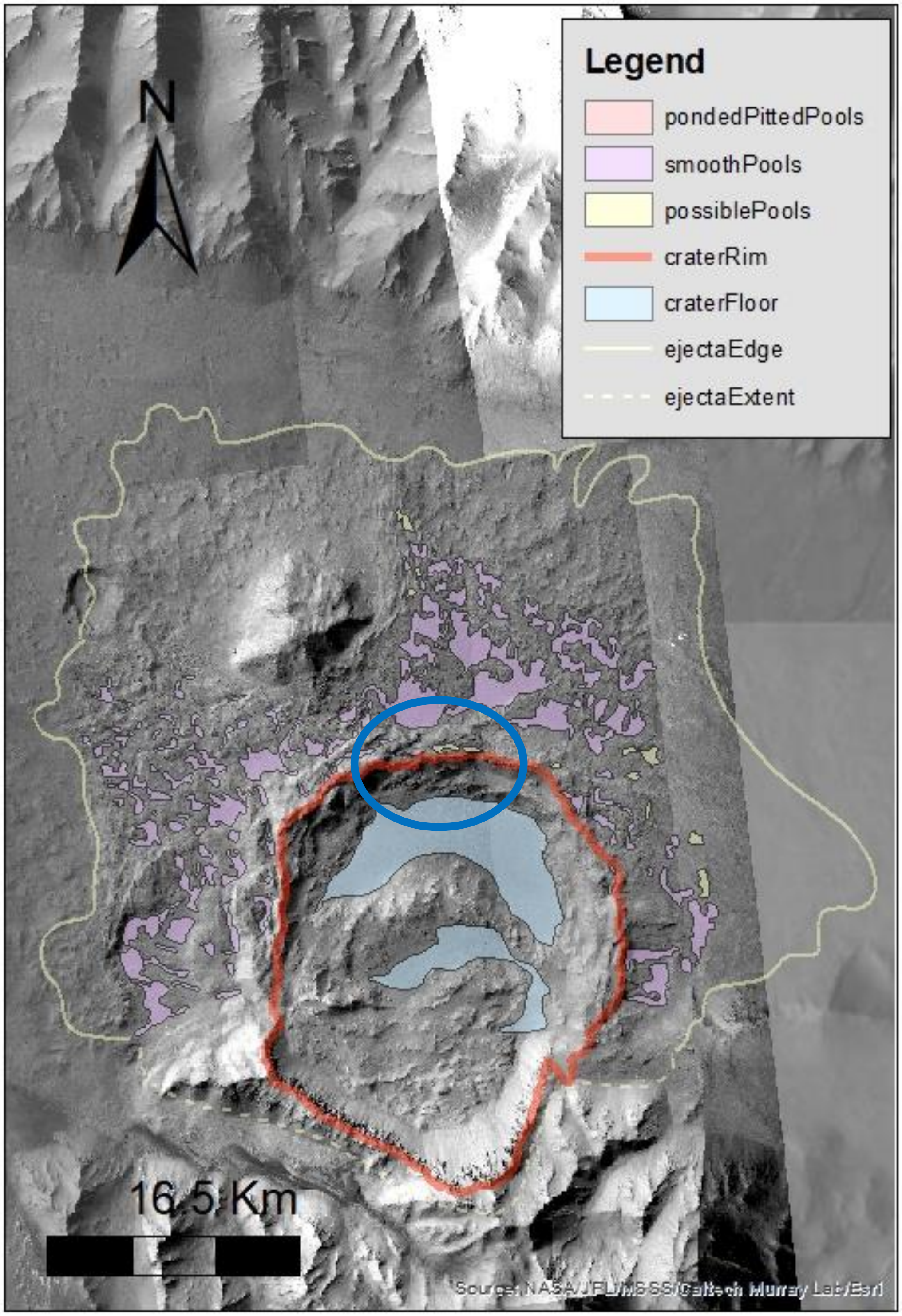

Appendix A Figure 10 Map of candidate crater Sibiti. Base map by NASA JPL/MSSS/Caltech Murray Lab/Esri. Rim crest low is annotated by blue oval.

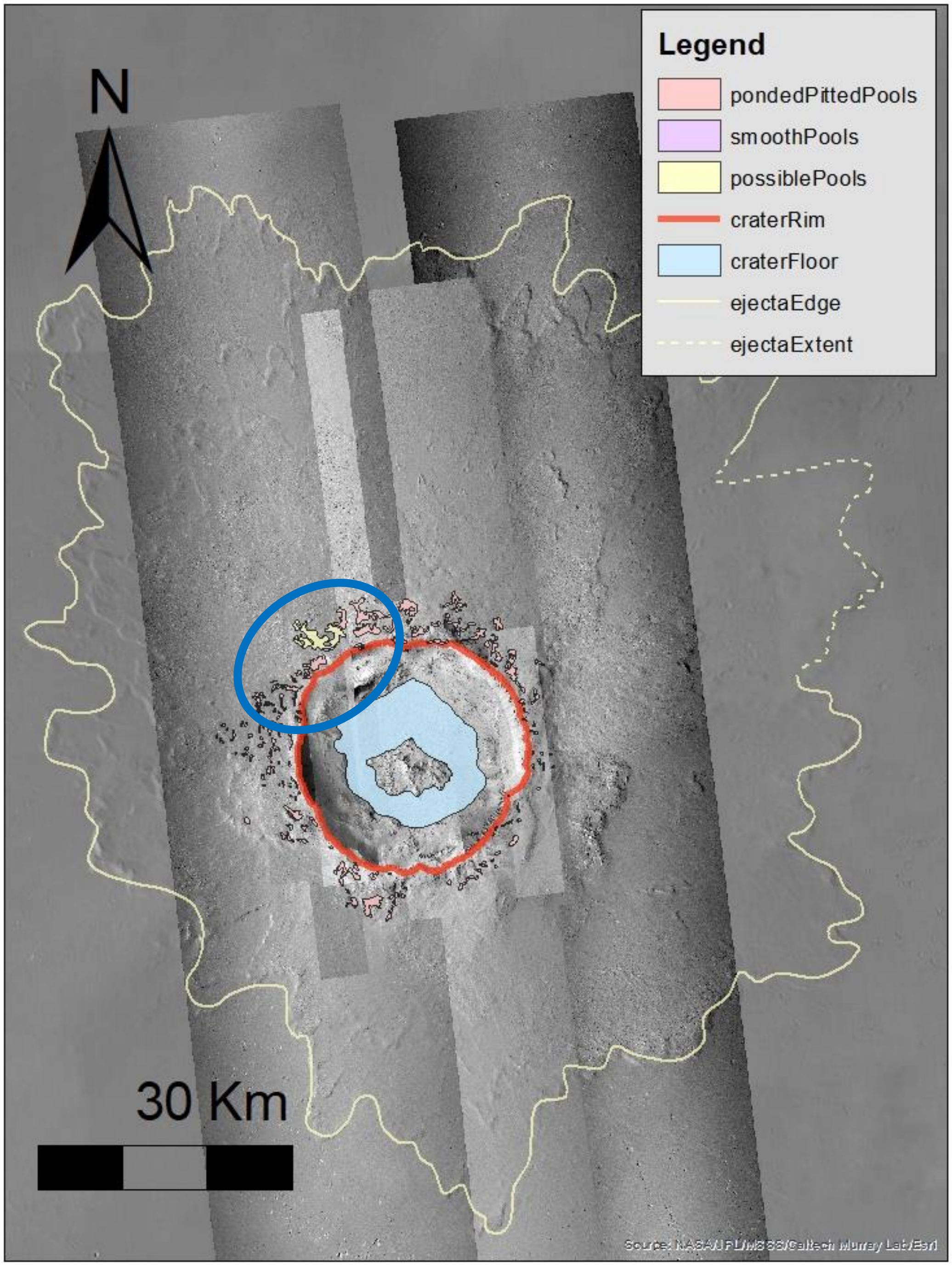

Appendix A Figure 11 Map of candidate crater Tooting. Base map by NASA JPL/MSSS/Caltech Murray Lab/Esri. Rim crest low is annotated by blue oval.

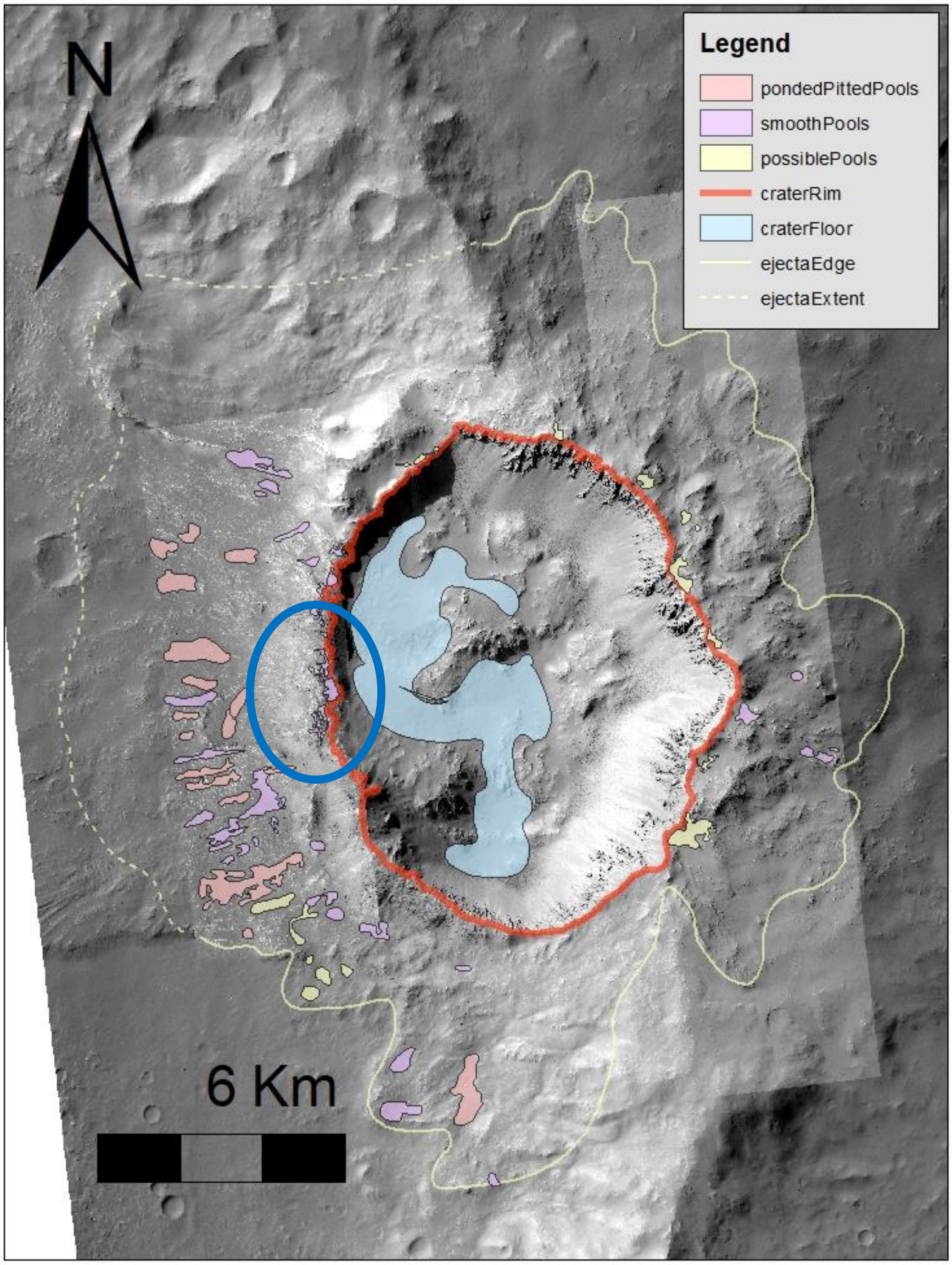

Appendix A Figure 12 Map of candidate crater "TyrrhenaTerra". Rim crest low is annotated by blue oval.

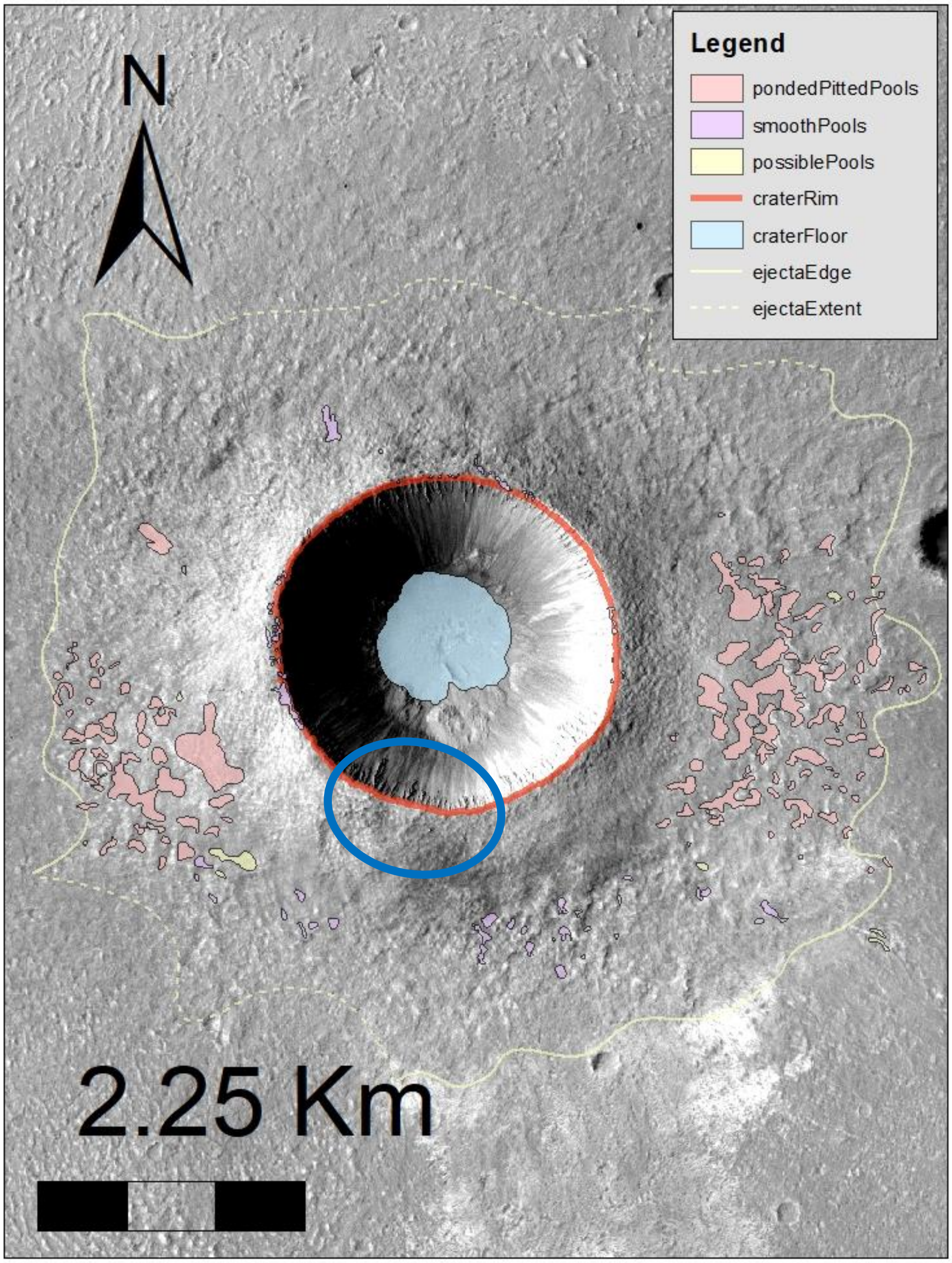

Appendix A Figure 13 Map of candidate crater Zumba. Rim crest low is annotated by blue oval.

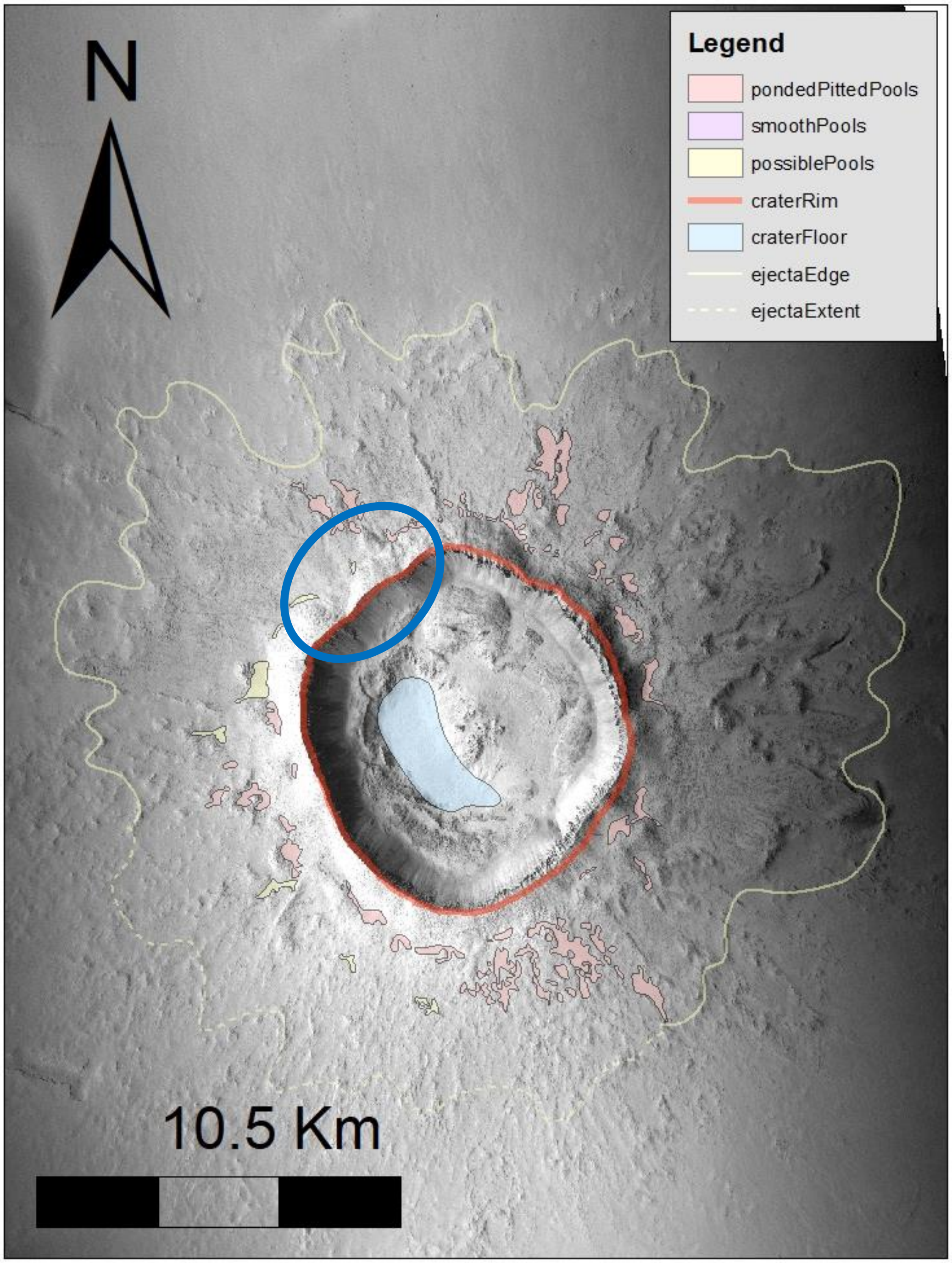

Appendix A Figure 14 Map of candidate crater Zunil. Rim crest low is annotated by blue oval.

Appendix B

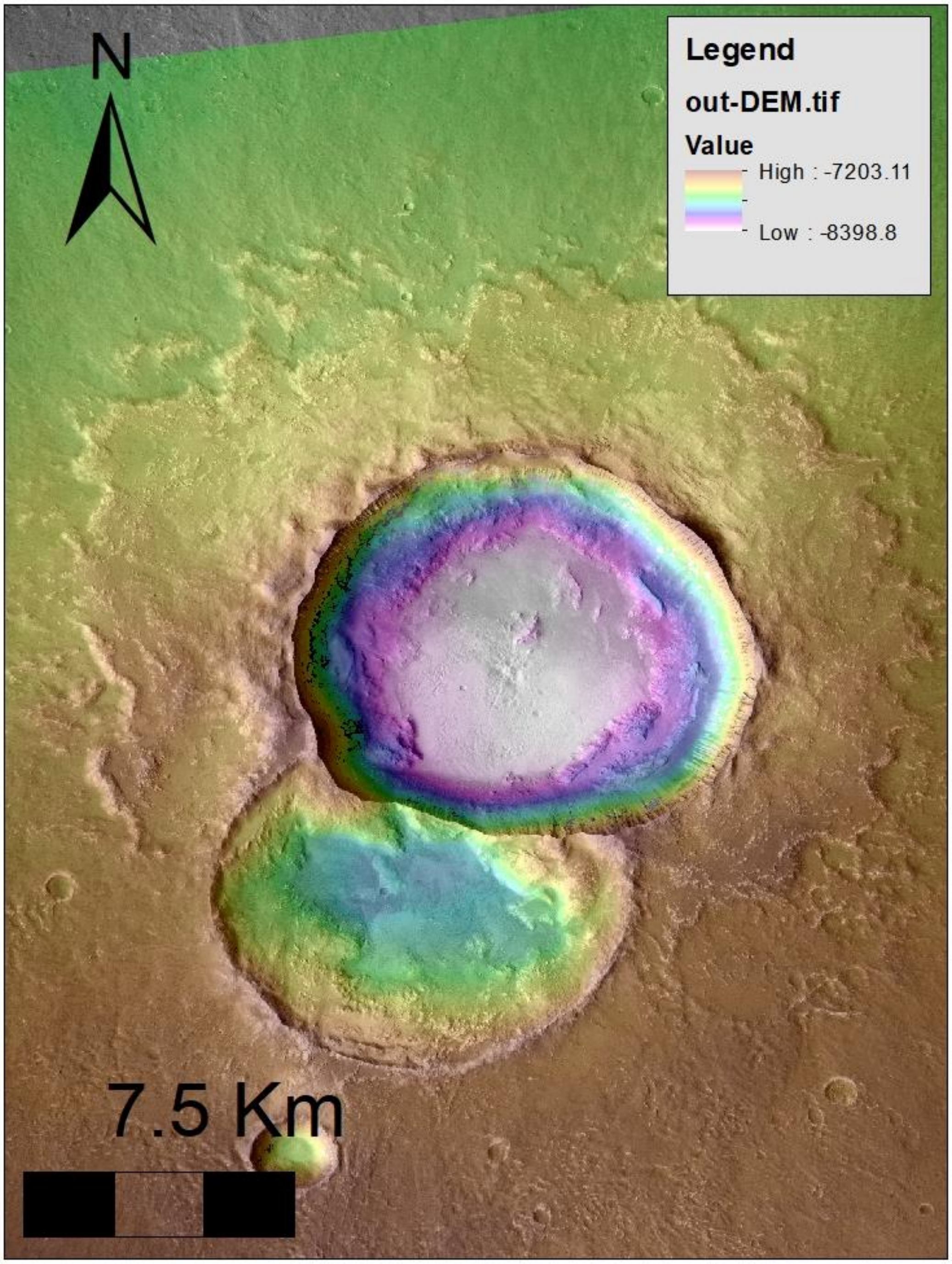

Appendix B Figure 1 CTX DTM of candidate crater "AcheronFossae".

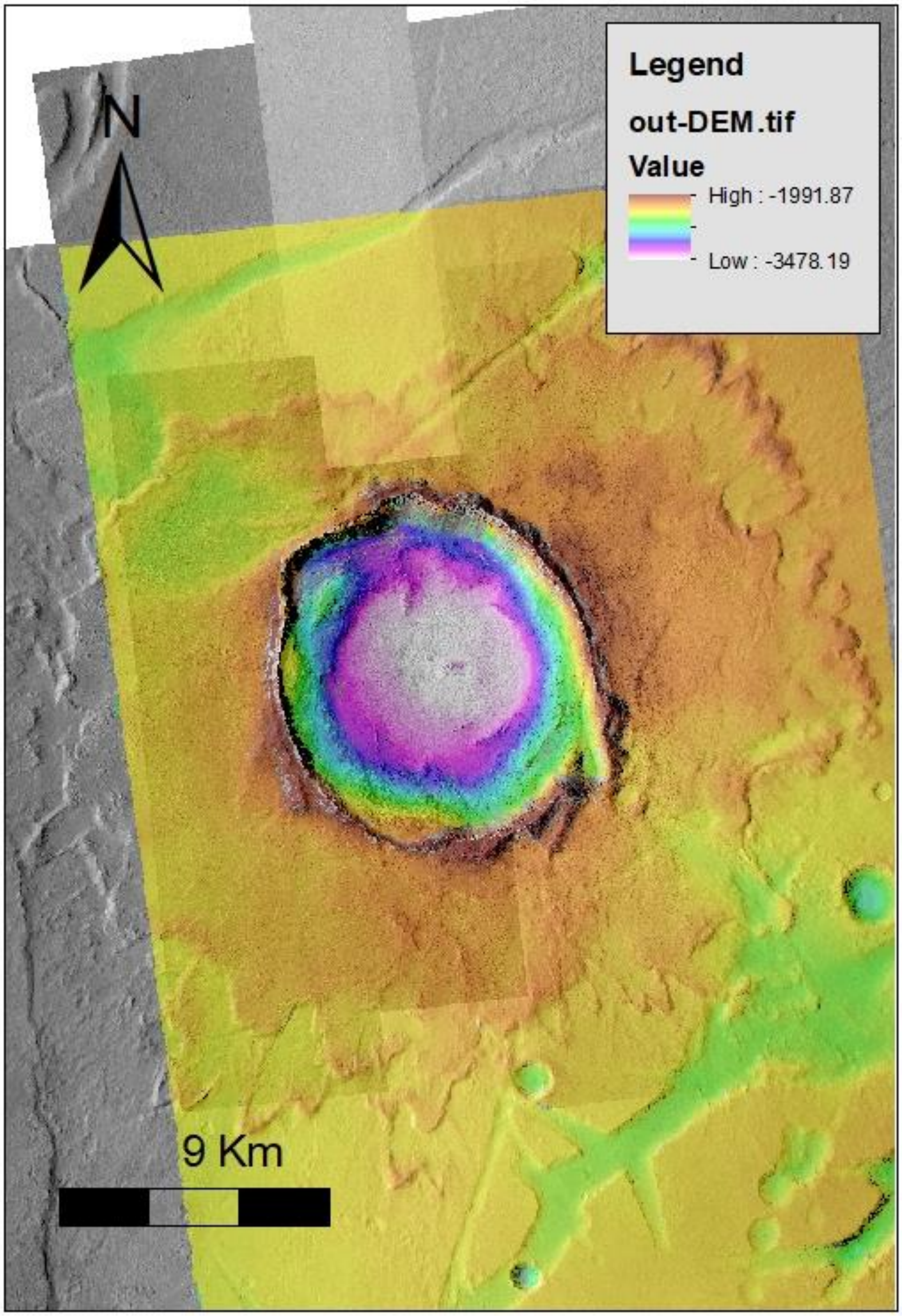

Appendix B Figure 2 CTX DTM of candidate crater Canala.

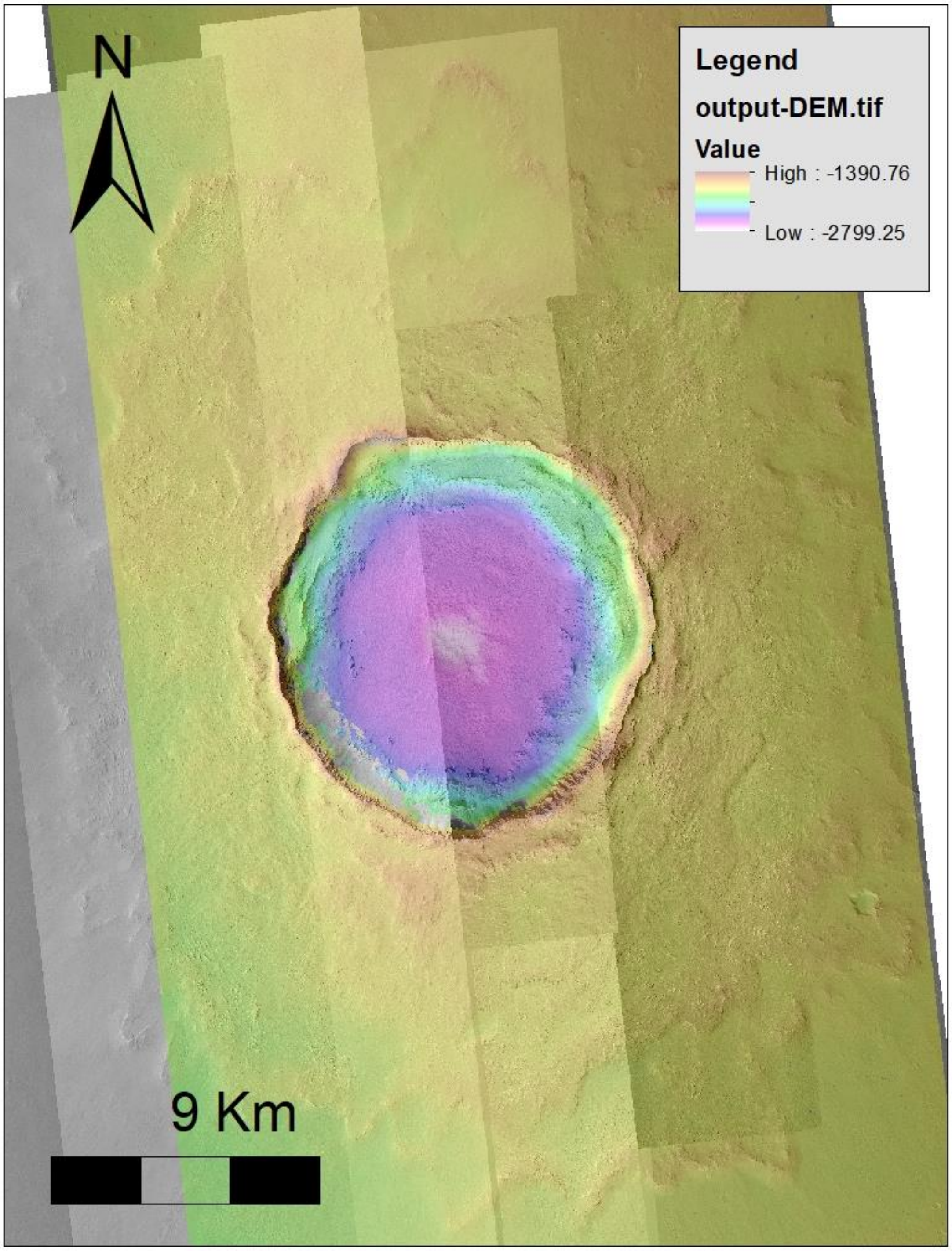

Appendix B Figure 3 CTX DTM of candidate crater Corinto.

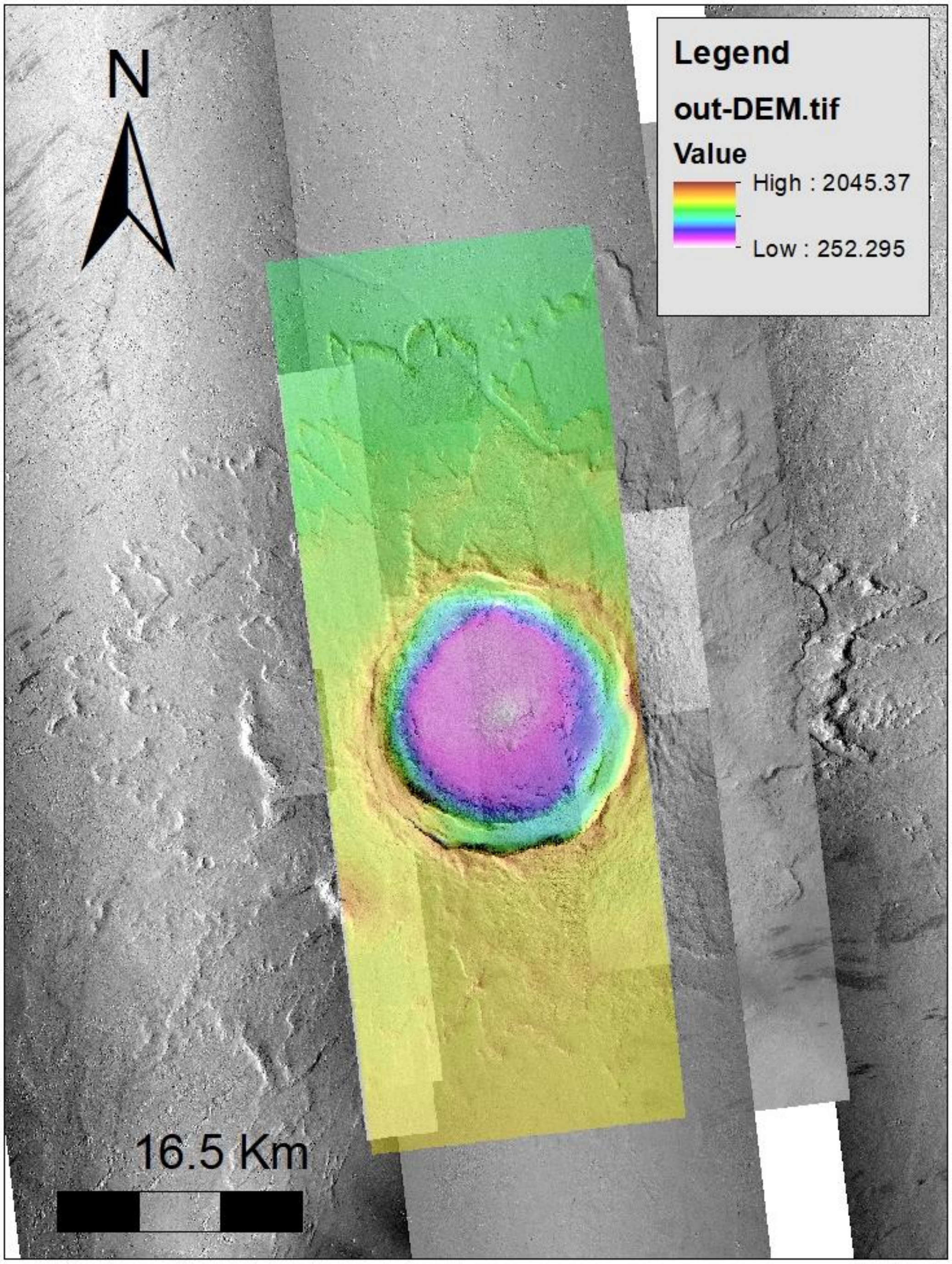

Appendix B Figure 4 CTX DTM of candidate crater "craterNEAscreausMons".

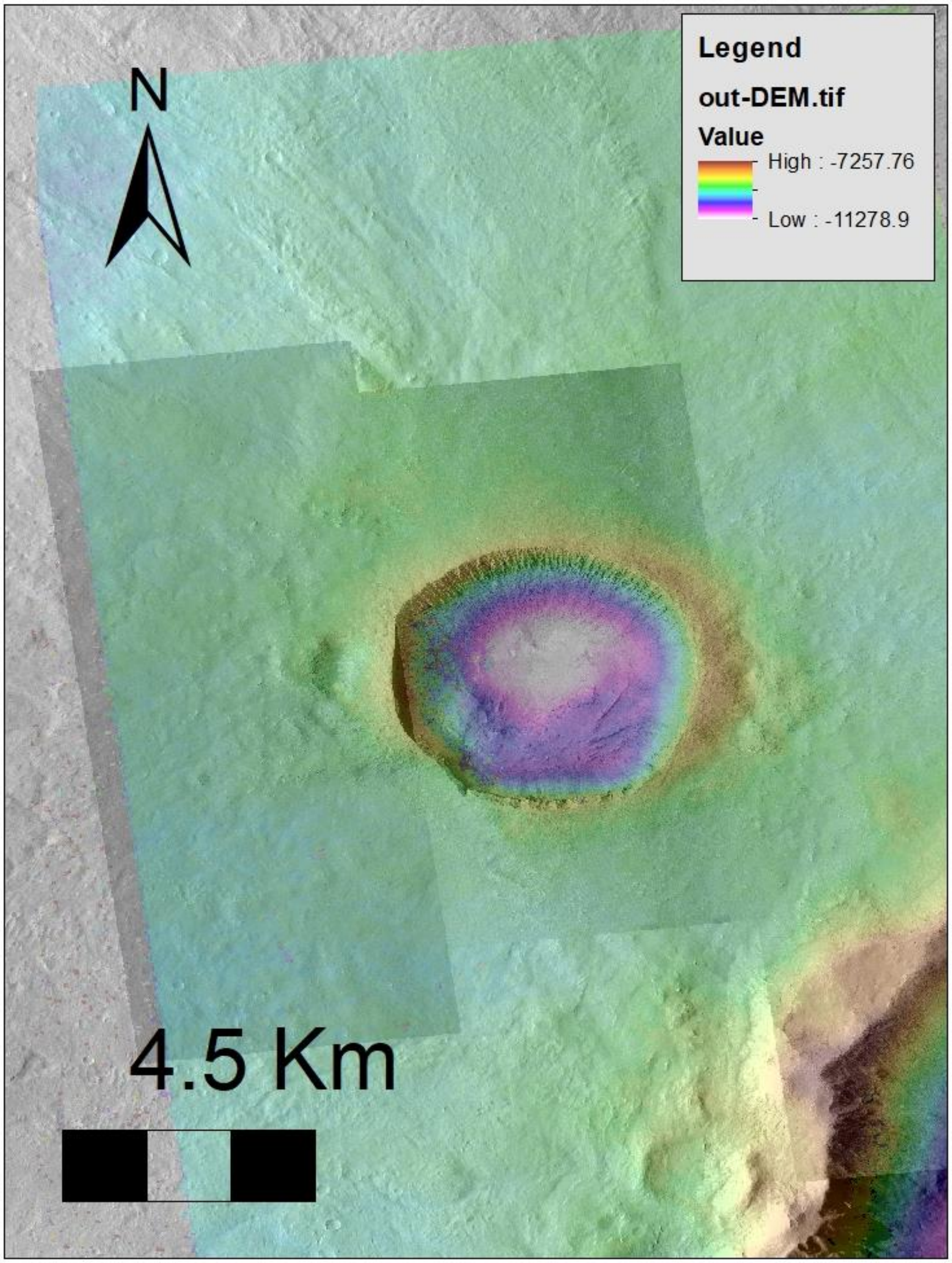

Appendix B Figure 5 CTX DTM of candidate crater Istok.

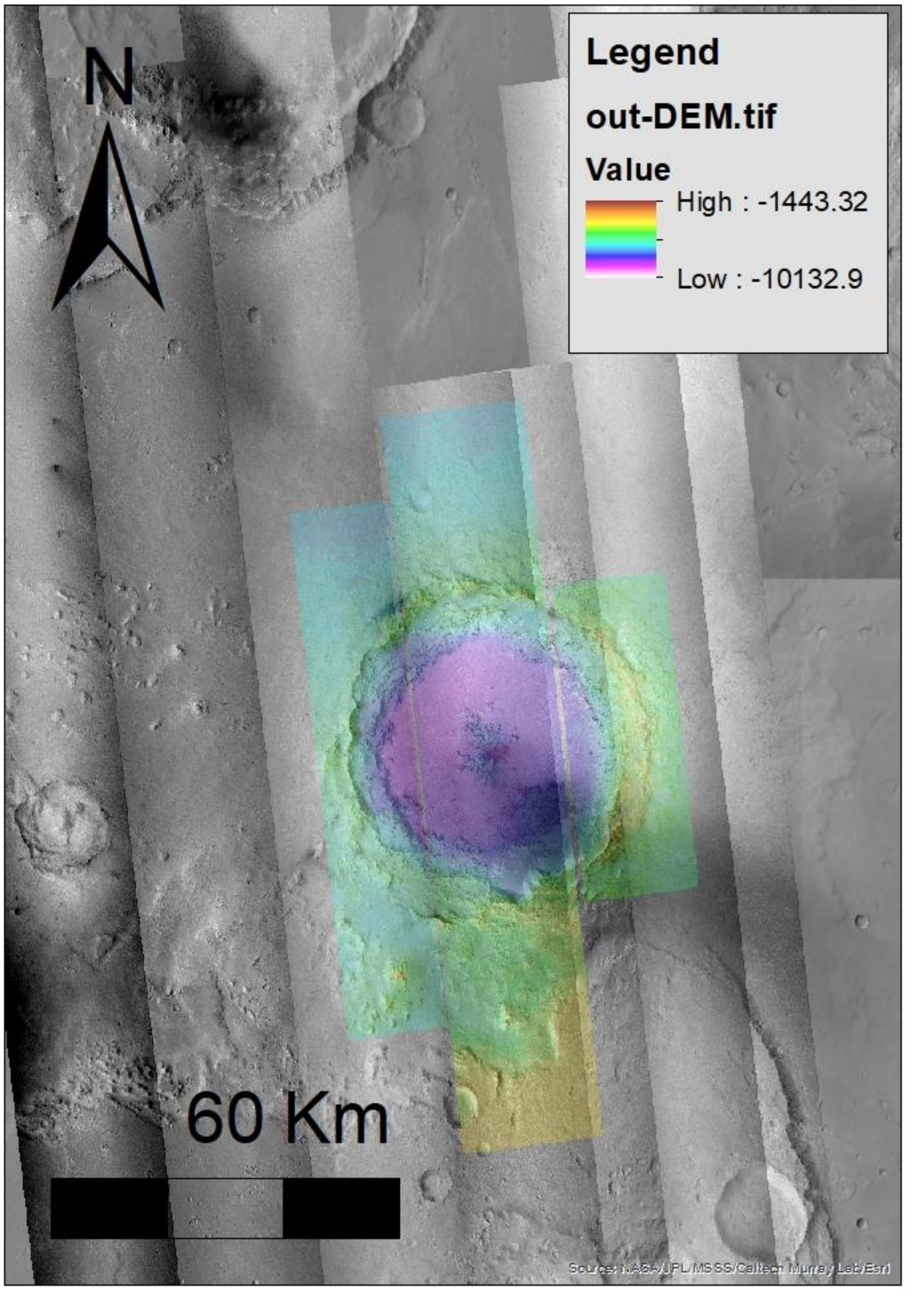

Appendix B Figure 6 CTX DTM of candidate crater Mojave.

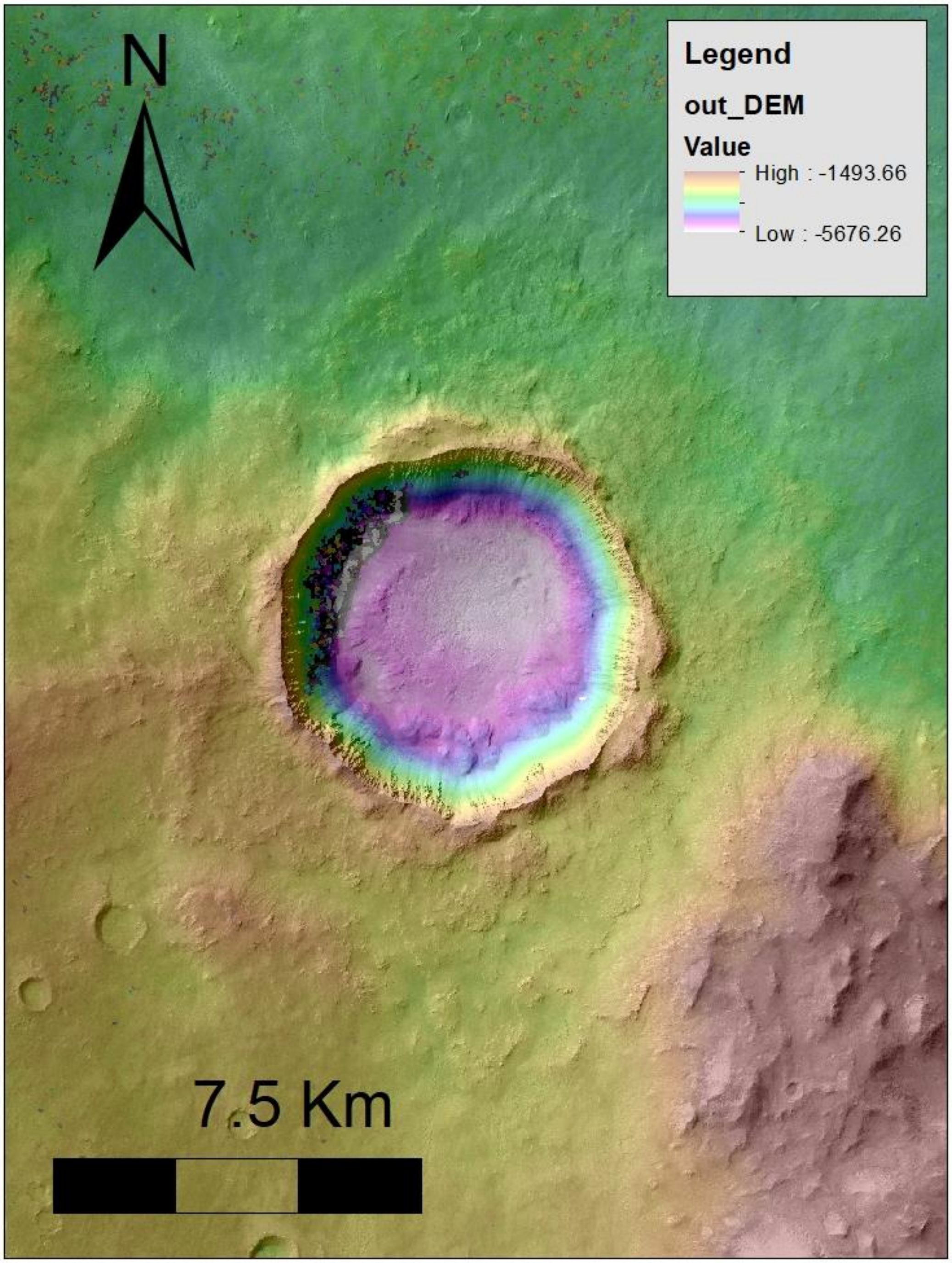

Appendix B Figure 7 CTX DTM of candidate crater Noord.

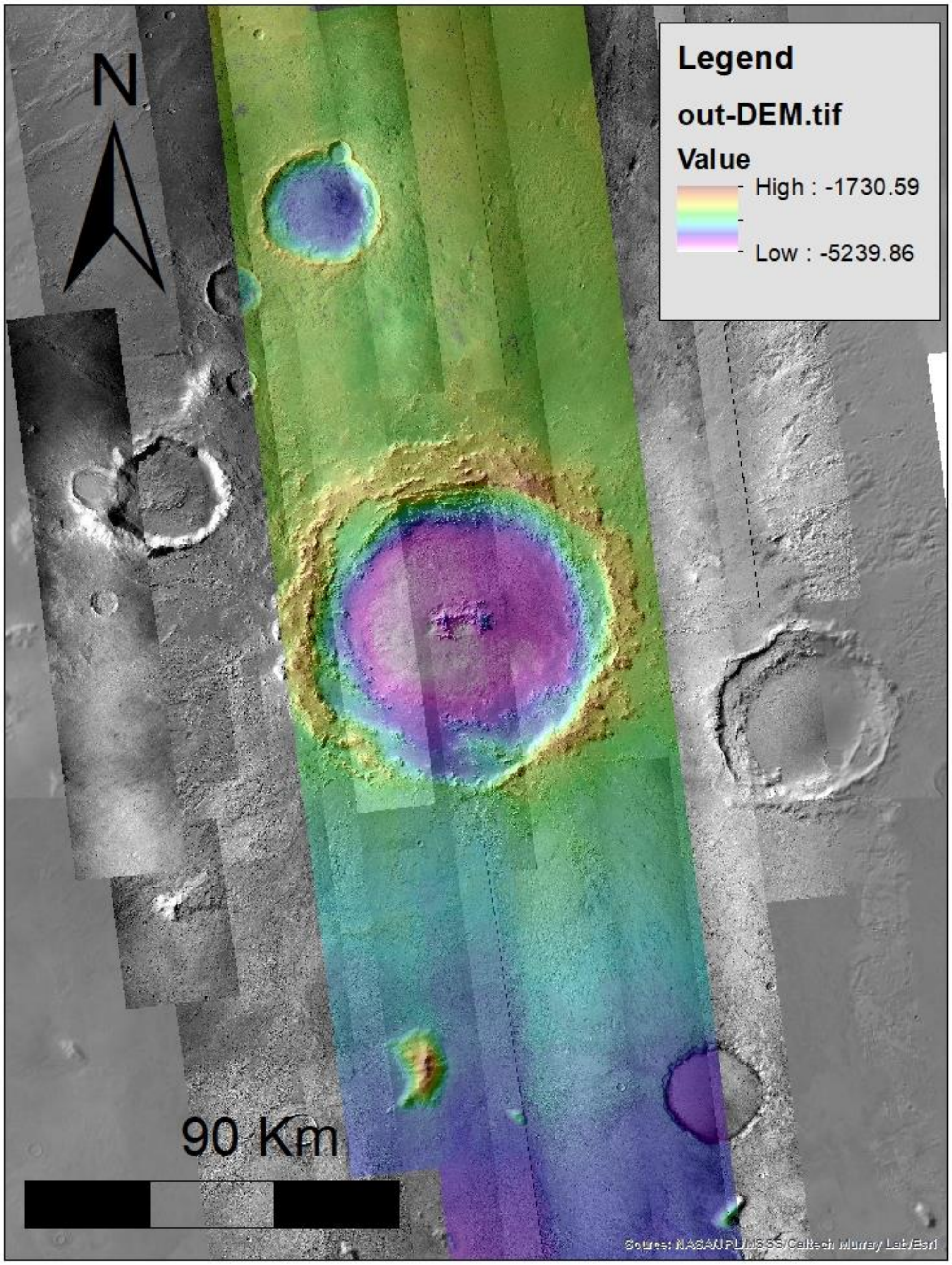

Appendix B Figure 8 CTX DTM of candidate crater Pál.

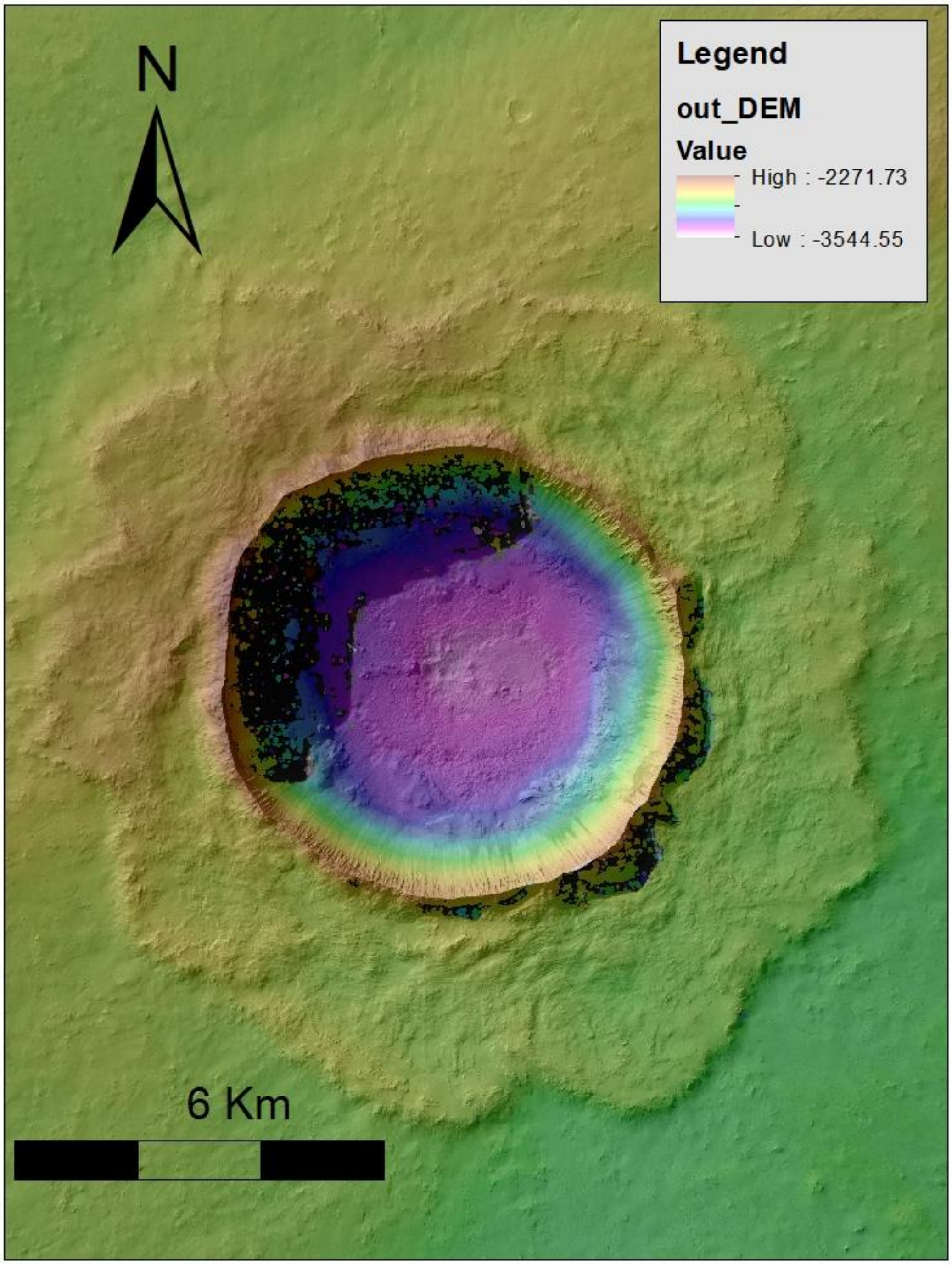

Appendix B Figure 9 CTX DTM of candidate crater Resen.

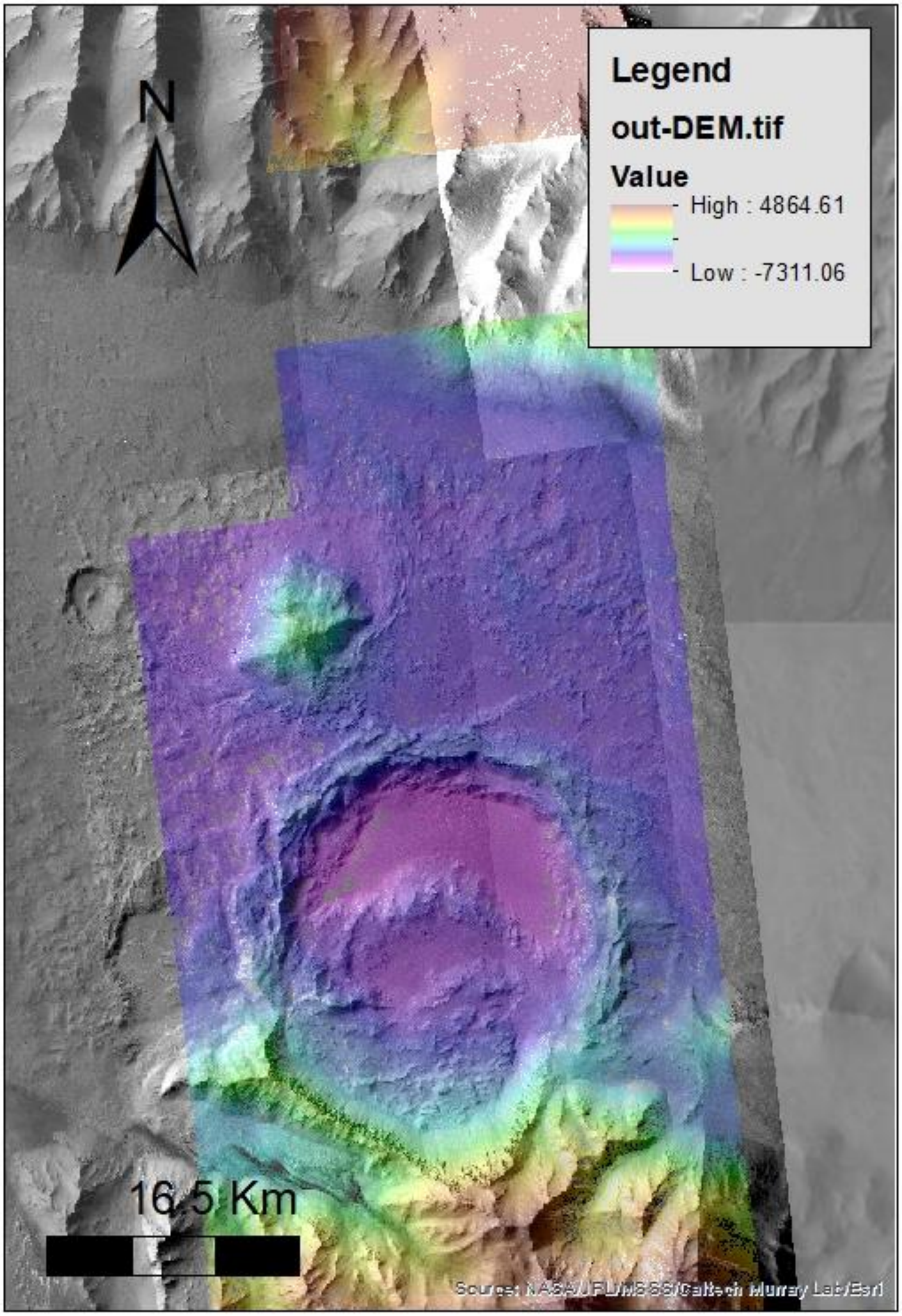

Appendix B Figure 10 CTX DTM of candidate crater Sibiti.

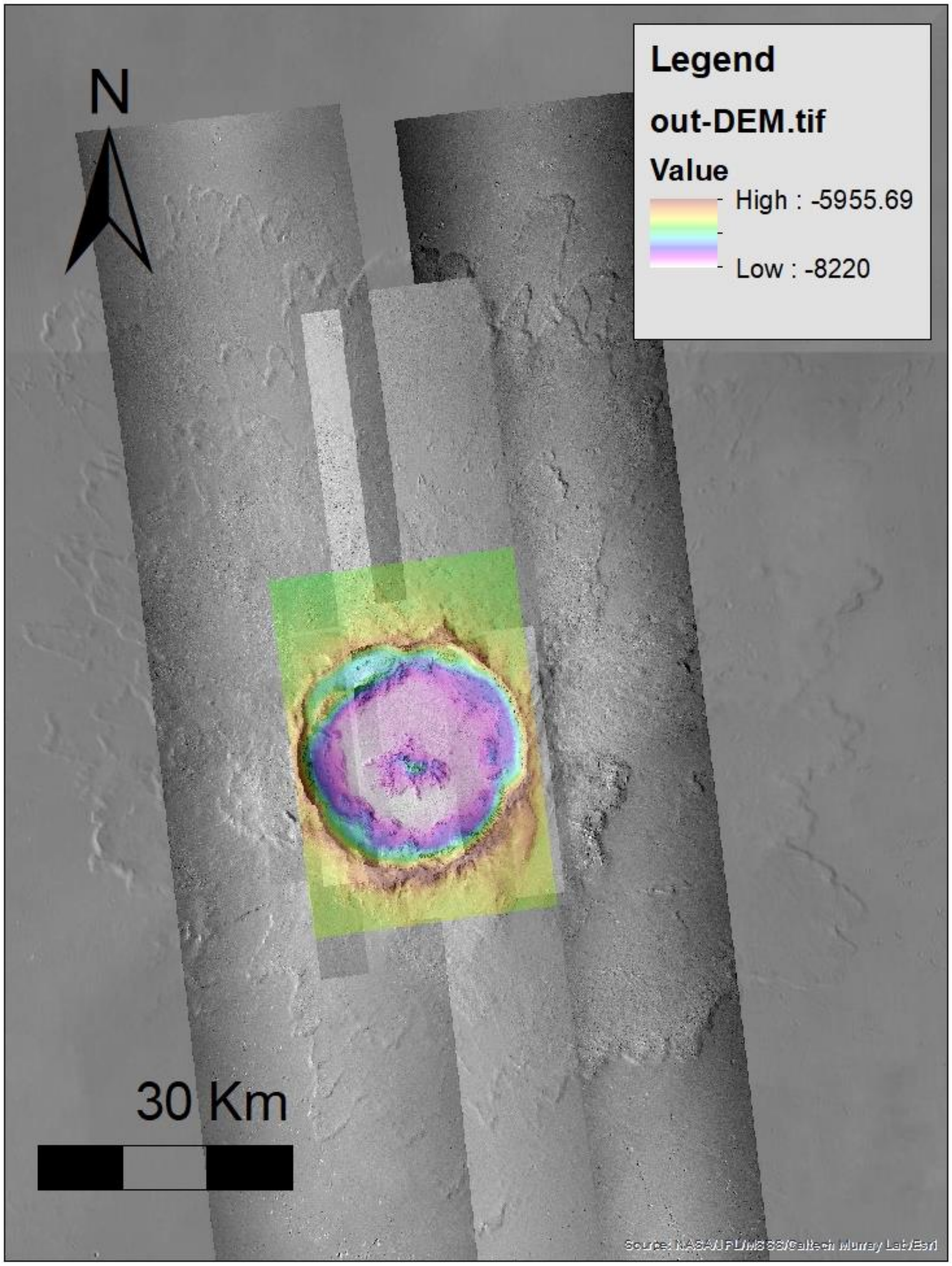

Appendix B Figure 11 CTX DTM of candidate crater Tooting.

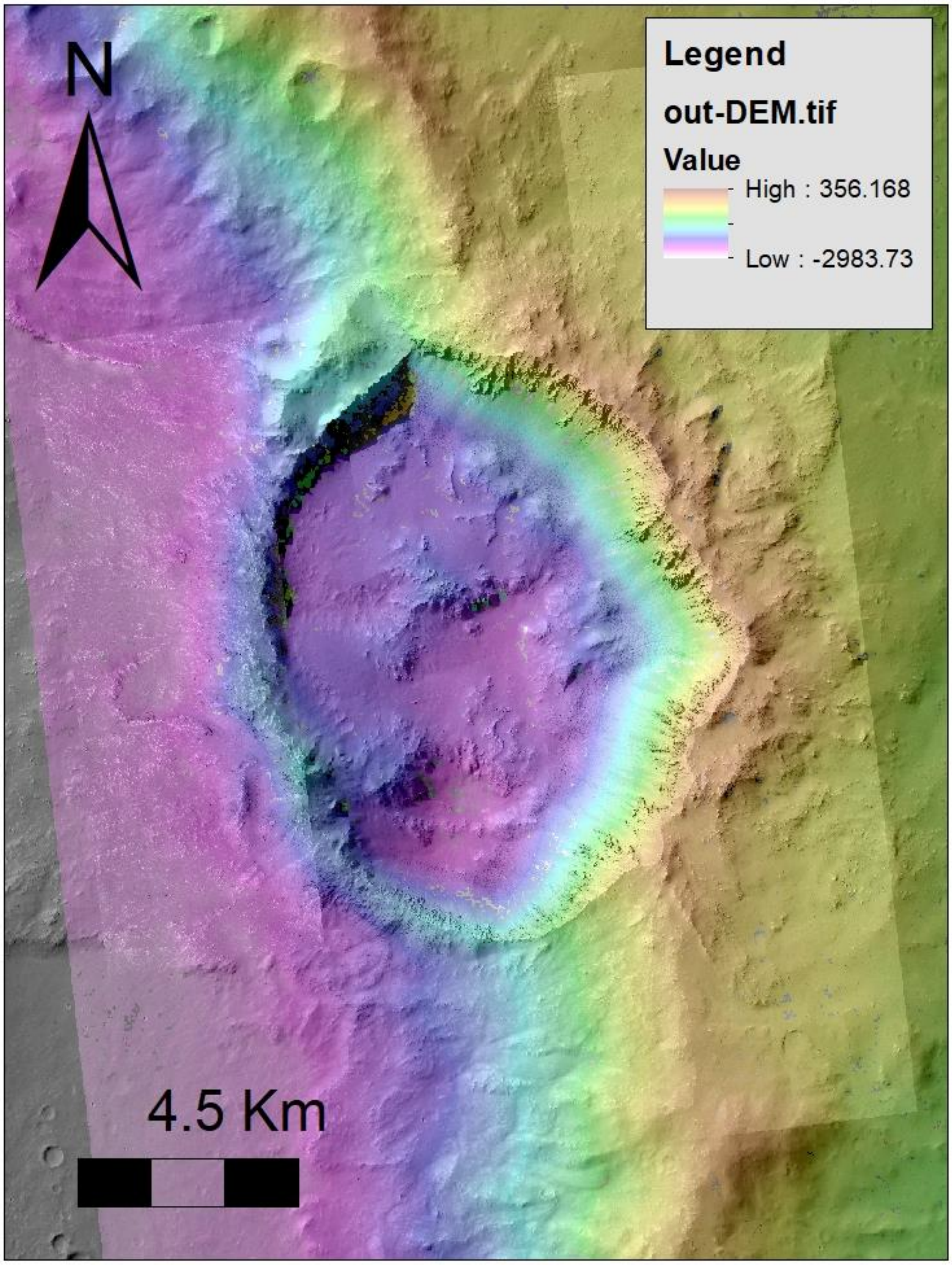

Appendix B Figure 12 CTX DTM of candidate crater "TyrrhenaTerra".

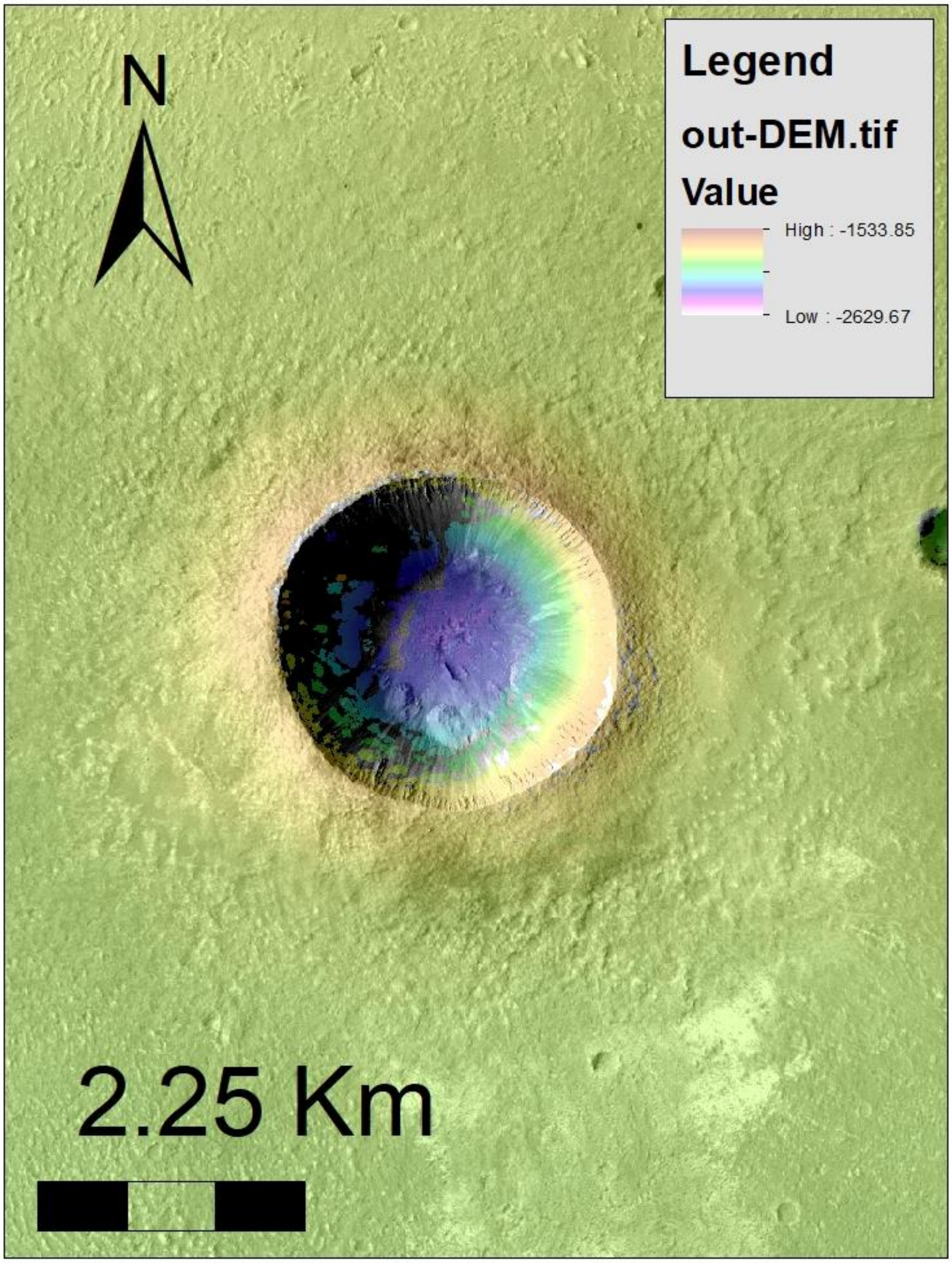

Appendix B Figure 13 CTX DTM of candidate crater Zumba.

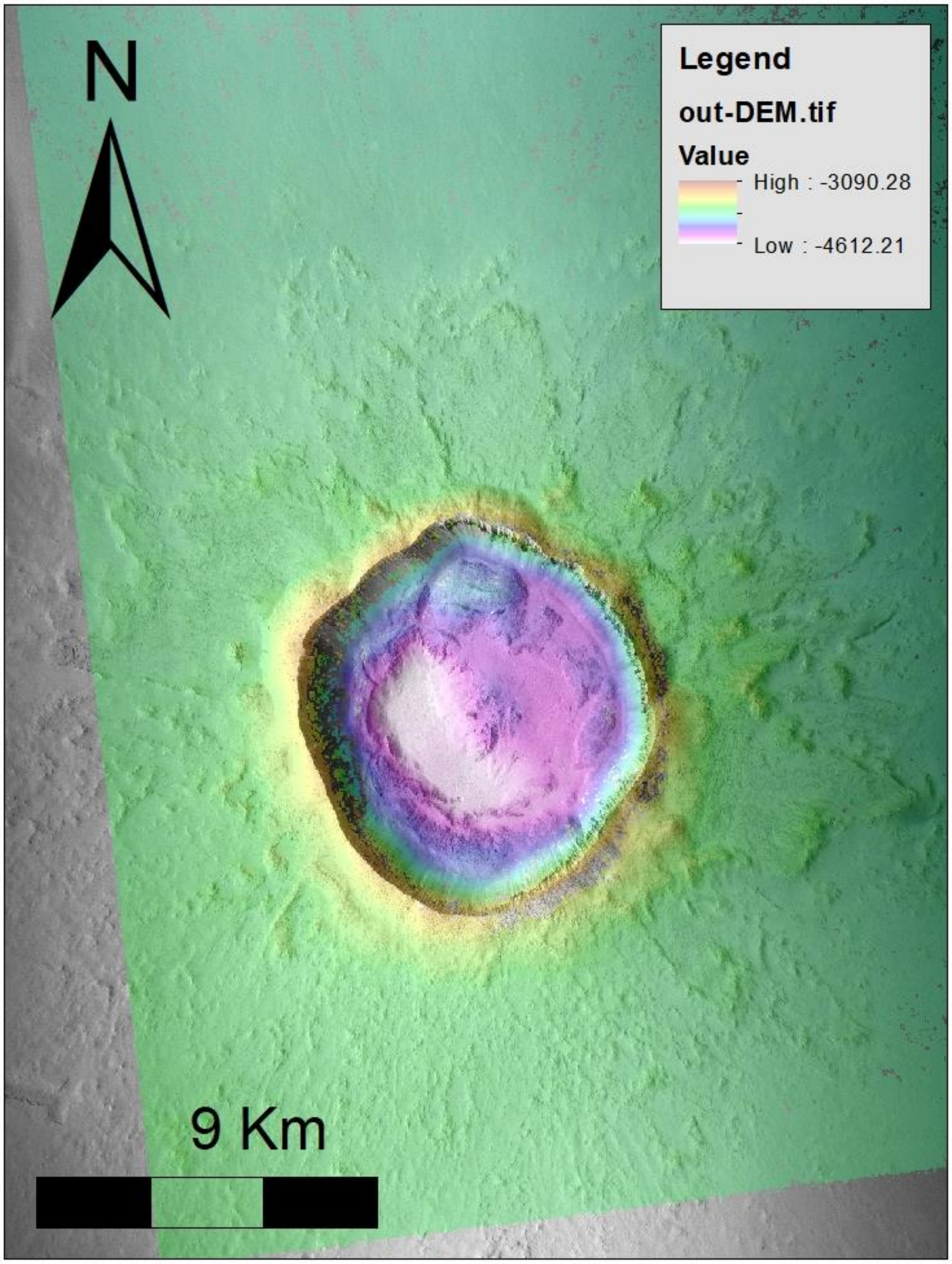

Appendix B Figure 14 CTX DTM of candidate crater Zunil.

Appendix C

This section describes the techniques and equations that went into the measurement of percent melt volume per transient crater cavity volume presented in Chapter 4. Here, we assumed a number of conditions. First, we held the density of the projectile and target constant at 3 g/cm^3, based on the density of target material (presumed anorthosite) and the density of the projectile (presumed chondrite). Secondly, we assumed a projectile diameter of 1 km because estimates from size frequency distributions of the main asteroid belt suggest this diameter is the most common amongst currently observed asteroids (n~10^5-10^6 Bottke et al., (2005)). Our third assumption held the angle of impact for each body to be similar to those values found in Table 2 from Le Feuvre & Wieczorek, (2008), with the exception of Ceres, where we assumed an average angle of impact to be 45°. Our fourth assumption approximates the volume of a transient crater through the technique implemented by Pierazzo & Melosh, (2000). We advise caution utilizing these numbers as there are a number of factors that this back-of-the-envelope calculation does not entirely account for, such as the porosity of the target or projectile.

Assumptions:

- Density of target rock (presumed anorthosite): 3 g/cm^3
- Density of projectile (presumed chondrite): 3 g/cm^3
- Diameter of projectile: 1.0 km
- Average impact angle, unless otherwise indicated: 45°

To complete this calculation, we used our assumed variables as inputs into scaling equations for the different crater properties. Previous work has detailed scaling equations of a given impact for (1) crater diameter (Grieve & Cintala, 1992) and crater depth, specific to each planetary body (Barnouin et al., 2012; Basilevsky et al., 1987; Grieve & Robertson, 1979; Hiesinger et al., 2016; Pike, 1974; Tornabene et al., 2018), (2) the transient cavity volume (Pierazzo and Melosh, 2000), and (3) the generated melt volume (Grieve & Cintala, 1992).

To obtain a crater diameter, we utilized Equation 5 from Grieve & Cintala, (1992), who adapted it from Schmidt & Housen, (1987). In Equation 1, V_{tr} is the volume of the transient cavity, ρ_{pr} and ρ_t are the densities of the projectile and target, respectively, D_{pr} is the diameter of the projectile, g is the surface gravity of the planetary body, ν_i is the velocity of the projectile, and θ is angle of impact measured from the surface. All variables units are in cgs.

$$D_{tc} = 1.16 \left(\frac{\rho_{pr}}{\rho_t}\right)^{1/3} D_{pr}^{0.78} v_i^{0.44} g^{-0.22} \qquad \textbf{Eq. 1}$$

Next, we used the diameter of our given impact crater to calculate the depth of the crater for each planetary body. This requires empirically-derived depth-to-diameter scaling equations from each planetary body, as listed below. Here are the equations for complex craters on the different worlds, where D is the diameter of the crater, while d is the depth.

Mercury	$d = 0.18D^{0.98}$	(Barnouin et al., 2012)
Venus	$d = 0.18D^{0.3}$	(Basilevsky et al., 1987)
The Moon	$d = 1.044D^{0.301}$	(Pike, 1974)
Earth	$d = 0.15D^{0.43}$	(Grieve and Robertson, 1979)
Mars	$d = 0.323D^{0.538}$	(Tornabene et al., 2018)
Ceres	$d = 0.82D^{0.37}$	(Hiesinger et al., 2016)

We would also like to point out the simple-to-complex transition for each body is dependent on the size of the planetary body. We would like to make a note that the size of the craters generated by a 1 km projectile produces craters that are on the smaller side of complex, where some craters fall in the simple-to-complex transition for that body particularly for the Moon and Ceres, so caution is advised when utilizing these numbers.

Now that we have found the depth of a crater for an average impact on each planetary body, we calculated the volume of the transient cavity and the volume of melt generated. To do the former, we used Eq. 2, from Pierazzo & Melosh, (2000), who similarly adapted the equation from Schmidt & Housen, (1987). The variables in Eq. 2 are the same as those in Eq. 1.

$$V_{tr} = 0.28\frac{\rho_{pr}}{\rho_t}D_{pr}^{2.35}g^{-0.65}v_i^{1.3}sin^{1.3}\theta \qquad \textbf{Eq. 2}$$

We then calculated the volume of melt generated during an impact and we used the scaling equation and constant table put forth by Grieve & Cintala, (1992). Here V_m is the volume of melt in km^3, D_{tc} is the diameter of the transient cavity in km, and c and d are unitless constants that can be referenced for a given impactor velocity and for a given impactor type, in this case, chondrite.

$$V_m = cD_{tc}^d \qquad \textbf{Eq. 3}$$

Impact Velocity (km/s)	c	d
15	0.000621	3.85
25	0.000715	3.85
50	0.000831	3.85

Recent work by Abramov et al. (2012) revisits the equations for transient crater cavity, diameter of the crater, the melt volume scaling from Schmidt & Housen, (1987) and Grieve & Cintala, (1992). The authors revised Eq. 2, citing that the transient crater cavity is approximately a factor of four too large. The revised equation is as follows (note the difference in the leading constant):

$$V_{tr} = 0.0745\frac{\rho_{pr}}{\rho_t}D_{pr}^{2.34}g^{-0.66}v_i^{1.3}sin^{1.3}\theta$$ **Eq. 4**

Abramov et al., (2012) also provided a revised equation for crater diameter for a given impact but intentionally leaving out the angle dependence, citing that transient crater diameter is weakly dependent on impact angle and that its effects are also likely target-dependent. Eq. 1 closely resembles that reported in Abramov et al., (2012), so we opt to leave the equation as it is. Abramov et al., (2012) also revise the melt volume scaling equation, Eq. 3, explicitly accounting for energy to melt the target rock, density of both projectile and target rock, and impact angle. The authors derive two equations: one that is dependent on impact velocity and independent of surface gravity, referred to as the "astronomer's perspective", and the another is dependent on surface gravity but independent of impact velocity, referred to as the "geologist's perspective". The astronomy perspective gives higher theoretical melt volume estimates than the geologists perspective (the transfer of energy from kinetic to heat is given more weight than for the geologist perspective, in which some energy is assumed to be lost to other processes). E_m is the specific internal energy required to melt the target. Eq. 5 and Eq. 6 could provide an upper and lower limited for generated melt volumes, respectively.

Astronomer's Perspective

$$V_m = 0.22E_m^{-0.85}\frac{\rho_{pr}}{\rho_t}D_{pr}^{3}v^{1.7}sin^{1.3}\theta$$ **Eq. 5**

Geologist's Perspective

$$V_m = 0.12E_m^{-0.85}\left(\frac{\rho_{pr}}{\rho_t}\right)^{-0.28}D_{tc}^{3.85}g^{0.85}sin^{1.3}\theta$$ **Eq. 6**

Finally, we calculate the ratio of melt volume to transient cavity volume and take the percentage of that result. In Table 5 below, we have provided the full results from our calculation.

In the three different melt volume per transient crater volume calculations there are a couple of observations we can make. First, it seems that the melt volumes calculated by way of Eq. 2 & 3 are strikingly different from the calculations through the means of Eq.

4, 5, & 6. Namely percent melt volume per transient cavity volume through Eq. 2 & 3 puts Mercury at the top of the list for amount of melt generated than for Eq. 4 & 5 or Eq. 4 & 6. This may be because Eq. 3 is solely dependent on crater diameter (which is itself dependent on a variety of factors, weakly gravity), whereas Eq. 6 explicitly takes into account the surface gravity of a body. Additionally, Eq. 5 and Eq. 6 might provide more trustworthy numbers; they follow more what we would expect for the various worlds. According to the calculations through Eq. 5 and Eq. 6, average Cerean impacts will produce the least melt volume per cavity volume, which agrees with the hypothesis that low gravity worlds with low impact velocities will produce low volumes of melt. In contrast, larger bodies, like Venus and Earth, according to these numbers, will create the highest amount of melt volume per cavity volume. Also to note from these revised numbers, the Moon and Earth create similar volumes of melt but due to their differences in gravity they create much different melt volume per cavity volumes. In the Eq. 2 & 3 calculation for the Earth and Moon, it would appear that lunar melt volume per cavity volume would be more than that of Earth, which seems unlikely given that their impact velocities are similar and that Earth has shallower craters due to its size.

Table 5. Full results for the percentage of melt volume per transient cavity volume calculation. Numbers are included for crater diameter and depth as well.

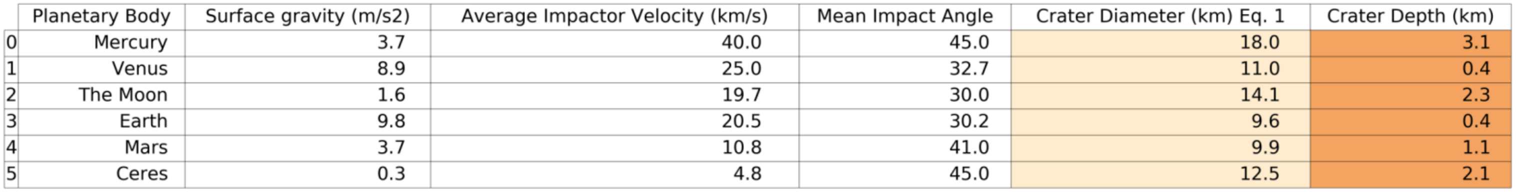

	Planetary Body	Surface gravity (m/s2)	Average Impactor Velocity (km/s)	Mean Impact Angle	Crater Diameter (km) Eq. 1	Crater Depth (km)
0	Mercury	3.7	40.0	45.0	18.0	3.1
1	Venus	8.9	25.0	32.7	11.0	0.4
2	The Moon	1.6	19.7	30.0	14.1	2.3
3	Earth	9.8	20.5	30.2	9.6	0.4
4	Mars	3.7	10.8	41.0	9.9	1.1
5	Ceres	0.3	4.8	45.0	12.5	2.1

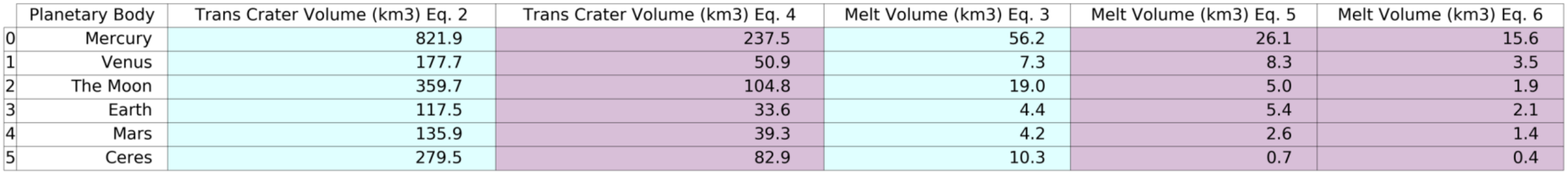

	Planetary Body	Trans Crater Volume (km3) Eq. 2	Trans Crater Volume (km3) Eq. 4	Melt Volume (km3) Eq. 3	Melt Volume (km3) Eq. 5	Melt Volume (km3) Eq. 6
0	Mercury	821.9	237.5	56.2	26.1	15.6
1	Venus	177.7	50.9	7.3	8.3	3.5
2	The Moon	359.7	104.8	19.0	5.0	1.9
3	Earth	117.5	33.6	4.4	5.4	2.1
4	Mars	135.9	39.3	4.2	2.6	1.4
5	Ceres	279.5	82.9	10.3	0.7	0.4

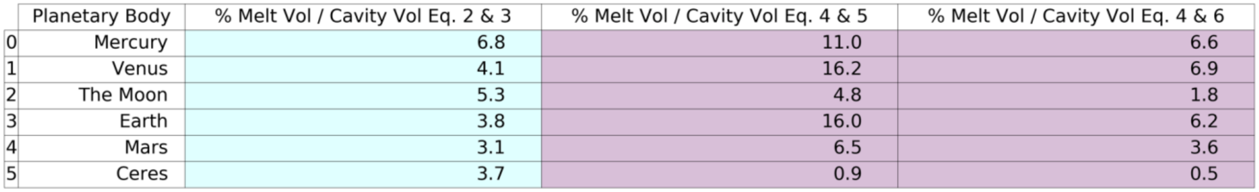

	Planetary Body	% Melt Vol / Cavity Vol Eq. 2 & 3	% Melt Vol / Cavity Vol Eq. 4 & 5	% Melt Vol / Cavity Vol Eq. 4 & 6
0	Mercury	6.8	11.0	6.6
1	Venus	4.1	16.2	6.9
2	The Moon	5.3	4.8	1.8
3	Earth	3.8	16.0	6.2
4	Mars	3.1	6.5	3.6
5	Ceres	3.7	0.9	0.5

Curriculum Vitae

Name:	William Yingling
Post-secondary Education and Degrees:	University of Arizona Tucson, Arizona, USA 2011-2016 B.Sc.
	The University of Western Ontario London, Ontario, Canada 2018-2020 M.Sc.
Honours and Awards:	Undergraduate Achievement Award (University of Arizona) 2016
Related Work Experience	Teaching Assistant The University of Western Ontario 2018-2020
	HiRISE Cycle Planning The University of Western Ontario October 2019
	CanMoon Canadian Lunar Sample Return Analogue Mission The University of Western Ontario September 2019
	Student Employee Lunar and Planetary Laboratory 2015-2016
	HiRISE Student Employee University of Arizona 2014-2016

Publications:

Yingling, W. A., Neish, C. D., Tornabene, L. L., (2020) Impact Melt-Bearing Deposits Around Martian Crater, 51st Lunar and Planetary Science Conference, LPI Contribution No. 2326, 2020, id.2672

Yingling, W., G. Besla (2016) Studying the Gravitational Dark Matter Wake of M33 During the Merging of the Milky Way and Andromeda. American Astronomical Society